Thèse n° 9103

Pressure on obstacles induced by granular snow avalanches

Présentée le 6 août 2021

Faculté de l’environnement naturel, architectural et construit
Laboratoire d’hydraulique environnementale
Programme doctoral en mécanique

pour l’obtention du grade de Docteur ès Sciences

par

Michael Lukas KYBURZ

Acceptée sur proposition du jury

Prof. J.-F. Molinari, président du jury
Prof. C. Ancey, Dr B. Sovilla, directeurs de thèse
Prof. N. Gray, rapporteur
Dr T. Faug, rapporteur
Prof. M. Sawley, rapporteur

École
polytechnique
fédérale
de Lausanne

2021

Le risque reste cependant le sel de la vie …
… qui doit être un plat relevé !

— Jean-Jacques Loup, Tour du Rwanda 2016

Acknowledgements

In the course of my PhD I was very fortunate to be able to count on the support of my supervisors, fellow PhD students, flat mates, friends and family.

My biggest thanks go to Betty Sovilla, who acquired the research grant and is therefore the "mother" of this project. Beside her great experience and competence in avalanche research I tremendously valued her constant positive attitude and willingness to help, be it for small or more substantial problems in all respects. Special thanks also go to Christophe Ancey and Johan Gaume, who contributed greatly to the making of this thesis with their scientific support, expertise, valuable discussions and manuscript revisions. Thank you Betty, Christophe and Johan for all your support, patience and advice with which you helped me to grow as a scientist.

Furthermore, I'd like to thankfully acknowledge the people who supported me with the setup and the installation of the high-speed camera in Vallée de la Sionne. Amongst others these are foremost Mark Schaer, Martin Hiller, Marco Collet and Michael Hohl. Beside the scientific relevance of the camera's data it has always been captivating to watch the videos over and over again, grasping an insight into the unleashed might of nature in the avalanches.

Thank you Fabienne from all my heart for everything you mean to me, for patiently tolerating my deficiencies, as well as for your understanding for my pursuit of this thesis, during which our realities have become very different and distant at times.

I'd like to thank Philipp for staying a true friend despite only occasional visits.

I also acknowledge my mom and dad, who always got my back, supporting me in every possible way in my various undertakings and goals, thus allowing me to become what I am today.

Many thanks go to my brothers Daniel and Andreas, who are great supportive companions and to whom I've been very happy to reconnect during the time of the thesis.

Thanks also go to my fellow sailors, supporters and coaches for all the moments of hardship and absolute joy we shared on water and ashore. I am hugely grateful for the life lessons learned from early on in competitive sports. The 470 Masters title 2019, during the making of this thesis, makes me proud and is a great conclusion of my active years.

Finally, I want to appreciate my flat mates Giulia and Christian, the “Frenchies” Camille, Guillaume, Grégoire, Martin, as well as Gregor and so many other great people in Davos, whom I’m lucky enough to count as my dear friends, going-out and sports companions.
The early morning, daytime or nocturnal ski-touring and free riding, the lunch break CC-skiing, cycling or trail-running escapes — the evenings at home and nights out — sharing countless moments of laughter and joy, as well as difficult times with you — every aspect of this beautiful mix will always remain fond memories of mine and made my PhD in Davos a fabulous journey.

Davos, April 2021 M.L. K.

Abstract

The increasing population and the consequential demand for dwelling and recreation areas lead to more frequent conflicts between humans and natural hazards. In mountainous regions snow avalanches are, therefore, still a major threat to humans and infrastructure, with a significant impact on the economy and tourism. For the development of design criteria for infrastructure it is crucial to obtain a thorough understanding on the pressure exerted by avalanches, so that they can withstand avalanche impact.

Although the differences between avalanche flow regimes reportedly play a crucial role for the avalanche–obstacle interaction, to date the impact pressure is often calculated similarly to the dynamic pressure in inviscid fluids proportional to velocity square and using empirical drag coefficients. Indeed, in the inertial flow regime, which is typical of powder avalanches, the impact pressure is proportional to velocity square. However, in the gravitational regime, which is typical of wet avalanches, the pressure is proportional to the flow depth. The empirical proportionality factor in the gravitational regime is referred to as the amplification factor. Field measurements indicate that the amplification factor and the drag coefficient may range within considerable boundaries. Thus, in the absence of a physics-based framework to make the crucial choice of the drag coefficient and the amplification factor for the impact pressure calculation, engineers need vast knowledge and experience in constructing in avalanche terrain and snow avalanche dynamics. Even for experienced experts it is often unclear how to calculate the impact pressure adequately according to the expected avalanche flow regime or how to consider the obstacle geometry in the calculation.

The aim of this project is to develop a physics-based framework for the calculation of avalanche pressure on obstacles. In particular, we want to evaluate drag coefficients and amplification factors as a function of snow properties and avalanche flow regimes. To reach this goal we develop a numerical Discrete Element Method model to investigate the interaction of avalanche flows and obstacles, using a cohesive bond contact law.

We test the relevance of the model by comparing simulated impact pressures with field measurements from the “Vallée de la Sionne” experimental site. By varying avalanche flow velocity and cohesion in the simulations, we show that the impact pressure can be interpreted as the superposition of an inertial, a frictional and a cohesive contribution. Further, we find a novel scaling law, reducing the problem of calculating the pressure induced by cohesive flows, to the calculation of cohesionless flows. We provide evidence that in the cohesionless case the compression inside the influenced flow domain around the obstacle, the mobilized domain, governs the impact pressure of granular flows in the gravitational regime. If the cohesion is high, we find that the cohesive bonds further enhance the stress transmission in the compressed mobilized domain, leading to an increase in impact pressure. Considering an inertial and a gravitational contribution, we quantitatively link the properties of the mobilized domain to the pressure. Finally, the knowledge from previous research and the findings of this thesis allow us to propose a physics-based framework to estimate the impact pressure by applying simple geometrical considerations and fundamental avalanche flow characteristics.

Key words:
- Calculation of impact pressure on obstacles
- DEM simulation of cohesive granular flows interacting with obstacles
- Snow avalanche engineering and structural design in avalanche prone terrain

Zusammenfassung

Anhaltendes Bevölkerungswachstum und der damit verbundene Siedlungsdruck sowie die vermehrte Nutzung alpiner Regionen als Erholungsgebiet erhöht die Verwundbarkeit des Menschen durch Naturgefahren. In Bergregionen sind Lawinen daher stets eine Bedrohung für Mensch und Infrastruktur und haben erheblichen Einfluss auf Wirtschaft und Tourismus. Damit Infrastrukturbauten Lawineneinwirkungen standhalten können, ist ein gutes Verständnis der Lawinenkräfte für die Erarbeitung von Bemessungsrichtlinien unerlässlich.

Obwohl bereits seit Jahrzehnten vermutet wird, dass die physikalischen Prozesse innerhalb der Lawine stark mit dem jeweiligen Fliesstyp variieren, werden die Lawinendrücke gemäss den gängigen Berechnungsmethoden meist unter Anwendung von empirischen Druckbeiwerten proportional zur Fliessgeschwindigkeit im Quadrat berechnet. Tatsächlich ist der Lawinendruck in trägheitsdominierten Lawinen, typischerweise Staublawinen, proportional zum Quadrat der Fliessgeschwindigkeit. Der Aufpralldruck von gravitationsdominierten Fliesslawinen, welcher mit Hilfe des empirischen Verstärkungsfaktors berechnet wird, ist jedoch proportional zur Tiefe unter der Fliessoberfläche. Messungen zeigen auf, dass sich die numerischen Werte der empirischen Druckbeiwerte und Verstärkungsfaktoren eine grosse Streuung aufweisen. Mangels physikbasierter Kriterien für die Wahl der empirischen Faktoren, brauchen Ingenieure umfangreiche Erfahrung, um Strukturen in lawinengefährdeten Zonen zu planen. So ist es selbst für Experten nicht immer klar, wie der jeweilige Lawinen-Fliesstyp und die Geometrie des Hindernisses für die Berechnung des Lawinendrucks im Einzelfall adäquat berücksichtigt wird.

Das Ziel der vorliegenden Arbeit ist es, einen physikbasierten Rahmen für die Lawinendruckberechnung auf Hindernisse zu entwickeln. Im Detail wollen wir Druckbeiwerte und Verstärkungsfaktoren unter Berücksichtigung der vorherrschenden Schnee- und Fliesseigenschaften der Lawinen bestimmen können. Um die Interaktion von Lawinen und Hindernissen numerisch untersuchen zu können, entwickeln wir ein Modell, das auf der Diskrete-Elemente-Methode basiert.

In dem wir die simulierte Lawinengeschwindigkeit und Kohäsion des Lawinenschnees variieren, gelingt es uns zu zeigen, dass der Lawinendruck als Überlagerung eines trägheits-, reibungs- und kohäsionsabhängigen Druckanteils interpretiert werden kann. Weiter entwickeln wir ein neuartiges Skalierungsgesetz, mit welchem sich die Problematik der Druckberechnung einer kohäsiven Lawine auf die Druckberechnung der entsprechenden kohäsionslosen Lawine reduzieren lässt. Wir präsentieren Evidenz, dass die Kompression des granularen Mediums im Einflussbereich des Hindernisses in der Lawinenströmung den Lawinendruck in kohäsionslosen gravitationsdominierten Fliesslawinen massgeblich beeinflusst. Im Falle kohäsiver Lawinen verstärkt die Kohäsion die Kraftübertragung zwischen den Schneepartikeln zusätzlich, was zu erhöhtem Aufpralldruck führt. Unter der Berücksichtigung eines gravitations- und eines trägheitsabhängigen Druckanteils gelingt es uns einen Zusammenhang zwischen den Schneeeigenschaften in der Einflusszone des Hindernisses und dem Aufpralldruck herzustellen. Schlussendlich präsentieren wir unter Einbezug von früheren Studien sowie eigener Resultate eine Methode zur physikbasierten Berechnung des Lawinenaufpralldrucks, welche lediglich von der Hindernisgeometrie und fundamentalen Fliesseigenschaften der Lawine abhängt.

Stichwörter:
- DEM Simulation der Interaktion von kohäsiven granularen Lawinen mit Hindernissen
- Berechnung vom Lawinenaufpralldruck auf Hindernisse
- Bauliche Gestaltung von Lawinen-gefährdeten Objekten

Contents

Acknowledgements **i**

Abstract (English/Deutsch) **v**

List of figures **xiii**

List of tables **xv**

List of symbols **xvii**

1 Introduction **1**

1.1 A preliminary note on flow regime 1

1.2 Computing impact pressure: a brief state of the art 3

1.3 Insights from experiments and Discrete Element Method simulations of flowing granular materials 6

1.4 Research question and chapter outline 8

2 The role of inertia, friction and cohesion in the pressure build-up on the Vallée de la Sionne measurement pylon **11**

2.1 Chapter summary 12

2.2 Materials and Methods 12

2.2.1 Experimental data and test case 12

2.2.2 Modeling snow using the Discrete Element Method 13

2.2.3 Modeling the interaction of the avalanche flow and structures 14

2.2.4 Model parameters 16

2.2.5 Comparing simulated impact pressure profiles to field measurements . 17

2.3 Results 18

2.3.1 Comparison of DEM simulations with field measurements 18

2.3.2 Influence of velocity and cohesion on impact pressure 19

2.3.3 Analysis of the mobilized domain and origin of the pressure amplification at the micro-scale 22

2.3.4 Pressure and range of cohesion in gravitational avalanches 27

2.4 Discussion 29

2.4.1 Modelling avalanche–obstacle interaction with DEM 29

2.4.2 Impact pressure contributions at the macro-scale 30

2.4.3 Micro-scale processes of impact pressure build-up 31
2.5 Conclusions 32

3 The concept of the mobilized domain: how it can explain and predict the forces exerted by a cohesive granular avalanche on an obstacle 35
3.1 Chapter summary 36
3.2 Materials and Methods 36
3.2.1 Simulation setup and procedure 37
3.2.2 Obstacle geometries 39
3.2.3 Granular flow and material properties 40
3.2.4 Compression tests of the granular material 41
3.2.5 Definition of the mobilized domain 43
3.3 Results 45
3.3.1 Influence of the obstacle width and geometry on the impact pressure and the MD 45
3.3.2 Influence of cohesion on the impact pressure and the MD 50
3.3.3 Analytical model to quantitatively link the MD properties to the impact pressure 51
3.4 Discussion 53
3.4.1 Physical processes governing the flow–obstacle interaction and impact pressure for varying obstacle geometries 53
3.4.2 Influence of cohesion on the flow–obstacle interaction processes 55
3.4.3 Analytical model to quantitatively link the MD properties to the impact pressure 56
3.4.4 Limitations 57
3.5 Conclusions 58

4 Physics-based estimates of drag coefficients for the impact pressure calculation of dense snow avalanches 61
4.1 Chapter summary 62
4.2 Simulation of avalanche impact pressure on obstacles with DEM 62
4.2.1 Avalanche modeling setup and parameters 62
4.2.2 Obstacle geometries 63
4.2.3 Avalanche scenarios 66
4.3 Comparison of simulated and measured impact pressure on obstacles of varied geometry 69
4.4 Average impact pressure exerted on obstacles of different geometries 71
4.5 Pressure distribution on obstacles of different geometries 73
4.6 Impact pressure calculation 76
4.6.1 Estimation of drag coefficients for cohesionless avalanches 76
4.6.2 Impact pressure exerted by cohesive avalanches 78
4.7 Comparison of calculated impact pressure with simulations and measurements 79
4.7.1 Cohesionless avalanches 79

4.7.2 Real avalanche scenarios . . . 81
4.8 Discussion . . . 83
4.8.1 Avalanche impact pressure on obstacles of varying geometry . . . 83
4.8.2 Estimation of the drag coefficient . . . 84
4.9 Conclusions . . . 86

5 Conclusions 89
5.1 Context and goal of the thesis . . . 89
5.2 DEM model for avalanche–obstacle interaction . . . 89
5.3 Impact pressure — from the physical origin to impact pressure calculations . . 90
5.4 Influence of the flow regime and the obstacle geometry on the impact pressure 92

6 Outlook 95
6.1 Modelling avalanche-obstacle interaction with DEM . . . 95
6.2 Determining and calibrating the crucial parameter of cohesion . . . 96
6.3 Existence and properties of the mobilized domain . . . 96
6.4 Relevance of the thesis results for practical avalanche engineering . . . 97

A Supplementary material for chapter 2 99
A.1 Formulation of the Discrete Element Method . . . 99
A.2 Model setup . . . 103
A.3 Simulation procedure . . . 104
A.4 Clarification of the quantities used for the analyses . . . 105
A.4.1 Vertical location . . . 106
A.4.2 Velocity . . . 106
A.4.3 Impact pressure . . . 107
A.4.4 Confining pressure . . . 107
A.4.5 Contact forces and mobilized domain . . . 107

B Supplementary material for chapter 3 109
B.1 Temporal evolution of the impact pressure during simulations . . . 109
B.2 Sensitivity analysis of axial compression tests . . . 110
B.3 Definition of the mobilized domain (MD) . . . 111
B.4 Sensitivity of the results on the MD threshold value . . . 112
B.5 Impact pressure calculated from reported drag forces in the literature . . . 114
B.5.1 Impact pressure scaling law for cohesive avalanches . . . 114

C Supplementary material for chapter 4 117
C.1 Simulation procedure . . . 117
C.2 DEM parameters . . . 118
C.3 Pressure calculation for real avalanche scenarios: parameter choice . . . 119

Bibliography 121

Curriculum Vitae **131**

List of Figures

1.1 Warm and cold avalanche deposits at the Vallée de la Sionne wall obstacle . . . 3
1.2 Supercritical avalanche flowing around the Vallée de la Sionne pylon 6

2.1 DEM simulation setup 15
2.2 Simulated and measured impact pressure profile comparison 19
2.3 Comparison of simulated and measured impact pressure versus velocity 20
2.4 Impact pressure of varying velocity and cohesion 21
2.5 Micro-scale analysis of the flow and contact forces around the pylon 23
2.6 Influence of the Fr on the mobilized domain 25
2.7 Influence of cohesion on contact forces and the mobilized domain 27
2.8 Simulated and measured pressure and pressure fluctuations 28

3.1 Simulation procedure chapter 3 38
3.2 Prismatic obstacles 40
3.3 Axial compression tests—setup and results 43
3.4 Visualization of the MD 45
3.5 Impact pressure on obstacles of varying widths w and for different geometries 46
3.6 Horizontal sections through flow around the obstacle showing the velocity field and the contact forces 48
3.7 Time series of MD properties and pressure 49
3.8 Influence of cohesion on the contact network inside the MD 51
3.9 Comparison of calculated and simulated impact pressure exerted by cohesionless flows 53

4.1 Vallée de la Sionne measurement obstacles 65
4.2 Generic obstacles in DEM 66
4.3 Comparison of simulated and measured impact pressure on the Vallée de la Sionne obstacles 70
4.4 Dependence of impact pressure p_x on obstacle geometry and width w 73
4.5 Impact pressure distribution on obstacle surfaces 74
4.6 Horizontal pressure distribution on obstacles 75
4.7 Estimation of C_o 77
4.8 Comparison of simulated and calculated impact pressure 80
4.9 Comparison of measured, simulated and calculated impact pressure profiles . 82

A.1 The parallel bond contact model 100
A.2 DEM simulation procedure 104
A.3 Comparison DEM obstacle and field measurement structure 104
A.4 Impact pressure time series 105
A.5 Impact pressure time averaging sensitivity 106

B.1 Time series of the simulated pressure 109
B.2 Sensitivity analysis for the axial compression tests 111
B.3 Definition of the MD 112
B.4 Sensitivity of the results on the MD threshold value 113
B.5 Sensitivity of the MD extent on the MD threshold value 113
B.6 Impact pressure calculated from reported drag forces from the literature 114

C.1 Detailed DEM simulation procedure 118

List of Tables

2.1 DEM simulation parameters in the gravitational and inertial regime 17

3.1 Granular material properties and simulation setup parameters chapter 3 41

4.1 Material properties for the Discrete Element Method (DEM) simulations. 63
4.2 Simulated avalanche flow scenarios. 69

A.1 DEM simulation parameters (extended) 101

List of Symbols

Acronyms

DEM	Discrete Element Method
MD	Mobilized Domain
VdlS	Vallée de la Sionne

Symbols

A	Obstacle's projected area facing the flow direction
Bo	Bond number
c	Empirical gliding factor (Haefeli, 1939; Haefeli, 1951), see Appendix D in (Ancey and Bain, 2015)
C	Coefficient for C_D in the phenomenological model of Faug (2015)
c_1, c_2, c_3	Fitting parameters for f_{coh}
C_{d0}	Empirical coefficient for C_D (Gauer and Jóhannesson, 2009; Gauer and Kristensen, 2016)
C_D	Drag coefficient
C_{geo}	Geometry-dependent coefficient of C_D
C_o	Shape-dependent coefficient of C_{geo}
C_r	Flow-regime-dependent coefficient of C_D
C_w	Width-dependent coefficient of C_{geo}
d	Diameter of cylindrical obstacle in Haefeli (1939) and Haefeli (1951)
D_x, D_y, D_z	Simulation domain extent in the x, y and z-direction
d_n	Width increment of the obstacle cross section
E	DEM particle Young's modulus
e_r	Restitution coefficient in DEM
f	Empirical coefficient for C_D from (Gauer and Jóhannesson, 2009; Gauer and Kristensen, 2016)
f_{coh}	Impact pressure increase factor due to cohesion
F_D	Drag force on obstacle
F_n	Normal contact forces
F_x, F_y, F_z	Force on obstacle in the x, y and z-direction
$F_{x,g}$	Gravitational contribution of the impact force on obstacles

$F_{x,i}$	Inertial contribution of the impact force on obstacles
Fr	Froude number
g	Gravitational acceleration
h	Avalanche flow height
K	"Pure earth coefficient" from (Faug, 2015) and (Thibert et al., 2013)
l	Sample length in the direction of deformation in axial compression test
l_0	Original sample length in the direction of deformation in axial compression test
L_{MD}	Streamwise extent (length) of the MD
m_{MD}	Mass of the granular medium inside the MD
n	Empirical exponent for weighting Fr in (Thibert et al., 2008)
p	Impact pressure
p^*	Impact pressure of a cohesive avalanche flow (chapters 3 and 4)
$p_{coh.less}$	Impact pressure of a cohesionless avalanche flow (chapter 2)
p_x	Impact pressure projected on the plane normal to the streamwise direction
$p_{x,calc}$	Calculated impact pressure of a cohesionless avalanche flow
$p_{x,g}$	Gravitational contribution of the impact pressure on obstacles
$p_{x,i}$	Inertial contribution of the impact pressure on obstacles
$q_{Bo,Fr}$	Bond to Froude number ratio $q_{Bo,Fr} = Bo/Fr$
R	Curvature radius of ground contour
r_p	DEM particle radius
v	Avalanche flow velocity
v_{MD}	Streamwise velocity of the granular material inside the MD
v_u	Impact velocity
w	Obstacle width
x	Streamwise direction in DEM
y	Transverse direction to the flow in DEM
z	Vertical direction in DEM
α	Wedge apex half-angle
β	Incidence angle
ϵ_n	Axial strain in compression test
δ	DEM absolute particle interpenetration
Δ	DEM particle interpenetration relative to particle radius
$\Delta t_1, \Delta t_2$	Simulation periods in simulation *phase I* and *phase II*
ζ	Empirical coefficient for the gravitational pressure contribution (Sovilla et al., 2010)
η_F	Efficiency factor (Haefeli, 1948)
θ	Ground slope
θ_n	Angle between impact surface increment and transverse direction to the flow
κ	Active/passive earth coefficient
μ	DEM Coulomb friction coefficient
ρ	Snow bulk density

ρ_b	DEM bulk density
ρ_m	Snow bulk density upon impact
ρ_p	DEM particle density
σ_{coh}	DEM cohesive bond tensile and shear strength
σ_n	Axial stress in compression test
σ_z	Hydrostatic stress inside the granular material

1 Introduction

Mountainous areas face various hazards involving the rapid mass movement of a finite volume of material. Typical examples include snow avalanches, debris flows, and rock avalanches. Building structures in this environment involves ensuring that they are placed in a safe area or, if this is not the case, reinforcing them. To that end, computational methods have been developed for estimating runout distances and forces exerted by the flowing mass on fixed obstacles (Perla, 1980; Hopfinger, 1983; Hutter, 1996; Ancey, 2012).

Faced with the thorny problem of estimating impact pressures exerted by complex natural materials, engineers have used analogies between avalanches and related issues in hydrodynamics or geotechnical engineering. Today, a routinely used definition of avalanche impact pressure is copied from the definition of drag force in fluid dynamics when computing the force exerted by a Newtonian fluid on an immersed body (e.g., Chap. 1 in White, 1991):

$$p_x = \frac{F_D}{A} = C_D \frac{\rho}{2} v^2 \tag{1.1}$$

where F_D is the drag force on the obstacle, A is the projected area facing upstream, C_D is the drag coefficient, ρ is the snow density, and v is the flow velocity (Mellor, 1978; Hopfinger, 1983; Burkard et al., 1990; Mears, 1992; Jóhannesson et al., 2009). The main difficulty of the problem lies in the determination of the drag coefficient C_D if we assume that we can determine or measure avalanche velocity and density independently. This problem has long seen only partial answers, owing to the scarcity of relevant avalanche data and the complexity of the avalanche behavior.

1.1 A preliminary note on flow regime

Avalanches involve a wide variety of flow features depending on snow, weather and topography, which in turn generate a diversity of flow behavior (Quervain, 1981; McClung and Schaerer, 1993). Since the earliest developments in avalanche science (Coaz, 1881; Mougin, 1922; Allix, 1925; Paulcke, 1938), there has been tension between providing a comprehensive classification of avalanches and outlining the overall flow behavior. In engineering, it has been common to distinguish between *flow avalanches* (dense flows of snow, which follows the ground's contours closely) and *powder avalanches* (dilute clouds of snow particles maintained in suspension by air turbulence and moving at a velocity higher than 50 m/s) (Ancey, 2016).

Here we are concerned with flow avalanches. Let us provide key characteristics, which will assist us later in quantifying the physical processes at hand: the flow depth h generally does not exceed a few meters, and its mean velocity v ranges from 5 to 25 m/s, although velocities as high as 50 m/s have been observed. On average, the density of snow mobilized by flow avalanches ranges from 150 to 500 kg/m^3. Dry snow tends to be light, whereas wet snow has the highest density. Flow avalanches exhibit varied flow regimes depending on snow consistency (cohesion, moisture and density), velocity and topography. A simple dichotomy used in engineering distinguishes between the inertia- and gravity-dominated regimes (or more concisely, inertial and gravitational regimes). Inertia-dominated avalanches reach high velocities ($v > 10$ m/s) and may overrun low-terrain obstacles. Because of their high velocities, they often entrain ambient air during their descent, and thus a density stratification exists across their flow depth: a dilute layer covers a dense core. Gravity-driven avalanches have low velocities ($v \leq 10$ m/s) and closely follow ground contours. They take the appearance of a granular or viscous flow.

Flow regime and snow consistency are often correlated: cold dry snow tends to form inertial avalanches, whereas wet cohesive snow is more prone to forming gravitational flows. Recently, field observations and laboratory experiments have suggested that snow temperature is the key parameter that affects snow cohesion and thus controls flow dynamics (Steinkogler et al., 2014; Steinkogler et al., 2015; Köhler et al., 2018b; Fischer et al., 2018): when snow temperature in the flow is lower than $-1\,^\circ$C the regime is dominated by inertial effects, whereas gravitational effects dominate at temperatures higher than this threshold. To highlight the influence of snow temperature, we speak of *cold* or *warm* snow avalanches. Snow texture changes radically as a function of snow temperature and moisture. Dry snow takes the form of a cohesionless powder, whereas wet snow can take the form of pasty material (like mud) or granular matter. This wealth of texture has marked consequences on bulk behavior, and we have taken this point into account in our study. Figure 1.1 illustrates differences in snow texture, granulometry, amount of deposits on the obstacle and the flow surface between the deposits of a warm and a cold avalanche at the wall obstacle in Vallée de la Sionne (section 4.2.2).

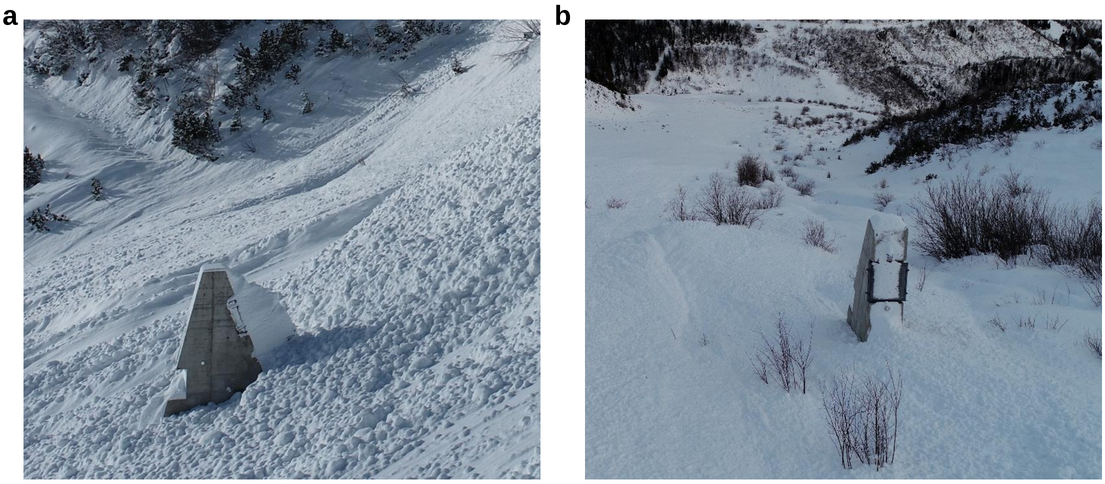

Figure 1.1 – Avalanche deposits at the Vallée de la Sionne wall obstacle. Panel a shows a side view of the wall with the deposits an avalanche with a warm tail (archive number # 20213009 in the VdlS database), which released naturally on January 15th 2021. Panel b shows a frontal view of the wall with the deposits of a typical cold avalanche (archive number # 20193014 in the VdlS database), which released naturally on December 16th 2018. Pictures: P. Huguenin, SLF

1.2 Computing impact pressure: a brief state of the art

For a body immersed in a Newtonian fluid, the drag coefficient C_D in equation (1.1) is usually entirely determined by the body's Reynolds number (White, 1991). For non-Newtonian fluids, the mere existence of the drag coefficient is not ensured, and in many cases little is known about its dependence on flow variables or dimensionless numbers. For snow (as a flowing material), the approach has long been speculative and based on sparse observations and measurements. Avalanche forces started to be measured as early as the 1930s in the former Soviet Union (Roch, 1961; Brugnot and Vila, 1985; Sokratov, 2013) and from the 1950s on in Western countries. At that time and in the subsequent decades until the 1990s, the measurement techniques were rudimentary. The earliest avalanche-dynamics models were also crude (Mougin, 1922; Zimmermann, 1936); among other things, they were unable to relate avalanche force to flow variables. Just after the devastating winters that struck the Alps in 1951 and 1954, the Swiss structural engineer Adolf Voellmy was commissioned to quantify avalanche forces. Based on field observations of damage to constructions, he published a series of four papers, in which he set out the first complete theory for computing avalanche velocities and forces depending on the flow regime (Voellmy, 1955d; Voellmy, 1955c; Voellmy, 1955b; Voellmy, 1955a). He ended up with a pressure distribution in the form:

$$p = \rho_m \left(gh + C_D \frac{1}{2} v^2 \right), \tag{1.2}$$

where ρ_m denotes the snow bulk density upon impact, g is the gravitation acceleration, h is the avalanche flow depth, v its velocity, and $C_D = 1-(v_u/v)^2(1-\sin\beta)$ is the drag coefficient, v_u is the impact velocity, and β is the angle of incidence between the flow direction and impacted surface. The impact pressure involves two contributions: a hydrostatic-like contribution $\rho_m gh$, and Bernoulli-like contribution $\frac{1}{2}\rho_m v^2$ weighted by the drag coefficient C_D. A decade later, considering that snow behaves as a cohesionless granular material, whose critical states can be described using Rankine's theory, Salm (1967) obtained this expression for the mean flow pressure far from any obstacle

$$p = \kappa\rho\left(gh\cos\theta + \frac{h}{R}v^2\right) \tag{1.3}$$

where ρ denotes snow density, R is the ground's radius of curvature, θ is the ground slope, and κ is the active/passive earth coefficient. In that case, the quadratic term in the pressure reflects centrifugal effects. Comparing Eqs. (1.2) and (1.3) shows that, for a flow past an obstacle, the pressure distribution is altered due to snow compaction and momentum transfer from the flow to the obstacle.

For subsequent developments, it is instructive to rearrange equation (1.2) by using the Froude number $Fr = v/\sqrt{gh}$:

$$p = C_D\frac{\rho_m}{2}v^2\left(1+\frac{2}{C_D}\frac{1}{Fr^2}\right) \tag{1.4}$$

In analogy to hydraulics, where the Froude number is used to distinguish between supercritical ($Fr > 1$) and subcritical ($Fr < 1$) flows, authors have suggested that this number can also be used to partition the avalanche flow regimes (Voellmy, 1955b; Salm, 1966; Salm, 1967; Mellor, 1968; Bozhinskiy and Losev, 1998; Ancey and Bain, 2015): the inertia-dominated regime—initially called shooting flow (*schiessender Abfluss*) by Voellmy (1955b)—refers to fast-moving avalanches, while the gravity-dominated regime—also called streaming flow (*strömender Abfluss*—refers to slow-moving avalanches. Whereas in hydraulics there is a neat separation between supercritical and subcritical flows at $Fr = 1$, the situation is less clear for avalanches. Salm (1967) suggested that the transition between the inertia- and gravity-dominated regimes occurs at a Froude number $Fr = \sqrt{\kappa\cos\beta}$. Other authors have assumed that the critical Froude number is unity.

For many scientists and practitioners, fast-moving avalanches were long perceived as the most dangerous ones, and this is why emphasis was mainly placed on this flow regime in developing guidelines for computing avalanche features (Burkard et al., 1990; Mears, 1992; Jóhannesson et al., 2009; Rudolf-Miklau et al., 2014; Margreth et al., 2015). For high-speed flow avalanches, we typically have $v = O(10-30)$ m/s and $h = O(1-5)$ m, which leads to Froude numbers in the 1.5–10 range. Authors have thus considered that the Bernoulli-like contribution in equation (1.2) is dominant. Field data have led to drag coefficients in the 1–10 range (Roch, 1980; Burkard et al., 1990; Norem, 1990; Gauer and Jóhannesson, 2009; Rudolf-Miklau et al., 2014). On rarer occasions, guidelines provide empirical equations for computing avalanche pressure depending on flow regime (Ancey, 2006; Ancey and Bain, 2015). Since the studies undertaken by Haefeli (1948) on snow plasticity, it has been observed that the snow pressure on an obstacle depends on the obstacle's size, a feature not predicted by equation (1.2) or equation (1.3). For creeping snow on a cylindrical obstacle of diameter d, Haefeli (1939) and Haefeli (1951) found that the hydrostatic-like pressure should be weighted by an empirical factor he called the efficiency factor $\eta_F = 1 + ch/d$, with $c \sim 0.6$ (see Appendix D in (Ancey and Bain, 2015)). The extension of Haefeli's theory to flow avalanches has long been debated.

With the equipment at several field sites across Europe (Issler, 1999), high-accuracy pressure data have been acquired and have shed new light on how avalanche impact pressure is related to the flow variables v and h. From the Col du Lautaret Pass (France) data, Thibert et al. (2008) deduced that the drag coefficient varied as a power law of the Froude number:

$$C_D = 2(1-\cos\alpha)AFr^{-n} \tag{1.5}$$

for a wedge-shaped obstacle whose apex angle is 2α, $A = 10.8$ and $n = 1.3$. Later, Thibert et al. (2013) used the analogy between snow avalanches and granular flows to propose an extended version

$$C_D = C + KFr^{-2} \tag{1.6}$$

where C and K are functions of the obstacle geometry, as well as avalanche flow depth and material properties that were calibrated from laboratory experiments (Faug, 2015). Analyzing data from the Ryggfonn site (Norway), Gauer et al. (2008) suggested that the drag coefficient could be written as

$$C_D = C_{d0} + \frac{f}{Fr^2} \tag{1.7}$$

where C_{d0} is a constant and $f \approx 4.8\sqrt{h/d}$ (Gauer and Jóhannesson, 2009; Gauer and Kristensen, 2016). At the Vallée de la Sionne field site (Switzerland), Sovilla et al. (2008a) observed that the assumption of a constant drag coefficient was not realistic, especially for subcritical avalanches for which the drag coefficient varies as $C_D \propto Fr^{-n}$ and thus becomes much larger than unity when $Fr \to 0$. Sovilla et al. (2010) observed a linear pressure distribution across the flow depth $p = \zeta\rho g(h-z)$, where z is the height relative to the ground and ζ is a fitted coefficient in the 7.2–8.1 range, but further measurements showed a strong dependence of ζ on the obstacle size and snow consistency (Baroudi et al., 2011; Sovilla et al., 2016).
In Figure 2.2 (chapter 2), we show two typical examples of the hydrostatic-like and the Bernoulli-like pressure distributions together with the corresponding velocity profiles measured at the pylon in Vallée de la Sionne.

1.3 Insights from experiments and Discrete Element Method simulations of flowing granular materials

Since Salm's work in the 1960s, the analogy between avalanches and granular flows has been used to gain insight in the bulk dynamics of dense avalanche flows (Scheiwiller and Hutter, 1982; Salm and Gubler, 1985; Hutter, 1996). Thereafter the analogy was used e.g. to derive equation (1.6) (Thibert et al., 2013), or to identify the flow-depth proportional pressure contribution from field measurements (Wieghardt, 1975; Albert et al., 1999; Sovilla et al., 2010). In addition to experimental investigations, the behavior of granular flows is often studied by performing simulations using the Discrete Element Method (DEM), as this method is particularly well suited to study granular materials (Andreotti et al., 2013). Figure 1.2 visualizes the interaction of a real and a simulated supercritical avalanche interacting with the Vallée de la Sionne pylon (section 4.2.2) in the upper and the lower half, respectively.

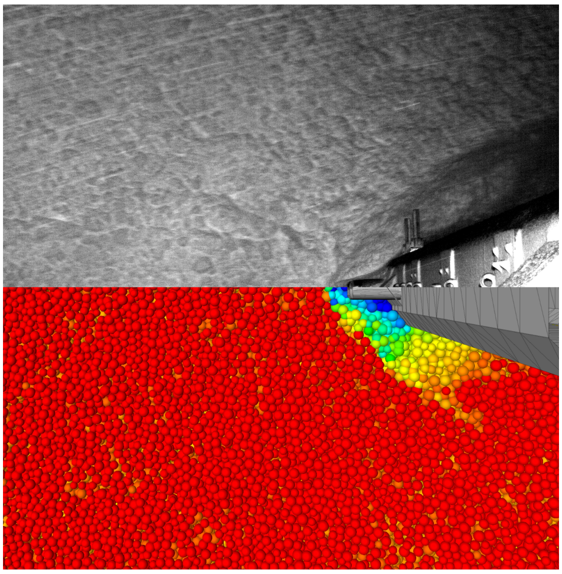

Figure 1.2 – Top view of a supercritical avalanche flowing around the Vallée de la Sionne pylon. The upper half shows a picture taken by a camera mounted on the pylon. The lower half shows a sample DEM simulation, where the particles are colored according to the velocity with red corresponding to high velocities and blue corresponding to low velocities.

Because in DEM the contact model governs the behavior of interacting particles, a suitable contact law is of prime importance to appropriately model a specific granular material. In our case, we want to mimic the complex and cohesive material behavior of snow.

On a microstructural level, the load on a snow sample is carried by the force chains through sintered joints connecting the individual ice grains (e.g., Ballard and McGaw, 1965; Gubler, 1978). These sintered joints are thus the origin of snow cohesion. However, most existing contact laws for cohesive granular media (Tomas, 2003; Roy et al., 2016) focus on the industrial handling of powders or wetted grains, where the cohesion originates typically from van der

Waals forces or liquid menisci between the particles (Rognon et al., 2008b). Hence, these models are not suitable for snow, because snow grains have no attractive force towards each other and only sinter if the particles are in physical contact (Szabo and Schneebeli, 2007). Although there exist cohesive contact law which captures elastic-plastic repulsion, dissipation, friction, as well as rolling and torsional resistance (e.g. Luding, 2008), no contact law has been developed specifically for snow so far. Steinkogler et al. (2015) were able to mimic the sintering and granulation processes of real snow in a concrete tumbler using DEM with a contact-bond model. In a similar contact model, the *parallel-bond* model originally developed for rock modeling (Potyondy and Cundall, 2004), the cohesive particle contact is modeled as a rigid joint sustaining compressive, tensile, bending and torsional loading. While this contact model has proven to be suitable to simulate other cohesive geomaterials, such as wetted sand (Butlanska et al., 2009) and debris (Kang and Chan, 2018), it was also successfully used to model snow (Gaume et al., 2015b; Bobillier et al., 2020).

Although the mechanics of granular flowing material was already studied as early as 1852 (Hagen, 1852) (see Tighe and Sperl, 2007), it only became an active field of research in the late 20th century (GDR-MiDi, 2004). Initially research focused on cohesionless granular materials (Forterre and Pouliquen, 2008; Moriguchi et al., 2009; Faug et al., 2009). Fundamental studies led to the identification of a unique frictional constitutive law describing the rheology of flowing cohesionless granular materials (GDR-MiDi, 2004; Cruz et al., 2005; Jop et al., 2006; Forterre and Pouliquen, 2008). To characterize the dynamics of granular free surface flows down inclined planes often the Froude Number Fr is used similarly to hydraulics (section 1.2). Later, many of the concepts for cohesionless flows could be extended for the more complex behavior of cohesive granular materials (e.g., Rognon et al., 2008b; Roy et al., 2017).

Previous research shows that the force exerted by a granular flow on an obstacle originates from force chains forming between jamming particles (Albert et al., 2000; Geng and Behringer, 2005). On the particle scale, the flow–obstacle interaction dynamics are therefore governed by the coexisting formation and destruction of these force chains extending upstream of the obstacle into the flow. Cohesion is known to increase the persistence of the force chains and the contact network density (Rognon et al., 2008b; Favier et al., 2013). On the macroscopic scale, the strong force chains originating from the obstacle form a region which is referred to as the *mobilized domain (MD)* by some authors (e.g., Thibert et al., 2013; Faug, 2015; Sovilla et al., 2016). Hence, the MD is the region in a granular flow encountering an obstacle, which experiences a significant increase in the contact forces between particles. Presumably, the macroscopic force experienced by the obstacle is therefore governed by the properties of the MD (Faug, 2015).

To our knowledge, the MD has only been described in a few studies, and the authors provided little information on the implications for the drag force on the obstacle (Chehata et al., 2003; Favier et al., 2009b; Faug, 2015). Chehata et al. (2003) suspect that the drag exerted on an obstacle is the result of compressive stresses acting on the MD. Revisiting a large number of studies on the macroscopic force on obstacles, Faug (2015) proposes a phenomenological model to calculate the force, considering a kinetic, a gravitational and an apparent weight contribution.

However, to the best of our knowledge, a detailed study about the MD properties and the resulting impact pressure for different flow regimes and types of obstacles is still lacking.

1.4 Research question and chapter outline

In recent decades, growing evidence has accumulated that Voellmy's physical intuition was correct. Field measurements have confirmed that when an avalanche impacts a rigid structure, it exerts a force that can be decomposed into hydrostatic-like and Bernoulli-like contributions, similar to Voellmy's equation (1.4). Although this overall pattern seems robust, there is no consensus on the origin and correct choice of the empirical proportionality factors for the two contributions to calculate the impact pressure depending on different the flow regime, snow consistency, obstacle size and shape. To address these uncertainties and to advance towards physics-based calculation of dense avalanche impact pressure on obstacles, we formulate the following research questions for the present thesis:

- How can the snow avalanche–obstacle interaction be simulated with the Discrete Element Method?
- What are the dominant physical avalanche–obstacle interaction processes?
- What role does the mobilized domain play in the build-up of avalanche impact pressure?
- What is the influence of varying flow regimes and snow properties, e.g. cohesion, on the impact pressure?
- What is the influence of the obstacle geometry on the impact pressure?
- How can the proportionality coefficients of the hydrostatic-like and Bernoulli-like contributions be estimated based on physical considerations?

In chapter 2, we describe the novel simulation setup, which we implement to tackle the research questions using the Discrete Element Method to numerically simulate the interaction of avalanches and obstacles. In the same chapter, we vary the velocity and cohesion of the avalanche interacting with the measurement pylon in the Vallée de la Sionne experimental site to identify the prevalent interaction processes for different avalanche scenarios.

In chapter 3, we focus on the interaction of gravitational flows and obstacles to investigate on the physical processes governing the empirical factor ζ. To find the link between the MD properties and the impact pressure, we perform 30 simulations with obstacles of different cross-sections and widths, as well as cohesive and cohesionless gravitational avalanche flow scenarios. In chapter 4, we expand the previous study from chapter 3 to also include inertial flows and also investigate on how the pressure is distributed on the obstacle impact surface (section 4.5).

Based on the results of chapters 2–4 and previous research, we propose a physics based practical approach to estimate C_D for varying avalanche flow regimes and obstacle geometries (section 4.6). We test the relevance of the proposed calculation method by comparing the calculated impact pressure to measured and simulated impact pressure values in different flow regimes and for different obstacle geometries.

In chapter 5, we summarize the individual chapter's results by highlighting the inference of the identified pressure build-up processes from the conceptual level of a flowing granular medium interacting with an obstacle, to the practical calculation of the impact pressure relevant for practitioners.

Chapter 6 gives an outline of work that could be performed in the future to further improve the physical understanding of avalanches interacting with obstacles and the impact pressure calculation procedure.

2 The role of inertia, friction and cohesion in the pressure build-up on the Vallée de la Sionne measurement pylon

Authors

M. L. Kyburz[1,2], B. Sovilla[1], J. Gaume[1,3], C. Ancey[3]

[1] WSL Institute for Snow and Avalanche Research SLF, Davos, Switzerland
[2] Environmental Hydraulics Laboratory, École Polytechnique Fédérale de Lausanne, Lausanne, Switzerland
[3] Snow and Avalanche Simulation Laboratory SLAB, École Polytechnique Fédérale de Lausanne, Lausanne, Switzerland

Publication

This chapter is a modified version of the publication:
Kyburz M.L., Sovilla B., Gaume J., Ancey C.: Decoupling the role of inertia, friction, and cohesion in dense granular avalanche pressure build-up on obstacles. Journal of Geophysical Research: Earth Surface 125(2), e2019JF005192 (2020). https://doi.org/10.1029/2019JF005192

Authors' contributions

Michael L. Kyburz: Conceptualization, Methodology, Software, Formal Analysis, Investigation, Visualization, Writing - Original Draft; **Betty Sovilla:** Funding Acquisition, Conceptualization, Experimental Data Curation & Investigation, Writing - Review & Editing, Supervision; **Johan Gaume:** Methodology, Writing - Review & Editing; **Christophe Ancey:** Writing - Review & Editing, Supervision.

2.1 Chapter summary

In this chapter, we aim to better understand how cohesion, friction, velocity and their interplay affect avalanche pressure build-up on structures. This is achieved by simulating the avalanche–obstacle interaction with a newly developed numerical model based on the Discrete Element Method (DEM), using a cohesive bond contact law. We test the relevance of the model by comparing simulated impact pressures with field measurements from the Vallée de la Sionne experimental site. Our results show that at the macro-scale, impact pressure consists of the inertial, frictional and cohesive contributions. The inertial and frictional contributions arise due to the existence, shape and dimension of the mobilized domain. The cohesive contribution increases the particle contact forces inside the domain, leading up to a doubling of the pressure. Based on these physical processes, we propose a novel scaling law to reduce the problem of calculating the pressure induced by cohesive flows, to the calculation of cohesionless flows.

2.2 Materials and Methods

In this section we describe the recently developed DEM model we use to investigate the processes involved in avalanche–obstacle interaction. This model allows us to reproduce the flow of a granular medium, such as a snow avalanche, in the vicinity of the obstacle and to analyze the resulting impact pressure and flow behavior around the obstacle.

In the first part, we define the test case and present experimental data which we use for the comparison with the simulations. The second part outlines how we model snow with DEM. In the third section, we present the model setup. The fourth section summarizes the most important parameters used in the simulations. Finally, we describe how we compare simulated impact pressures to field measurements. This chapter's appendix A presents the details of the implementation of the numerical Discrete Element Method, the contact model, as well as the model setup and procedure.

2.2.1 Experimental data and test case

Over the past 20 years, a large set of field measurements has been collected at VdlS. Therefore, we choose the measurement data from this site as the test case to model avalanche flow and pressure in the present study. Among many other quantities, avalanche pressure and velocity are measured on a 20 m high pylon-like steel structure (Sovilla et al., 2010). The pylon is located on a flat slope beneath two couloirs, where avalanches releasing from a 1.5 km wide area converge (Ammann, 1999). Here, we use the term pressure to refer to the measured or simulated impact pressure on the obstacle, if not mentioned otherwise. At the pylon, the pressure is measured at the front of six cylinders distributed with 1 m vertical spacing (Sovilla et al., 2014). The velocity of the incoming flow is measured at the face of a wedge attached to the front of the pylon (Kern et al., 2010). These point measurements at the pylon are complemented by radar measurements, which provide information on the flow regime along the $\sim 2.5\,\mathrm{km}$ long flow path (Köhler et al., 2018b).

Based on radar measurement data from VdlS, avalanche flows have been reclassified recently into seven categories (Köhler et al., 2018b). This highlights the complexity of avalanche flows, which also strongly depend on the specific terrain and the snow properties. In this study however, we limit ourselves to two flow types, which are often observed at the VdlS test site, namely, the inertial shear flow and the gravitational plug flow regimes.

Field experiments have demonstrated, that in the inertial flow regime, which is mostly typical of fast and cold avalanches, the pressure is proportional to velocity squared. Throughout this paper, we refer to cold or warm avalanches as avalanches with prevailing snow temperatures below or above $-1\,^{\circ}\mathrm{C}$, respectively. Previous research suggests that snow undergoes dramatic changes at this temperature, which consequently influences avalanche flow dynamics (Steinkogler et al., 2015; Köhler et al., 2018b; Fischer et al., 2018). The dense flows of inertial avalanches at VdlS rarely exceed a flow height of $h = 2.5\,\mathrm{m}$ and often exhibit a sheared velocity profile (Kern et al., 2009). Typical velocities of the inertial dense flow at VdlS range from $10\,\mathrm{m/s}$ to $30\,\mathrm{m/s}$ (Sovilla et al., 2008a).

The gravitational regime is often observed for warm snow avalanches and features a linear pressure variation with flow depth. A typical gravitational plug flow avalanche flows at very low velocities up to a maximum of approximately $10\,\mathrm{m/s}$, at the pylon location. At the VdlS test site these avalanches can build up maximum flow heights of $5-7\,\mathrm{m}$ and exert pressures in the range of $100-500\,\mathrm{kPa}$ (Sovilla et al., 2016). However, at VdlS, the peak flow heights are rarely maintained over longer time spans, but decrease with time. Heights of $h \lesssim 4\,\mathrm{m}$ are more common for this kind of flow.

2.2.2 Modeling snow using the Discrete Element Method

Our model is implemented within the framework of Itasca's commercial PFC software. This software implements the DEM method based on the soft-contact algorithm (Cundall and Strack, 1979) for interacting discrete particles.

Because of limited computational power, the number of snow crystals involved in large avalanches is prohibitive to be resolved as individual discrete elements in the model. Therefore, we consider the discrete particles to correspond to small snow agglomerates rather than individual ice crystals. Hence, the radius of the particles in the simulations are normally distributed within the interval $32\,\mathrm{mm} \leq r_p \leq 48\,\mathrm{mm}$ corresponding to a mean value of $r_p = 40\,\mathrm{mm}$. According to field surveys, this corresponds to an intermediate granule size (Bartelt and McArdell, 2009; Sovilla et al., 2008a; Steinkogler et al., 2015). Because snow particles are not resolved individually, the material properties of the discrete elements in the model must correspond to the macroscopic properties of the snow granules rather than the ice properties at the crystal level.

In DEM, the material's characteristics are not only influenced by the particles' properties. The dynamical behavior is primarily governed by the contact model, which comes into play whenever two particles interact with each other. A suitable contact law is therefore of prime importance to mimic the flowing snow in an avalanche. In the present work, a parallel bond contact model (Potyondy and Cundall, 2004) is used to model the mechanical behavior of snow. The model consists of two components: (1) a classical linear viscoelastic component consisting of a spring and a dashpot in the normal direction and a spring and a coulomb friction limit in the tangential direction, as well as (2) an elastic-brittle cohesive bond in parallel to the linear component. The bond models the sintering and therefore cohesion of the real snow. Mechanically it acts like a beam connecting the particles and can sustain normal and shear forces as well as bending and torsional loads. Similar to the sintering in snow, also in our simulations we allow for new bonds to form if a new contact occurs between two unbonded particles. Because the bond is in parallel to the linear component, the cohesionless behavior is conserved in any case, such as after bond breakage before a new bond forms.

2.2.3 Modeling the interaction of the avalanche flow and structures

In order to perform a systematic study of the influence of velocity and cohesion on impact pressure, we aim to impose the flow of the granular material independently from the particle and contact properties in the DEM model. Therefore, we propose a setup which enforces the flowing granular material (e.g. snow) to match a specific vertical velocity profile.

To achieve this, we isolate a finite volume of particles around the obstacle. The computational domain is 28 m high (z direction) and is confined with a wall at the bottom. This bottom wall mimics the gliding surface on which the avalanche flows. Transverse to the flow (y direction), the domain is 7 m wide and is limited by a periodic boundary condition. In the streamwise direction (x direction), the domain is 10 m long and is limited by boundary walls, segmented in height (Figure 2.1 a, b). By moving the wall segments at different speeds at different heights, we can impose the velocity magnitude and profile to the particle volume. In this way the velocity past the obstacle can be controlled while also accounting for effects such as basal friction and shear dilatancy.

For the simulations, we use idealized plug and shear velocity profiles. In the gravitational plug flow, we impose a constant velocity over the whole flow height (Figure 2.1 a). In the inertial shear flow, the velocity increases linearly from the bottom to the free surface of the granular flow (Figure 2.1 b). Ranges for cohesion and velocity, velocity profiles and flow heights are given in Table 2.1.

Gravity points in the negative z direction. While the average slope in the region of the VdlS pylon is approximately 20°, this approximation can be justified in the context of our test case because the terrain up to 10 m upstream of the pylon is nearly flat.

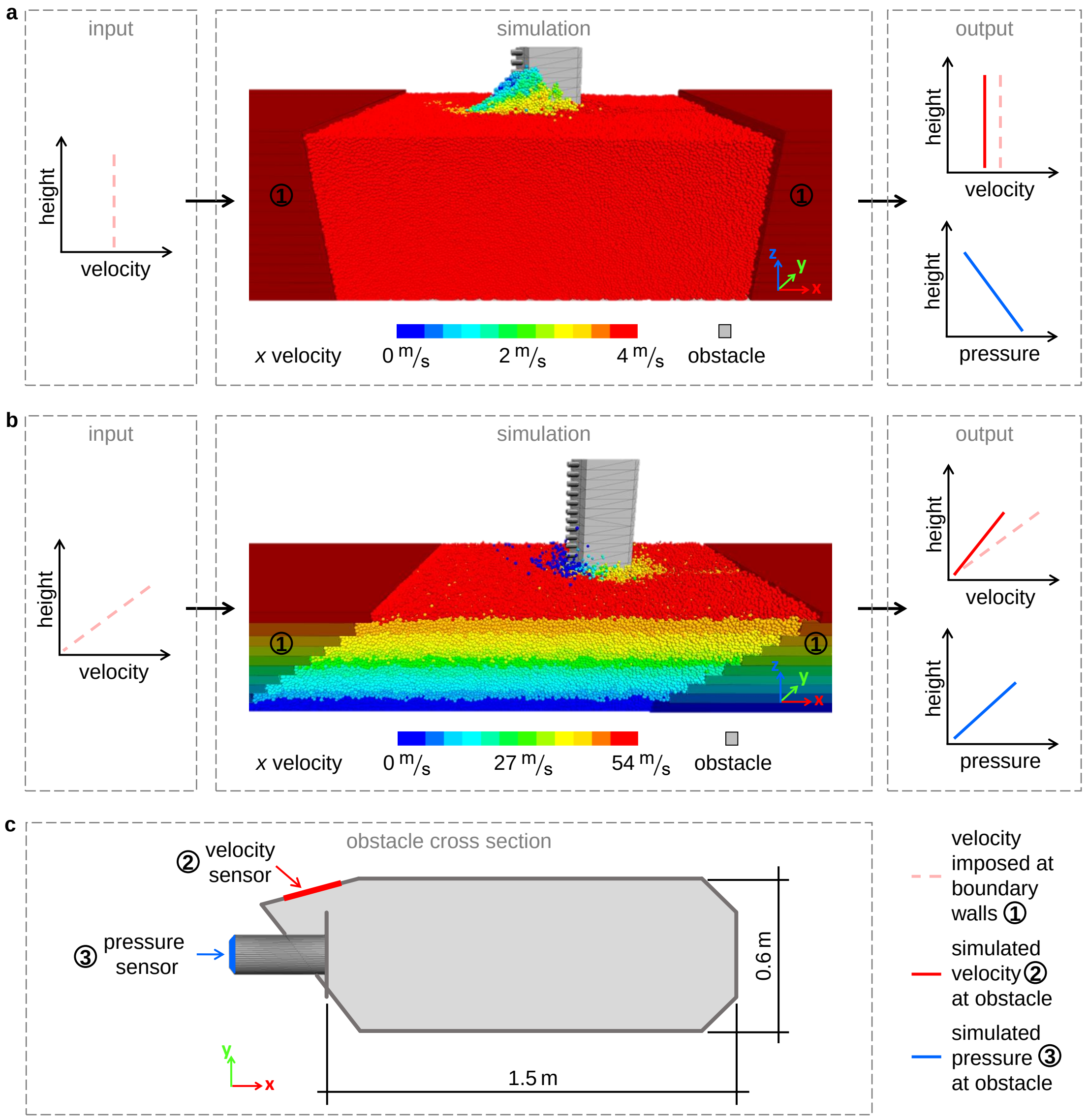
a
input
height
velocity
simulation
①
①
z
y
x
x velocity
0 m/s
2 m/s
4 m/s
obstacle
output
height
velocity
height
pressure
b
input
height
velocity
simulation
①
①
z
y
x
x velocity
0 m/s
27 m/s
54 m/s
obstacle
output
height
velocity
height
pressure
c
obstacle cross section
② velocity sensor
③ pressure sensor
y
x
0.6 m
1.5 m
velocity imposed at boundary walls ①
simulated velocity ② at obstacle
simulated pressure ③ at obstacle

Figure 2.1 – Panels a and b show the workflow for the DEM simulations of a plug flow and a shear flow velocity profile, respectively. The inputs of the simulations are on the left. The pictures in the middle show DEM simulations, where the boundary walls and the discrete elements are colored according to the velocity in the streamwise direction. The boundary walls and the static obstacle are shaded in gray. The outputs of the model are shown on the right. Panel c shows the cross section of the pylon with the location of the pressure and velocity sensors.

Figure 2.1 c shows a vertical cross section through the obstacle implemented in the simulation, which is similar to the measurement pylon in VdlS. In the simulation the pressure and the velocity are sampled at the same temporal frequency as in VdlS. The simulated impact pressure and velocity at the obstacle are also sampled at the same locations as in VdlS. The locations are highlighted in Figure 2.1 c in red and blue for the velocity and the pressure, respectively.

The simulated impact pressure is determined by summing up the face-normal component of all contact forces acting on the measurement surface and dividing it by the sensor surface area.

With the exception of the comparison of simulations and measurements (sections 2.2.5 and 2.3.1), we always use the imposed velocity at the wall. To compare different simulations, we always use a representative value of contact force, velocity at the pylon, imposed velocity, confining pressure and impact pressure, which corresponds to the value at mid flow depth.

2.2.4 Model parameters

While it is notoriously difficult to measure the mechanical properties of snow due to its heterogeneity (Gerling et al., 2017; Gaume et al., 2015a), even less is known about the mechanical properties of flowing snow in avalanches. As mentioned earlier, this applies particularly for cohesion, which is of central interest in the present study. Thus, most of the parameters and material properties applied in the simulations of this study are estimated rather than rigorously measured or calibrated with values within typical ranges as used and suggested by other authors for snow.

As mentioned in section 2.2.1, gravitational and inertial avalanches have different snow and flow properties. In the present article we want to focus on the influence of velocity and cohesion on the impact pressure. Hence, in our parametric study we only vary the cohesion as well as the flow height and the velocity according to the two flow regimes given in Table 2.1. Parameters such as the friction coefficient $\mu = 0.5$ (Steinkogler et al., 2015; Gaume et al., 2015b; Gaume et al., 2018a), Young's modulus E, particle radius r_p (section 2.2.2) and particle density $\rho_p = 500\,\mathrm{kg/m^3}$ of a single discrete element are constant in all simulations. In contrast to ρ_p, the bulk density ρ_b is the volumetric average density including voids between particles in a spherical control volume with a radius of $5.0 \cdot r_p$. Hence, ρ_b varies as a result of cohesion and shear rates, ranging from $370\,\mathrm{kg/m^3}$ to $430\,\mathrm{kg/m^3}$ in the gravitational plug flows and from $300\,\mathrm{kg/m^3}$ to $365\,\mathrm{kg/m^3}$ in the inertial shear flows. The ranges of these bulk densities agree well with the values from field and experimental studies (Platzer et al., 2007; Steinkogler et al., 2015; Bartelt and McArdell, 2009).

For the particles' Young's modulus, we use a value of $E = 10^5\,\mathrm{Pa}$ in all simulations, which is in the lower range of the values used by Gaume et al. (2015b) for modeling snow slabs and in the range of reported values from the literature (Shapiro et al., 1997; Gerling et al., 2017; Scapozza, 2004). For Young's modulus of the cohesive bond, we use the same value as for the particles. The cohesive strength of the bond is set to $\sigma_{coh.less} = 0\,\mathrm{Pa}$ for cohesionless simulations and varied between $0\,\mathrm{kPa} < \sigma_{coh} \leq 20\,\mathrm{kPa}$ otherwise. The upper limit corresponds roughly to the values reported by Shapiro et al. (1997) for snow with densities from $320\,\mathrm{kg/m^3}$ to $420\,\mathrm{kg/m^3}$ and is the same range as used by Gaume et al. (2015b). In the present study we use the local Bond number (equation (2.1)) instead of σ_{coh} to analyze the influence of the cohesive strength.

$$Bo = \sigma_{coh}/p_{conf} \tag{2.1}$$

This dimensionless number is the re-scaled cohesion, defined as the cohesive strength divided by the confining pressure p_{conf} (Roy et al., 2017), where the confining pressure is the vertical component of the local stress tensor $p_{conf} \equiv \sigma_{zz}$.
The parameters discussed here are summarized in Table 2.1.

Table 2.1 – Parameters for the DEM simulations in the gravitational and inertial regime

Parameter	Symbol	Unit	Gravitational plug flow	Inertial shear flow
Particle density	ρ_p	kg/m^3	500	500
Bulk density*	ρ_b	kg/m^3	$370-430$	$300-366$
Young's modulus	E	Pa	10^5	10^5
Cohesive strength	σ_{coh}	Pa	$0.0-2.0\cdot10^4$	$0.0-2.0\cdot10^4$
Friction coefficient	μ	–	0.5	0.5
Particle radius	r_p	mm	40 ± 8	40 ± 8
Depth-averaged velocity	v	m/s	$2-8$	$15-40$
Flow height	h	m	4.0	2.5

* The bulk density is not an input parameter, but is mentioned here for illustrative reasons.

2.2.5 Comparing simulated impact pressure profiles to field measurements

In this section we describe how we compare the simulated impact pressure and field measurements to test the DEM model's capacity to reproduce impact pressure measurements in a selected flow scenario. To reproduce a flow scenario, we impose a velocity profile at the boundary walls in the simulation, as depicted in Figure 2.1 a, b. The resulting velocity profile at the pylon directly dependents on the imposed one, but is slightly altered due to the presence of the obstacle influencing the flow.
On the condition that the simulated and the measured velocity profile at the pylon are similar, we can compare the resulting impact pressure profiles for this scenario. Hence, we use the velocity profile at the pylon as a boundary condition by matching the simulated and measured velocity profile. We therefore impose an idealized plug or shear velocity profile (section 2.2.3) such that the resulting velocity at the pylon closely matches the measured velocity. The only free parameter is the cohesion, which to date can not be measured in experiments and can only be estimated for the simulations (section 2.2.4). The other parameters in the simulations are kept constant as described in Table 2.1.

2.3 Results

The following section presents the results of our study on the influence of velocity and cohesion on the avalanche pressure on the VdlS pylon. The results are divided into four parts. In the first step, we compare the simulated impact pressure to field measurements of snow avalanches from VdlS to test whether the model proposed in section 2.2 is able to reproduce field measurements. Secondly, we show the results of the parametric study, where we vary velocity and cohesion in our simulation. There we analyze how impact pressure is influenced by changes in these two variables. In the third step, we analyse the flow around the obstacle at the micro-scale to better interpret and understand the influence of velocity and cohesion on the impact pressure. In the fourth step, we analyze the range of cohesion, the pressures and pressure fluctuations in gravitational avalanches with regard to the results from the previous sections.

2.3.1 Comparison of DEM simulations with field measurements

For the comparison of simulations with measurements, we select examples of field measurements of a gravitational plug flow and an inertial shear flow from the VdlS archive, respectively. In the case of the gravitational flow, we select measurements performed in a warm avalanche (archive number # 20103003 in the VdlS database), which released naturally on 30 December 2009. From these measurements we extract a short time sequence in the order of 0.5 s to obtain the pressure and velocity profile. In Figure 2.2 a these measurements are compared to a simulation with an imposed plug velocity profile of 10 m/s, a flow height of 4 m, resulting in the red velocity profile of ~ 8 m/s at the pylon (Figure 2.2 a, left panel). For the cohesive strength we choose a value of $\sigma_{coh} = 15.6\,\mathrm{kPa}$ which is high considering the range of σ_{coh} given in Table 2.1, as expected from a typical warm plug flow avalanche.

The qualitative trend of the simulated pressure profile agrees with the measured pressure profile, which increases linearly with the flow depth (Figure 2.2 a, right panel). However, the simulated pressure increases at a slightly higher rate near the free surface of the flow, and at a slightly lower rate below ~ 3.5 m than in the real-scale experiment.

In the case of the inertial shear flow we choose the measurement of avalanche # 20173032, which was released artificially on 08 March 2017. In Figure 2.2 b this measurement is compared to a simulation with a flow height of 2.5 m and an imposed shear velocity profile of 0 – 20 m/s, resulting in the red velocity profile at the pylon shown in Figure 2.2 b, left panel. Due to the idealization of the shear velocity profile as a linear profile, the simulated velocity profile shows small deviations with the measurements in the lower layers of the flow, at a flow height of ~ 1.0 m. For this scenario we choose a cohesive strength of $\sigma_{coh} = 1.25\,\mathrm{kPa}$. As it would be expected for an inertial shear flow, the selected cohesion is considerably lower than the one of the gravitational plug flow. The small mismatch between the measured and simulated velocity profiles does not seem to affect the pressure profiles in Figure 2.2 b, right panel. The two impact pressure profiles show a very good agreement.

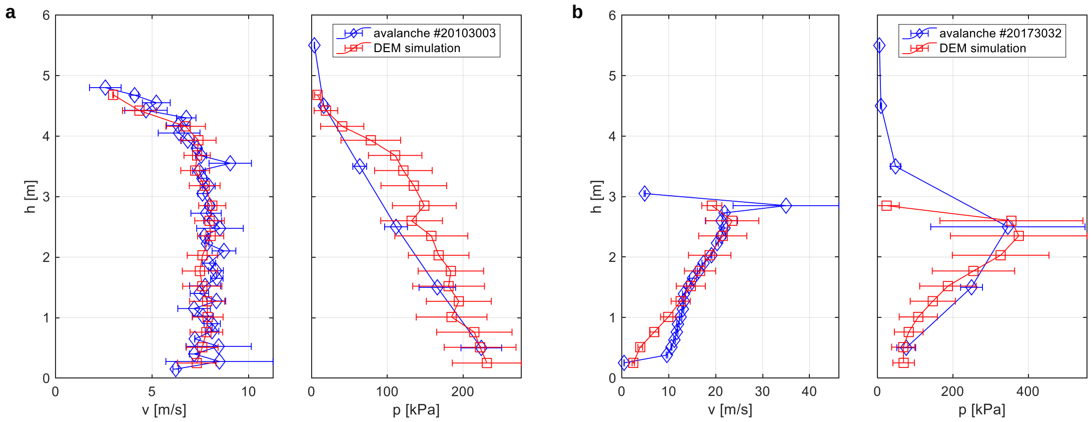

Figure 2.2 – Panels a and b show the comparison of simulated (red squares) and measured (blue diamonds) velocity and pressure profiles for an example of a plug flow and a shear flow, respectively. The error bars indicate the standard deviation from the mean value of the pressure or velocity. The interpolating lines between the data points are only a visual aid.

In order to test the relevance of our model in simulating the correct pressure for a larger range of velocities and cohesions, we vary the cohesive strength and velocity in our simulations according to the ranges given in Table 2.1.

In Figure 2.3, we compare the simulated impact pressures to field measurements of two avalanches (# 7226, # 6236, published by Sovilla et al. (2008a)). We can see that the simulated and measured impact pressure values in Figure 2.3 show good agreement over a wide range of avalanche velocities. For low velocities up to 10 m/s, the scatter of the simulated data is in the same range as the scatter of the measured data. The large scatter of the measurements for velocities higher than 10 m/s is very likely to be caused by the variability of the snow properties in the avalanches (Köhler et al., 2018a). The scatter in the simulations is smaller because many snow properties are kept constant (Table 2.1). Specifically, the scatter of the simulated impact pressure is caused only by the variation of cohesion, flow height or imposed velocity.

2.3.2 Influence of velocity and cohesion on impact pressure

In this section we analyze the influence of velocity and cohesion on impact pressure. For this purpose, we vary both quantities systematically in the ranges given in Table 2.1.

Figure 2.4 a shows the simulated impact pressures p on the obstacle plotted over a range of velocities. Here we plot the impact pressure of cohesionless simulations connected by the dashed black line, and the simulations with the strongest cohesion $\sigma_{coh} = 20$ kPa connected by the dash-dotted black line. We observe that the dashed and the dash-dotted line only vary little at slow velocities under 4 m/s, as found earlier for cohesionless granular materials (Albert et al., 1999; Wieghardt, 1975). For velocities higher than 8 m/s, the pressure increases gradually, for the cohesive and the cohesionless case.

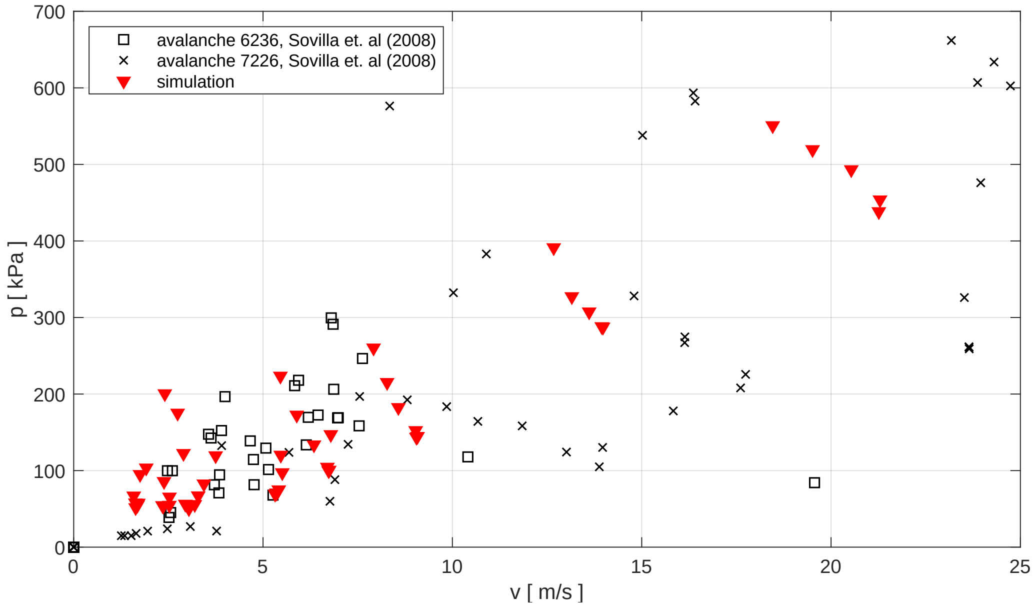

Figure 2.3 – Comparison of simulated (red triangles) and measured (black symbols) impact pressure versus velocity.

In this plot we identify three pressure contributions at the macro-scale. The contributions are separated by the black lines in Figure 2.4 a, and visualized by the colored areas in the inset. We define the first impact pressure contribution as the inertial contribution, which is proportional to velocity squared $p \propto v^2 \cdot \rho/2$ (Salm, 1966), similarly to the hydrodynamic impact pressure of inviscid fluids. This contribution is visualized in Figure 2.4 a by the blue area in the inset and the black solid line, which is calculated using a constant density $\rho = 300\,\mathrm{kg/m^3}$ as suggested by Burkard et al. (1990). In the log-log plot in Figure 4 a the slope of the cohesionless pressure curve (dashed line) reaches a maximum of 1.9 between 30 m/s and 40 m/s, very close to the theoretical value 2.0 given by the v^2 proportionality (solid line). Hence, Figure 2.4 a shows that $p \propto v^2 \cdot \rho/2$ is only a good approximation for the pressure of fast flows in the inertial regime ($v \gtrsim 20\,\mathrm{m/s}$).

For flows where $v \leq 15\,\mathrm{m/s}$, we observe that the lowest simulated pressures, which are connected by the dashed black line and correspond to cohesionless simulations, are well above the solid black line. Hence, we define the second contribution as the pressure difference between the dashed and the solid black line at a constant velocity, and refer to it as the frictional pressure contribution. It is highlighted with the yellow area in the inset. The frictional contribution arises due to the granular nature of the flow which we inherently simulate with DEM, in contrast to the flow of an inviscid fluid. The pressure increase due to this contribution is ~ 30 % (50 kPa) of the maximum pressure for $v < 8\,\mathrm{m/s}$ and decreases monotonically for $v > 8\,\mathrm{m/s}$. Hence, the frictional contribution is mostly relevant for gravitational flows ($2 \leq v \leq 8\,\mathrm{m/s}$).

The third pressure contribution is the cohesive contribution, visualized with the red area in the inset. We define it as the pressure difference between the dash-dotted and the dashed black line at a constant velocity. Thus, the cohesive contribution is the difference between impact pressure of a cohesive and a cohesionless simulation. While frictional processes between particles might still occur in the red area, they are less relevant with increasing cohesion because the cohesive bonds inhibit the relative movement between the particles. Hence, the increase in impact pressure is caused by the presence of cohesion in the granular material. From Figure 2.4 a we find that, for the maximum cohesion $\sigma_{coh} = 20\,\mathrm{kPa}$, the maximum pressure increase due to cohesion is 70 % (127 kPa) at 3 m/s and 14 % (70 kPa) at 40 m/s, respectively. Hence, similarly to the frictional contribution also the cohesive contribution is more relevant for gravitational flows than for inertial flows.

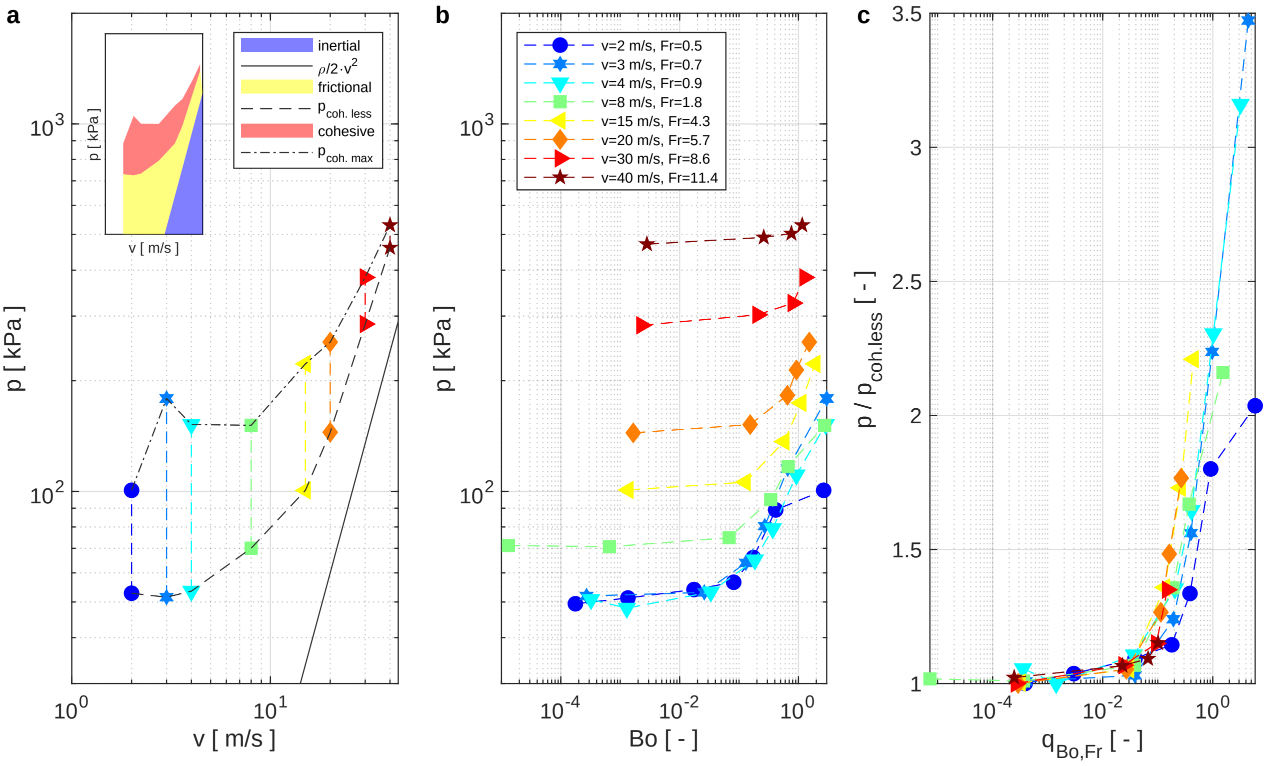

Figure 2.4 – Panel a shows the simulated pressure as a function of velocity with an illustration of the inertial (blue), frictional (yellow) and cohesive (red) pressure contributions in the inset. Panel b shows the simulated pressure for different Fr (colors) as a function of the Bond number. Panel c shows the pressure normalized by the corresponding cohesionless pressure plotted against the Bond to Froude number ratio $q_{Bo,Fr}$. In panel b and c the dashed interpolating lines between the data points are only a visual aid.

Figure 2.4 b shows the pressure plotted against the Bond number Bo to investigate the influence of cohesive strength on impact pressure. For all Fr values, we observe that at small Bo (equation (2.1)), pressure is a very weak function of Bo. In contrast, we find that for large Bo values the pressure is affected significantly by cohesion (Bo). For increasing velocity, and thus Froude number, the pressure curves are gradually shifted towards higher Bond numbers.

In order to obtain a more universal description of the pressure curves, we compensate for this shift by introducing a new dimensionless number, which is the ratio of the Bond and the Froude number $q_{Bo,Fr} = Bo/Fr$. In Figure 2.4 c, we normalize the absolute pressure p by the impact pressure of the cohesionless flow $p_{coh.less}$ at the same speed and plot it against $q_{Bo,Fr}$. By normalizing the pressure in this way, we consider only the pressure increase, which is caused by the presence of cohesion. As Figure 2.4 c demonstrates, the pressure data collapse almost onto a single curve for the suggested choice of normalization. The curves show that the pressure is amplified by cohesion predominantly for the flows with low velocities. The largest amplifications are observed at 3 m/s and 4 m/s, where the pressure of the cohesive flow is up to 3.5 and 3.2 times higher, respectively, than the pressure of the cohesionless flow.

2.3.3 Analysis of the mobilized domain and origin of the pressure amplification at the micro-scale

In order to understand the origin of the pressure amplifications, we analyze the flow around the pylon at the particle level (micro-scale) and compare selected simulations. First, we give a general overview of three scenarios with different velocities and cohesions. In the following subsections, we analyze the influence of velocity (Fr) and cohesion (Bo) separately.

We define the mobilized domain as the volume in the flow, where the contact forces between particles adjacent to the obstacle coherently exceed a threshold. With respect to contact forces, we consider only the force component normal to the contact plane. We define this threshold as the median of the contact forces in a control volume around the pylon. In the present analysis, the median of the contact forces is more representative of the undisturbed force level than the mean value because the mean is increased by very high force values in the mobilized domain.

Figure 2.5 shows the comparison of the mobilized domain for three sample simulations. The first and second rows show simulations of gravitational flows ($Fr = 0.9$) with no and strong cohesion, respectively. The third row shows the simulation of an inertial flow ($Fr = 11.4$) with strong cohesion.

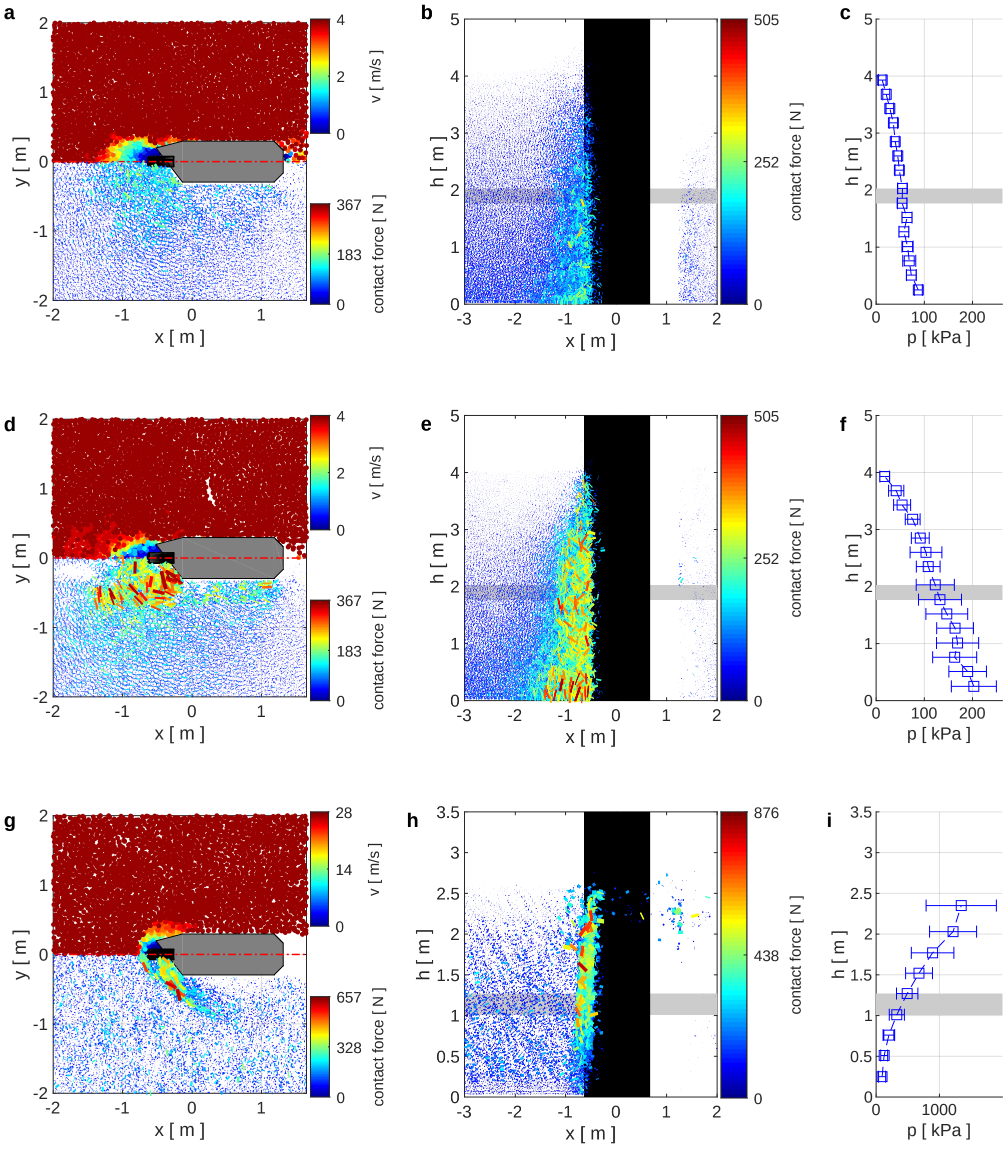

Figure 2.5 – Analysis of the flow and contact forces around the pylon at the micro-scale. Panels a–c show a gravitational flow ($Fr = 0.9$) with no cohesion ($\sigma_{coh} = 0.0$ kPa). Panels d–f show a gravitational flow ($Fr = 0.9$) with high cohesion ($\sigma_{coh} = 10.0$ kPa). Panels g–i show an example of an inertial flow ($Fr = 11.4$) with high cohesion ($\sigma_{coh} = 10.0$ kPa). Panels a, d and g show a horizontal section view through the flow in the middle of the flow height as indicated by the gray area in the other panels. The upper half in Panels a, d and g shows the velocity distribution. The lower half shows inter-particle contact forces whose strength is visualized through the line thickness and color. Panels b, e and h show the vertical section view in x-z plane located in the middle of the pylon (red dash-dotted line in panels a, d and g). The extent of the pylon is visualized by the black area. Panels c, f and i show the impact pressure profiles with the standard deviation of the temporal pressure fluctuations from its mean value indicated by the error bars.

In panels a, d and g we find that force chains stronger than average are only observed in the same region where the velocity of particles is reduced due to the presence of the obstacle. Indeed, the mobilized domains in the velocity field and the contact forces agree well in terms of size and shape.

For the two gravitational examples (first and second rows), the mobilized domain has an almost circular shape and is located upstream of the obstacle. Qualitatively, the contact forces in the mobilized domain away from the pylon increase from top to bottom in both panels b and e in Figure 2.5. This increase is even more pronounced in the mobilized domain in the vicinity of the obstacle. Not only do the contact forces increase with increasing depth below the surface of the dense flow, but the mobilized domain also grows larger in size. In the simulation with strong cohesion (panel d, $\sigma_{coh} = 10.0\,\mathrm{kPa}$), the mobilized domain is considerably larger and contact forces are stronger than in the cohesionless case (panel a, $\sigma_{coh} = 0.0\,\mathrm{kPa}$).

In the inertial flow (panel g, $\sigma_{coh} = 10.0\,\mathrm{kPa}$), we observe very strong contact forces only in the vicinity of the obstacle. The shape of the mobilized domain is similar to a bow shock at the leading edge of the pylon.

When comparing the pressure profiles in panels c and f to the panels b and e, we observe higher pressure at the bottom or for high cohesion, where the mobilized domain and contact forces are larger. Aside, the increase in the pressure itself, pressure fluctuations also increase in the flow with high cohesion. In contrast, for the inertial flow regime (panels h–i), the strongest contact forces and pressures are located at the top where the flow velocity is the highest.

Influence of the Froude number on the mobilized domain and impact pressure

In Figure 2.5, we show that the geometry of the mobilized domain varies in different scenarios. Here we want to examine how the shape changes when varying Froude numbers. To exclude the influence of cohesion we only consider cohesionless simulations.

Figure 2.6 a shows the mean contact forces as a function of distance from the obstacle (position 0) and for different Fr (colored symbols). Each point in the plot represents the local contact force averaged in volumes across the whole domain width at varying streamwise positions (x direction). The dotted lines in Figure 2.6 a indicate the median of the contact forces in the whole domain, which is used as the threshold for the mobilized domain as defined earlier.

Figure 2.6 a shows that the shape and location of the mobilized domain change as a function of the Froude number. This is visualized in panels b and c, which display the contact forces for the simulations corresponding to the Froude numbers $Fr = 0.5$ and $Fr = 11.4$, respectively. Similarly to Figure 2.5, we find a circle-shaped mobilized domain for the lowest Froude number $Fr = 0.5$ (Figure 2.6 b). Figure 2.6 c reveals that the mobilized domain is pushed downstream if the Froude number is increased. In this case strong contact forces concentrate just upstream of the obstacle. This leads to the sharp increase in the mean contact force in Figure 2.6 a for high Fr compared to low Fr.

To quantify the size of the mobilized domain in a single number, we use the standoff distance. Similarly to Faug (2015), we define it as the furthest point in the mobilized domain upstream of the obstacle's leading edge. Hence, the standoff distance defined here depends on the choice of the threshold which is used to distinguish between the free flow and the mobilized domain. However, even for a different thresholds, the definition of the mobilized domain with the median force proves to be very robust, and the standoff distance alters only marginally. Here, we use the standoff distance to compare the size of the mobilized domains across all cohesionless simulations. Figure 2.6 d shows that the standoff distance decreases dramatically from 1.84 m to approximately 1.0 m with increasing Froude numbers in the range of $0 \le Fr \le 5$. For $Fr > 5$, the values of the standoff distance level out at around 0.8 m.

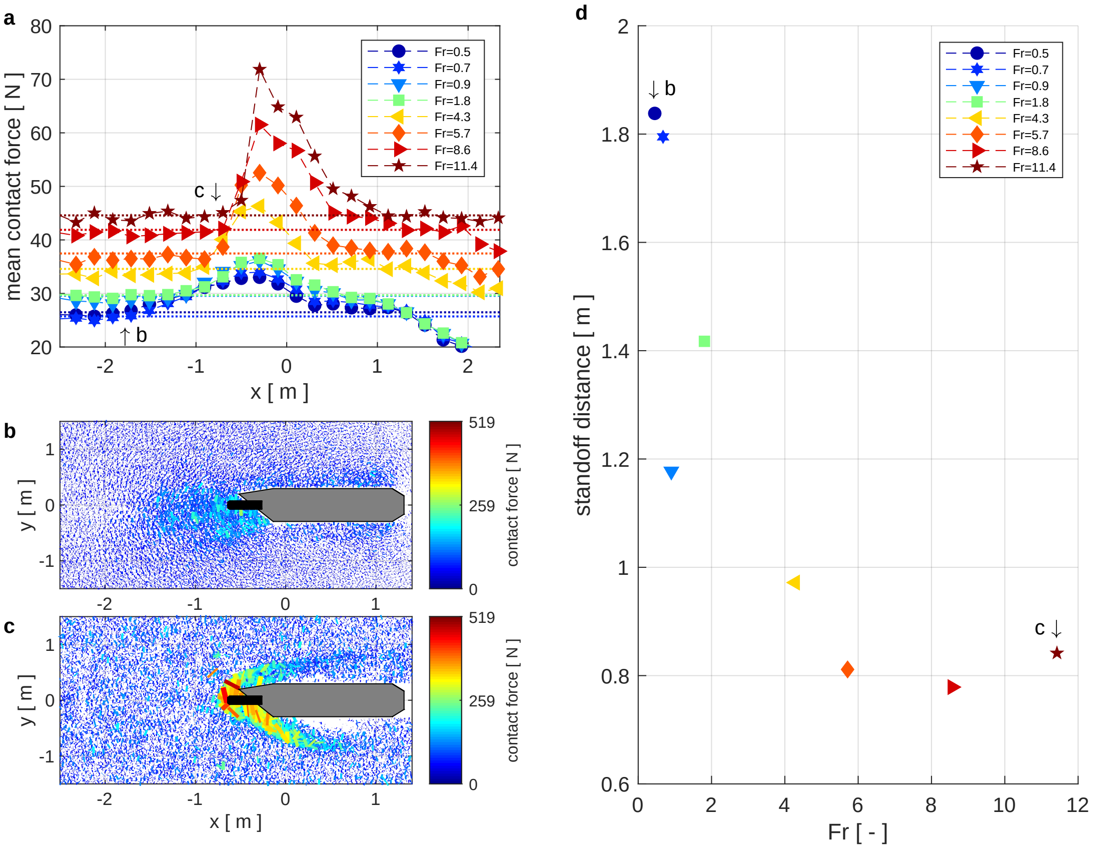

Figure 2.6 – Influence of the Froude number on the mobilized domain and the standoff distance. Panel a shows the mean contact force upstream of the obstacle in streamwise direction for different Froude numbers and $Bo = 0.0$. The dotted lines correspond to the median contact force in simulations with the same color. Panels b and c show horizontal section views at mid-height from the simulation with the lowest and the highest Froude number from panel a, respectively. The lines indicate the force chains whose strength is visualized through the line thickness and color. Panel d shows the standoff distances of the mobilized domain as a function of Fr for cohesionless flows.

Influence of the Bond number on the mobilized domain and impact pressure

In this section we investigate the influence of cohesion on the mobilized domain and the pressure on the obstacle. Similarly to the analysis in the previous subsection, we consider contact forces to be an indicator of the disturbance of the structure on the flow. However, here we only take contacts directly upstream of the structure into account, because these are considered the most relevant for pressure build-up. If a larger region in the y direction is considered, higher forces in the mobilized domain are averaged out and are therefore less evident. Figure 2.7 a shows the mean contact forces as a function of streamwise location for Bond numbers varying between $Bo = 0.0$ and $Bo = 3.0$. In panel a, the flow has a Froude number of $Fr = 0.7$. Again we consider the median of the contact forces as an indicator of the overall force level (dotted lines in Figure 2.7 a).

In contrast to Figure 2.6 a all curves in Figure 2.7 a have a similar shape. In addition, the standoff distance is almost constant around 1.5 m for all cases, and the dotted lines show that contact forces are enhanced by increasing cohesion. This is even more pronounced for local forces in the mobilized domain just upstream from the obstacle. There, the peak contact forces differ considerably more between low and strong cohesion than the median contact force. For the example of $Fr = 0.7$ given in Figure 2.7 a, the peak force (highest red triangle) is approximately 3 times higher than the median of the contact forces (red dotted line) for the highly cohesive case. In the cohesionless simulation, the peak value (highest dark blue circle) is only 2.5 times higher than the median contact force (dark blue dotted line). A sectional view of the flow around the pylon in the middle of the flow height illustrates this for the case with no cohesion (panel b, $Bo = 0.0$) and strong cohesion (panel c, $Bo = 3.0$). In these two pictures it is obvious that very strong cohesion heavily intensifies contact forces in the vicinity of the obstacle, while the shape and size of the mobilized domain remain largely unchanged. In panel c, the cohesion is so high that the granular material fails along clearly visible fracture lines.

In Figure 2.7 d, we compare the median contact force of all simulations with varying velocity and cohesion, and plot this as a function of the respective Bond number. Here we find that similarly to the pressure in Figure 2.4 b, the median contact forces also increase with increasing Fr. Moreover, the median contact forces also exhibit a weak dependency on Bo for low Bo values and a strong dependency for large Bo values.

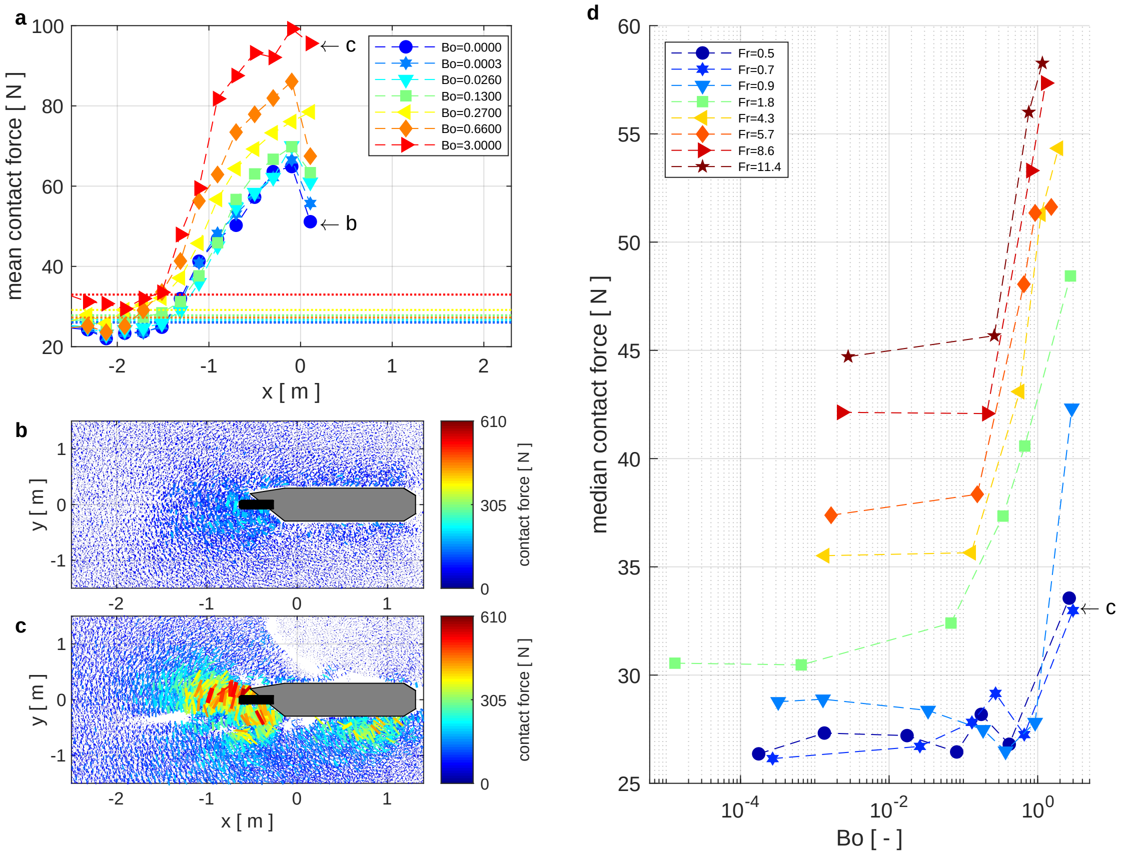

Figure 2.7 – Influence of cohesion on contact forces and the mobilized domain. Panel a shows the mean contact force upstream of the obstacle in streamwise direction for different Bond numbers (different colors and symbols) at $Fr = 0.7$. The dotted lines correspond to the median contact force in simulations with the same color. Panels b and c show horizontal section views at mid-height from the cohesionless case and the most cohesive simulation from panel a, respectively. The lines indicate the force chains whose strength is visualized through the line thickness and color. Panel d shows the median contact force as a function of Bo, and for different Fr (colors and symbols).

2.3.4 Pressure and range of cohesion in gravitational avalanches

As mentioned in section 2.2.4, we vary cohesion in simulations in the range of 0.0 kPa – 20.0 kPa. From Figures 2.4 c and 2.7 d we learn that pressure is only amplified by cohesion if a critical threshold of the Bond-to-Froude ratio is exceeded. By comparing simulated to measured pressures of gravitational avalanches, we aim to evaluate which range of cohesive strengths in our simulations can be used to reproduce the pressure values observed in reality. In Figure 2.8, we show the measurement data of three gravitational avalanches published by Sovilla et al. (2010) represented by the gray squares. In these measured warm dense avalanches, velocity ranges from 1 m/s to 8 m/s. The simulated pressure is colored according to the cohesive strength and has different markers for varying velocity. The temporal pressure fluctuations are illustrated by the error bars in panel a, and are separately plotted as a function of the flow height in Figure 2.8 b for all simulations of panel a.

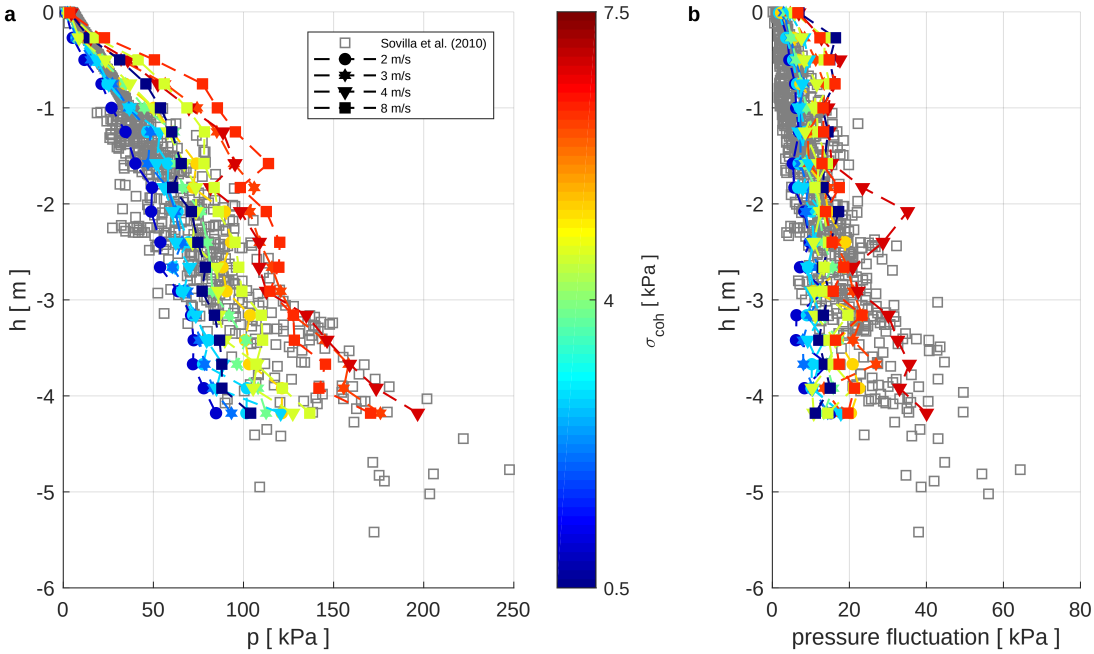

Figure 2.8 – Panel a shows the simulated (colored symbols) and measured (gray squares, from Sovilla et al. (2010)) pressure of gravitational avalanches on the VdlS pylon. Panel b shows the pressure fluctuations alone for the same avalanche and simulation data as in panel a.

We find in Figure 2.8 a that cohesive strengths in the range of 0.5 kPa – 7.5 kPa fit the measurement data well for the velocity range 2 – 8 m/s. The different symbols indicating velocity in Figure 2.8 a show that avalanche speed has very little influence on the pressure. In contrast, it is apparent from the colors, that flows with less cohesion exert lower pressures than flows with elevated cohesion.

Already in Figure 2.5, we observed that pressure fluctuations are larger in flows with higher cohesion. This trend is clearly confirmed by Figure 2.8 b. Similar to the measured fluctuations, fluctuations in the simulations also increase with increasing flow depth as well. Although Figure 2.8 b shows good overall agreement between measurements and simulations, the simulated fluctuations are greater than those from measurements at the flow free surface and increase less deeper within the avalanche. Similarly to the pressure itself, fluctuations are smaller and larger in simulations with little and high cohesion, respectively.

2.4 Discussion

2.4.1 Modelling avalanche–obstacle interaction with DEM

In section 2.2, we describe our newly developed DEM model to study the interaction between avalanches and structures. By comparing simulated pressure profiles and pressure profile from field measurements, we show that by treating avalanches as granular flows and applying the Discrete Element Method, the numerical model is able to reproduce flow-depth and velocity squared proportional pressure profiles as well as temporal pressure fluctuations. Furthermore, the simulated pressure values are in the same order as measured values over a wide range of avalanche velocity (Figure 2.3). Particularly at velocities lower than 5 m/s the simulated impact pressure values agree well with measurements from avalanches # 6236 and # 7226. Only at higher velocities we observe a significant difference between the scattering of the simulated and measured impact pressure. This is probably because we only vary few parameters (Table 2.1) in our parametric study.

Further limitations of the presented model become apparent due to the differences in pressures and pressure fluctuations between simulations and measurements (Figure 2.2 a, b and 2.8). Firstly, the current parallel-bond contact model does not allow for plastic compaction of the granular material. We assume that compaction influences not only pressure at the bottom of the avalanche flow, due to the weight of the snow above, but also across the whole flow height where the snow impacts the obstacle (Gauer and Jóhannesson, 2009). Secondly, variation in the radii of particles is small, whereas in natural avalanches, particles are typically larger at the surface of the flow due to particle segregation, which may affect the pressure distribution (Kern, 2000).

To obtain a broad understanding of the influence of cohesion in various avalanche scenarios we choose a large range of cohesion (0.0 kPa$\leq \sigma_{coh} \leq$ 20.0 kPa) values and apply it to the whole range of velocities (Table 2.1). We put these cohesive values into perspective by back calculating the cohesion range from four avalanche measurements. From the calculations and comparisons in sections 2.3.1 and 2.3.4, the measurements of these slow avalanches are found to correspond to cohesion values of 0.5 kPa$\leq \sigma_{coh} \leq$ 15.6 kPa in the simulations. Although the back calculated cohesion values agree well with values of tensile strength of snow reported by other authors (Mellor, 1974; Jamieson and Johnston, 1990; Shapiro et al., 1997; Yamanoi and Endo, 2002), they are probably only valid for the same choice of the other parameters stated in Table 2.1.

In this study, we used mechanical snow properties from the literature, which are mostly derived from studies on the mechanics of undisturbed snow. In contrast, avalanche snow may undergo large deformations and transitions (Steinkogler et al., 2015; Valero et al., 2015). Therefore, the stated values must be considered with care in the context of this study. Hence, in the future it would be important to collect data on the mechanical properties of snow granules from avalanches.

The qualitative trend of all results shown in this study have, however, proven to be very robust to changes in any of these parameters. For example, if ρ_p is increased, the absolute pressure value increases as well, but pressure proportionality with flow-depth and velocity squared and the trends shown in sections 2.3.2, 2.3.3 and 2.3.4 remain qualitatively the same. Given this qualitative robustness of the results to changes in the particle properties and because we use a standard cohesive contact model as well as a generic model setup, we believe that the physical understanding gained in this study may also be relevant for similar processes, where cohesive granular flows interact with rigid structures.

2.4.2 Impact pressure contributions at the macro-scale

In the inset of Figure 2.4 a, we visualize and highlight the inertial, frictional and cohesive impact pressure contributions. The complex interplay between these contributions in avalanche dynamics are investigated for the first time in this study. It is important to note that all three contributions are present for the whole range of Fr, but with changing importance as a share of the entire impact pressure.

The inertial contribution is known from other fields (e.g. fluid dynamics, granular flows) and is proportional to density and velocity squared. This v^2 proportionality is confirmed by the slope of the dashed black line in Figure 2.4 a, which is ~ 2 for high velocities ($v \gtrsim 20\,\mathrm{m/s}$). Hence, we confirm that avalanche pressure is governed primarily by inertial impact for Froude numbers close to or greater than 10 (Voellmy, 1955e; Thibert et al., 2008; Faug, 2015).

The frictional contribution is most pronounced at low Fr and arises due to the granular nature of the flow. It is, therefore, also present in cohesionless granular flows (Chehata et al., 2003; Albert et al., 2001). Thus, even a hypothetical cohesionless avalanche would exert considerably higher pressures on an obstacle at low Fr, compared to the inertial contribution alone.

The cohesive contribution is also highest at low Fr and constitutes up to 70 % of the entire impact pressure for the range of cohesion from Table 2.1. If we consider the range of back calculated cohesion ($0.5\,\mathrm{kPa} \leq \sigma_{coh} \leq 15.6\,\mathrm{kPa}$) the largest pressure amplification factor due to cohesion is 2.1 with respect to the cohesionless case. Furthermore, we show that cohesion is only relevant for a pressure increase above a certain threshold, where the slopes of the curves in Figure 2.4 b increase dramatically. The idea of a critical cohesion threshold is also supported by other studies (Favier et al., 2013; Steinkogler et al., 2015). Most likely, below this threshold the flow behaves similarly to a cohesionless flow as long as collisional forces are strong enough to break the cohesive bonds between particles. If the cohesive strength is above this threshold value, the bonds cannot be broken anymore by the collisional forces. Thus, the flow exhibits a cohesive behavior (section 2.3.3) and impact pressure is amplified.

Because the cohesion threshold is included in the range of the back calculated cohesion values we assume that real avalanches are most likely subject to this transition between cohesive and nearly cohesionless flow behavior. Similarly to the sharp transition of granulation behavior at the threshold temperature $-1\,^{\circ}\mathrm{C}$ reported by Steinkogler et al. (2015), we demonstrate that also here small changes in cohesion around the cohesion threshold, above which pressure is amplified, may lead to substantial changes in pressure.

We also observe that the cohesion threshold varies with Fr and assume that this is due to the competing effect of cohesive and inertial forces in the snow. We take this into account by defining the Bond to Froude ratio $q_{Bo,Fr}$. Moreover, we decouple the cohesive pressure contribution from the frictional and inertial contribution by normalizing the impact pressure of a cohesive flow with the cohesionless pressure. The collapse of the data from Figure 2.4 b onto a single curve in Figure 2.4 c shows that we find a scaling for the impact pressure of a cohesive granular as a function of the cohesionless pressure as well as Bo and Fr. This scaling allows us to estimate the impact pressure of a cohesive granular flow by calculating the pressure of cohesionless flow and multiplying by the factor given in the curve in Figure 2.4 c. This is expedient because the problem of cohesionless granular flow impacting an obstacle has been studied in the past (e.g. Albert et al., 2001).

2.4.3 Micro-scale processes of impact pressure build-up

In this study, we confirm the existence of the mobilized domain postulated by Faug (2015), even in cohesionless granular flows. Hence, the mobilized domain owes its presence to the granular nature and the force chains in the granular flow, rather than the presence of cohesion. Consequently, the mobilized domain in cohesionless flows is most likely the origin of the frictional pressure contribution (yellow area in inset of Figure 2.4 a).

Our results show that the shape of the mobilized domain can be described using the Froude number only. For low Fr, the domain has an approximately circular shape and is located mainly upstream of the obstacle (Figure 2.6 b). If the Froude number is increased, the mobilized domain is “pushed” gradually downstream by the flow. For the highest Froude numbers, the mobilized domain has the shape of a bow shock (Figure 2.6 c).

Here, we use the standoff distance (section 2.3.3) to characterize the extent of the mobilized domain. Figure 2.6 d shows that for increasing Fr, the standoff distance decreases dramatically from a maximum of ~ 2.0 m in the range of $Fr < 5$, and then levels out at around 1 m for $Fr > 5$. This result agrees qualitatively with the findings of Cui and Gray (2013) and Faug et al. (2002) on the standoff distance of granular bow shocks and size of mobilized domains, respectively. Interestingly, a similar dependency is found experimentally between the drag coefficient of a wall and Fr in a mud flow by Tiberghien et al. (2007), as well as for the hydrodynamic impact pressure of debris flows and Fr by Proske et al. (2011). Quantitatively, however, the maximum standoff distance in all simulations is considerably smaller than the 3.5 m−7.0 m estimated by Sovilla et al. (2016) using the theory of Faug (2015) for the same structure. Furthermore, it is important to bear in mind that the size of the mobilized domain and therefore the standoff distance probably differs substantially for other geometries.

We also show that cohesion neither influences the size, nor shape of the mobilized domain, but changes the level of the contact forces inside the domain. As a general rule, we observe that the median contact forces increase with increasing cohesion. Our results confirm the observations of Favier et al. (2013), who found that cohesion increase leads to a densification of the contact network and to an increase in the temporal contact persistency. Figure 2.7 d shows that the dependency of the median contact force and cohesion is not linear. Indeed, the median of the contact forces are almost constant for low Bond numbers but increase sharply if a particular Bo is exceeded. The resemblance of Figure 2.4 b to Figure 2.7 d clearly indicates that the pressure increase due to cohesion at the macro-scale is directly linked to the intensified contact forces at the micro-scale.

While further proof is needed, we assume that the frictional and cohesive contributions observed at the macro-scale can be linked to processes at the particle scale. The frictional contribution arises due to frictional and collisional processes between particles, which causes the mobilised domain to form around a structure due to jamming or building of force chains. Thereby, the force of the incoming flow probably acts on the larger apparent surface of the obstacle, which is the outline of the mobilized domain, and it is transmitted and concentrated at the obstacle surface through the force chains. By increasing the cohesion between particles, the force transmission from the apparent surface to the obstacle is enhanced, and results in higher pressure on the obstacle surface.

2.5 Conclusions

In this study we present a newly developed DEM model to investigate the interaction between dense snow avalanches and obstacles. We show that the model is able to reproduce the pressure profiles and the range of temporal pressure fluctuations exerted by avalanches on the VdlS pylon for a wide range of Froude numbers and cohesion values. This indicates that approximating avalanches as granular flows and applying DEM allows us to capture the most important physical processes involved in avalanche–obstacle interaction.

We also identify, however, some limitations of the model. Firstly, the contact model does not allow for compaction of snow, and particle segregation cannot occur because the particles are not flowing freely. Secondly, particle properties are estimated from values found in the literature, which are based on the mechanical behaviour of undisturbed snow samples. Hence, to obtain relevant results in future investigations on the mechanical properties and contact behavior of snow avalanche granules will be needed.

In our study we identify three pressure contributions, which are of varying importance depending on avalanche speed. The inertial contribution, which is proportional to velocity squared and density, is most important at high avalanche velocities. The frictional contribution arises due to the granular nature of the flow and is therefore inherently present in cohesionless flows. Hence, depending on the granulometry, the impact pressure of slow avalanches is increased by this frictional contribution even without the presence of cohesion, such as in cold avalanches. In agreement with previous studies, we find growing evidence that the formation of force chains and the existence of a mobilized domain around the structure in cohesionless flows are factors leading to elevated pressures at low Fr compared to the impact pressure in Newtonian fluids (Sovilla et al., 2010; Favier et al., 2013; Faug, 2015). The shape of this mobilized domain smoothly changes from a nearly circular shape upstream of the obstacle for low Fr, into a bow shock-like shape for high Fr.

The cohesive contribution increases the impact pressure of a cohesionless flow by a maximum factor of 2.1 if a critical cohesion value is exceeded, such as in warm avalanches. We find that this increase of impact pressure is caused by the amplification of contact forces within the entire cohesive flow, but especially within the boundaries of the mobilized domain. Surprisingly, the shape and size of the domain are barely influenced by cohesion as assumed in other studies (Faug, 2015; Rognon et al., 2008b).

Furthermore, we find a scaling relating the pressure of cohesive and cohesionless flows. This allows us to reduce the problem of calculating the pressure of a cohesive granular flow, to calculating the pressure of a cohesionless flow, which has been investigated in the past (Albert et al., 2001; Calvetti et al., 2017; Albaba et al., 2015; Moriguchi et al., 2009; Chanut et al., 2009). Thanks to the identification of the three pressure contributions at the macro-scale and the underlying processes at the particle level, this study contributes to our understanding of the build-up of impact pressure of cohesive granular flows on narrow structures. Finally, as we use a standard cohesive bond contact model and the qualitative results are not affected by changes of the properties of the granular material, we are convinced that this study may not only be relevant for snow avalanches, but for the interaction of structures and flows of cohesive granular materials in general.

Acknowledgments

Michael Kyburz, Betty Sovilla and Christophe Ancey acknowledge the Swiss National Science Foundation for funding this project “Pressure on obstacles induced by granular snow avalanches” (grant no. 200021_169640). Johan Gaume acknowledges financial support from the Swiss National Science Foundation (grant no. PCEFP2_181227). The supporting information and the code to be used with the Itasca PFC3D software to reproduce the data presented in this paper is available in the open access data repository Zenodo, which is financed by the Horizon 2020 project OpenAIRE and hosted by CERN. The associated entry can be accessed via Kyburz M. L., Sovilla, B., Gaume J., & Ancey C. (2019). Decoupling the role of inertia, friction and cohesion in dense granular avalanche pressure build-up on obstacles [Supporting Information]. Zenodo. https://doi.org/10.5281/zenodo.3239031. We would like to thank the Editor Ton Hoitink, the Associate Editor Michele Bolla Pittaluga, as well as Thierry Faug and two anonymous reviewers for their helpful comments.

3 The concept of the mobilized domain: how it can explain and predict the forces exerted by a cohesive granular avalanche on an obstacle

Authors

M. L. Kyburz[1,2], B. Sovilla[1], J. Gaume[1,3], C. Ancey[3]

[1] WSL Institute for Snow and Avalanche Research SLF, Davos, Switzerland
[2] Environmental Hydraulics Laboratory, École Polytechnique Fédérale de Lausanne, Lausanne, Switzerland
[3] Snow and Avalanche Simulation Laboratory SLAB, École Polytechnique Fédérale de Lausanne, Lausanne, Switzerland

Publication

This chapter is a modified version of the publication:
Kyburz M.L., Sovilla B., Gaume J., Ancey C.: The concept of the mobilized domain: how it can explain and predict the forces exerted by a cohesive granular avalanche on an obstacle. Granular Matter (2021)

Authors' contributions

Michael L. Kyburz: Conceptualization, Methodology, Software, Formal Analysis, Investigation, Visualization, Writing - Original Draft; **Betty Sovilla:** Funding Acquisition, Conceptualization, Experimental Data Curation & Investigation, Writing - Review & Editing, Supervision; **Johan Gaume:** Methodology, Writing - Review & Editing; **Christophe Ancey:** Writing - Review & Editing, Supervision.

3.1 Chapter summary

In this chapter, we want to assess whether the findings of the previous chapter 2 for the VdlS pylon, also hold for obstacles with other geometries and how the impact pressure depends on the processes at the particle scale in the vicinity around the obstacles. Hence, we investigate in more detail the origin of the force transmitted from the flow to the obstacle and what role the mobilized domain (MD) plays in the processes of pressure building up on the obstacle in subcritical avalanche flows. To achieve this, we simulate granular flows interacting with static obstacles with rectangular, circular and triangular cross-sections of widths between 0.24 m and 6.0 m using DEM and analyze the properties of the granular material inside the MD. Because in subcritical flows the impact pressure is independent of the velocity, we arbitrarily select a flow velocity of $v = 3\,\mathrm{m/s}$ corresponding to $Fr = 0.61$. In order to assess the influence of the cohesion on the impact pressure, we simulate a cohesive and cohesionless scenario for all combinations of obstacle widths and cross-sections. As compressive stresses may play an important role for the impact pressure (Chehata et al., 2003), we perform axial compression test with the same cohesionless and cohesive granular material to assess how the compressed material state in the MD is linked to the stress inside the material and on the obstacle.

Our results show that the impact pressure decreases non-linearly with increasing width regardless of the obstacle geometry. While the MD size is mostly proportional to the obstacle width, the pressure decrease for increasing width originates from the jammed material inside the MD. Thus, we provide evidence that the compression inside the MD governs the pressure build-up for cohesionless subcritical granular flows. In the cohesive case, we show that the enhanced stress transmission and increased compression of the material inside the MD causes the pressure increase compared to the cohesionless case. Finally, considering an inertial and a gravitational contribution, we are able to calculate the impact pressure based on the properties of the MD.

3.2 Materials and Methods

In this section we describe the methods and parameters used to simulate the interaction of granular flows and obstacles of various geometries and sizes. First, we present in detail the numerical setup and the simulation procedure. Second, we present the obstacle geometries for which we simulate the interaction with the granular flow. Third, we define the contact model, as well as the material and flow properties of the granular material used in our study. Fourth, we present axial compression tests showing how this material behaves under compressive loading. Finally, we present how we can distinguish the domain where the granular material flows freely from the domain where the flow is affected by the presence of the obstacle.

3.2.1 Simulation setup and procedure

The present model is implemented in the *PFC* Discrete Element Method (DEM) software from Itasca (Minneapolis, MN, USA), which is based on the soft-contact algorithm for the interaction of discrete spherical particles (Cundall and Strack, 1979).

In this study, we simulate granular flows with and without cohesion (section 3.2.3) interacting with obstacles of different geometries and sizes (section 3.2.2). As input for the simulation we want to impose the same boundary velocity of the granular material independently of the properties of the granular material and the obstacle geometry. Hence, we only simulate an isolated volume of granular material around an obstacle and impose the motion of the granular material at the up- and downstream boundaries. In the streamwise x direction the granular material is confined between either fixed particles or boundary walls, as shown in Figure 3.1. In the simulations with obstacle widths $w \leq 1.0$ m, we use a domain length of $D_x = 11$ m in the x direction. For wider obstacles we use $D_x = 22$ m. In the y direction transverse to the flow, the domain is limited by a periodic boundary condition and has a width of $D_y = 28$ m. We check that these domain sizes are sufficient to avoid strong force chains, and thus the MD originating from the obstacle, reaching the domain boundaries.

In the vertical, z direction the domain is $D_z = 28$ m tall. Because the granular material is subjected to gravity acting in the $-z$ direction, there is only a bottom boundary wall to confine the particles in the vertical direction.

When the flow first impacts the obstacle at the beginning of a simulation, the flowing material has yet to form the MD. Hence, to investigate how the impact pressure on an obstacle is physically linked to the flow around it, we need to obtain a continuous flow with a MD around the obstacle. In order to achieve this while minimizing the computational effort, we split the simulation procedure into two phases which we describe below. The first and the second phase are shown schematically in the upper and the lower half of Figure 3.1, respectively. While the particles can flow around the obstacle in our 3D setup, Figure 3.1 shows in sectional a view in the x-z plane in the middle of the flow domain.

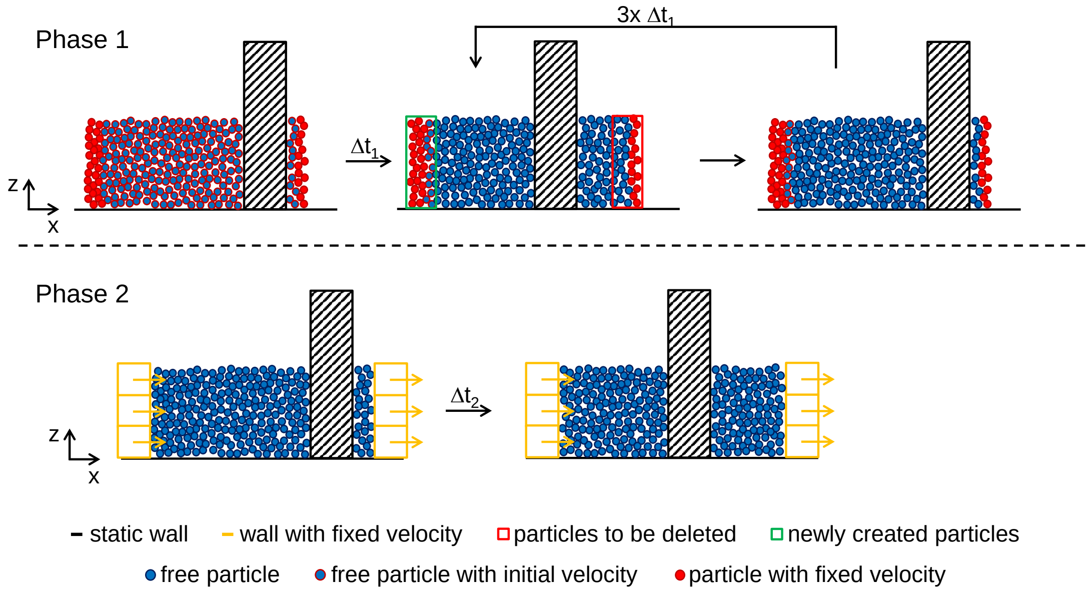
Phase 1
$3x\ \Delta t_1$
Δt_1
z
x
Phase 2
Δt_2
z
x
▬ static wall
▬ wall with fixed velocity
☐ particles to be deleted
☐ newly created particles
● free particle
● free particle with initial velocity
● particle with fixed velocity

Figure 3.1 – Simulation procedure in two phases. First phase (top) with continuous particle generation and deletion at the boundaries. Second phase (bottom) where the flow is imposed by the boundary walls.

In the first phase we establish the flow of the granular material around the obstacle. In the beginning all particles are assigned an initial or boundary velocity in the streamwise x direction (particles with a red outline in Figure 3.1). During a simulation period Δt_1 the velocity of the particles at the up- and downstream boundary (particles with a red outline and fill) is fixed at the boundary velocity in the x direction, and at zero in the y and z directions. The rest of the particles are free to move according to the interaction with other particles or the obstacle (particles with blue fill). Hence, the boundary particles push the freely moving particles in the flow direction past the obstacle.

After the simulation period Δt_1 the simulation is paused and the fixed velocity condition is released for all particles. Particles beyond the downstream boundary are deleted (red outline). At the upstream boundary the domain is filled with newly generated particles (green outline). The newly generated particles are again assigned the initial velocity. Again, the velocities of the particles at the up- and downstream boundaries are fixed (particles with red outline and fill), while the particles further from the boundary move freely. Subsequently another period Δt_1 is simulated. To develop the MD around the obstacle, we repeat this procedure three times. However, the generation of new particles in the first phase causes fluctuations in the system. Because we want to obtain a continuous force on the obstacle, we simulate a second phase where the granular material is moving continuously.

In the second phase we implement boundary walls up- and downstream of the granular material to push it continuously past the obstacle. In this configuration the fixed boundary velocity is only prescribed at the boundary walls (orange walls in Figure 3.1), while all particles are moving completely freely (particles with blue outline and fill). To avoid a situation where the upstream boundary influences the mobilized domain around the obstacle, we stop the simulation after Δt_2 when the boundary walls have travelled half the domain length D_x in the streamwise direction.

While the impact pressures shown in Figure 3.5 are calculated as the mean value of the continuous pressure on the obstacle during the second phase (Supplementary Material S.1), for the results in Figure 3.7 we consider the instantaneous impact pressure values in this phase. In Figures 3.8 and 3.9, we report the instantaneous impact pressure values of the last time step of the simulations, as we relate the pressure to the MD properties extracted at this last time step (section 3.2.5).

In chapter 2 we implemented a similar setup consisting only of the second simulation phase described above. There we showed that the presented numerical procedure is able to reproduce impact pressure of snow avalanches measured in full-scale field experiments.

3.2.2 Obstacle geometries

To study the influence of the obstacle geometry on the MD and the impact pressure, we implement prism shaped obstacles with rectangular, circular and triangular cross-sections, as shown in Figure 3.2. In all simulations the obstacles are fixed in place and are rigid, consequentially not deforming under the experienced forces. All of these prismatic obstacles have a height of 5.7 m, which prevents the granular mass from overflowing the obstacle. We consider obstacles with widths w of 0.24 m, 0.6 m, 1.0 m, 3.0 m and 6.0 m. We select these widths based on the dimensions of already existing obstacles measuring the impact pressure of avalanches in field experiments (Sovilla et al., 2008b), which are 0.24 m, 0.6 m and 1 m wide. In our setup the obstacle widths are limited by our current computational resources, which do not allow the simulation of larger domains needed to avoid boundary effects for obstacles $w > 6$ m.

For the rectangular cross-sections, two sides are normal and two sides are parallel to the flow direction. The sides normal to the flow are of varying width w, while the sides parallel to the flow are 1.6 m in all simulations. A comparison of two simulations with obstacle lengths of 0.1 m and 1.6 m in the streamwise direction shows that the pressure only deviates by 0.3 % between the two cases. Hence, we expect that using a length of 1.6 m for all rectangular obstacles does not affect the results considerably.

For the circular cross-sections the width w corresponds to the diameter. For the triangular cross-sections we define the angle of the wedge facing the flow as $\alpha = 60°$. Hence, the width w of the triangular obstacles is given by the length of the downstream side of the triangle.

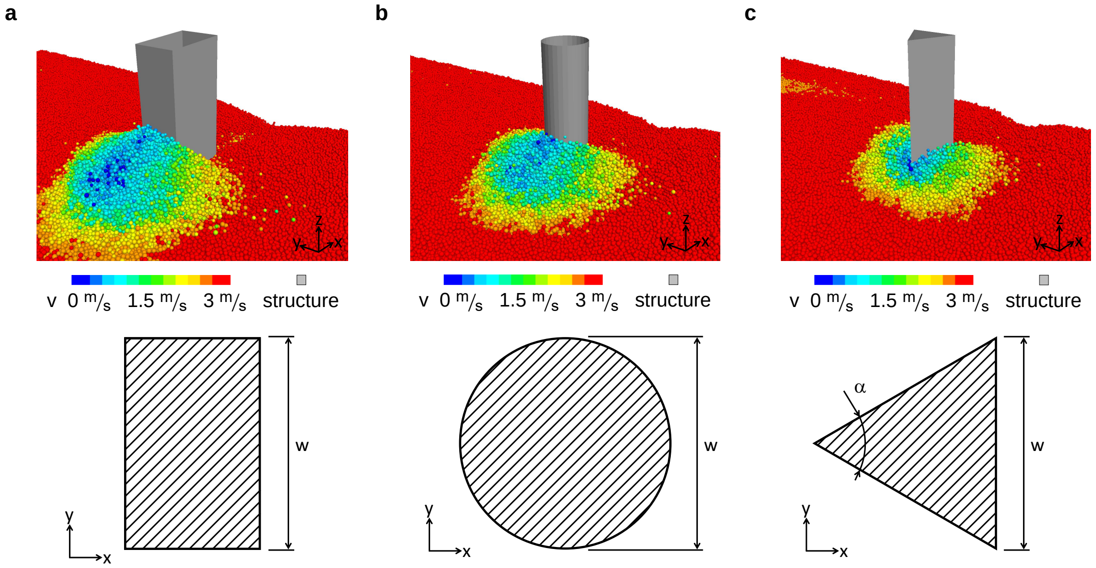

Figure 3.2 – Prismatic obstacles with a rectangular (a), circular (b) or triangular cross-sections (c). The top row shows obstacles with $w = 1$ m interacting with the granular flow. The bottom row shows the cross-sections with the most important geometric measurements.

The force exerted by the granular flow on the obstacle is calculated by summing the contact forces of all particles in contact with a surface. Because we simulate symmetrical obstacles and flow conditions, the force F_y in the y direction on the obstacles is $< 1\,\%$ of the total force in all simulations. The force F_z in the vertical direction is $< 5\,\%$ of the total force in all simulations. We therefore neglect F_y and F_z for the analysis of this study and only consider the force F_x exerted on the obstacle in the streamwise x direction.

To obtain a measure of the force exerted by the granular flow that is independent from the surface area and the geometry, we define the projected impact pressure p_x. It is equal to the impact force in flow direction F_x divided by the obstacle's area $A_{yz} = w\,h$ facing the flow projected on the $y-z$ plane normal to the flow direction $p_x = F_x / A_{yz}$.

3.2.3 Granular flow and material properties

The formulation of the Discrete Element Method and the model setup we use for this study are generic. If suitable particle and contact properties are chosen, the model can be used to simulate the interaction of any cohesive material and obstacle. However, in the context of snow avalanches, we choose suitable material properties for avalanche modeling. The most important contact and particle properties are summarized in Table 3.1. A more in-depth description of the parameter choices and the contact model can be found in chapter 2 and its supplementary material.

In our model all particles are subjected to a gravitational acceleration of $g = 9.81$ m/s^2 in the negative z direction. The mean diameter d_p of the particles is 0.08 m with a polydispersity of

20 % to avoid crystallization. The particles have a density of $\rho_p = 500$ kg/m^3 and a restitution coefficient of $e_r = 0.05$.

In DEM the material behavior is governed not only by the particle properties but also by the contact model, which is applied whenever particles interact. To simulate a cohesive granular material we use the *parallel-bond* model, originally developed for rock modeling (Potyondy and Cundall, 2004). This contact model has also proven to be suitable to simulate other cohesive geomaterials, such as sand (Butlanska et al., 2009), debris (Kang and Chan, 2018) and snow (Gaume et al., 2015b; Steinkogler et al., 2015; Bobillier et al., 2020).

The contact model consists of a linear and a cohesive component in parallel. The linear viscoelastic component consists of a spring and a dashpot in the normal direction and a spring and a coulomb friction limit in the tangential direction. The cohesive component is a bond connecting the particles in parallel to the linear component. The bond acts mechanically like a beam and can sustain tensile, bending, shear and torsional forces. In our simulations a new bond is formed whenever two unbonded particles make contact.

In order to assess the influence of cohesion in the pressure build-up processes, we perform simulations of a cohesive and a cohesionless scenario. In the cohesionless and the cohesive case we implement a cohesive strength of $\sigma_{coh} = 0.0$ kN/m^2 and $\sigma_{coh} = 10.0$ kN/m^2, respectively. This value corresponds to the tensile and pure shear strength of the cohesive bond.

Table 3.1 – Granular material properties (a) and simulation setup parameters (b)

Parameter	**Symbol**	**Unit**	**Value**
a) Particle and contact properties			
Particle density	ρ_p	kg/m^3	500
Particle diameter	d_p	m	0.08 ± 0.008
Young's modulus	E	Pa	10^5
Friction coefficient	μ	–	0.5
Restitution coefficient	e_r	–	0.05
Cohesive strength	σ_{coh}	N/m^2	$0.0, 10^4$
b) Simulation setup parameters			
Domain length	D_x	m	11, 22
Domain width	D_y	m	28
Domain height	D_z	m	28
Flow velocity	v	m/s	3
Flow height	h	m	2.5
Obstacle width	w	m	$0.24 - 6.0$

3.2.4 Compression tests of the granular material

One of this study's main objectives is to physically link the properties of the MD to the impact pressure on the obstacle. Hence, we need to bridge the gap between the relevant processes at the micro scale of the particles, such as the force chains and particle densification (Geng and Behringer, 2005; Favier et al., 2013), and the forces on the obstacle at the macroscopic scale in which we are interested. To achieve this, in this section we characterize the behavior of the granular material presented in the previous section under compressive loading by performing displacement-controlled axial compression tests.

We visualize the setup of the compression tests in Figure 3.3 a. For the compression test we use a material sample with a rectangular cross-section of equal side length of $s_0 = 6.0$ m, which corresponds to the maximum considered obstacle width w. A sensitivity analysis (Supplementary Material S.2) on the sample size shows that the compression tests' results converge towards the results obtained with $s_0 = 6.0$ m.

In the normal direction the granular material is compressed between a wall and a collection of rigidly connected particles, referred to as a *clump*. In the lateral directions the tested material sample is confined by periodic boundaries. We perform the compression tests in a zero gravity environment.

On the macroscopic scale the compressive strain $\epsilon_n = (l_0 - l)/l_0$ evokes a stress σ_n in the compression direction on the boundary wall, on the boundary clump and inside the granular material.

At the micro scale the rigid particles in contact typically interpenetrate each other due to compressive loading. The particle interpenetration δ visualized in Figure 3.3 b evokes a force at the contact according to the contact law. In the following we express the compression of the granular material at the micro scale as the particle interpenetration normalized by the particle radius $\Delta = \delta / r_p$.

Figure 3.3 c shows the normal stress σ_n inside the granular material, on the clump and on the wall as a function of the particle interpenetration in the cohesionless case. Figure 3.3 d shows a comparison of σ_n as a function of Δ in the cohesionless and the cohesive case. To distinguish between the test with the cohesive and cohesionless granular material, we use an asterisk for the quantities in the cohesive scenario, e.g. σ_n^*.

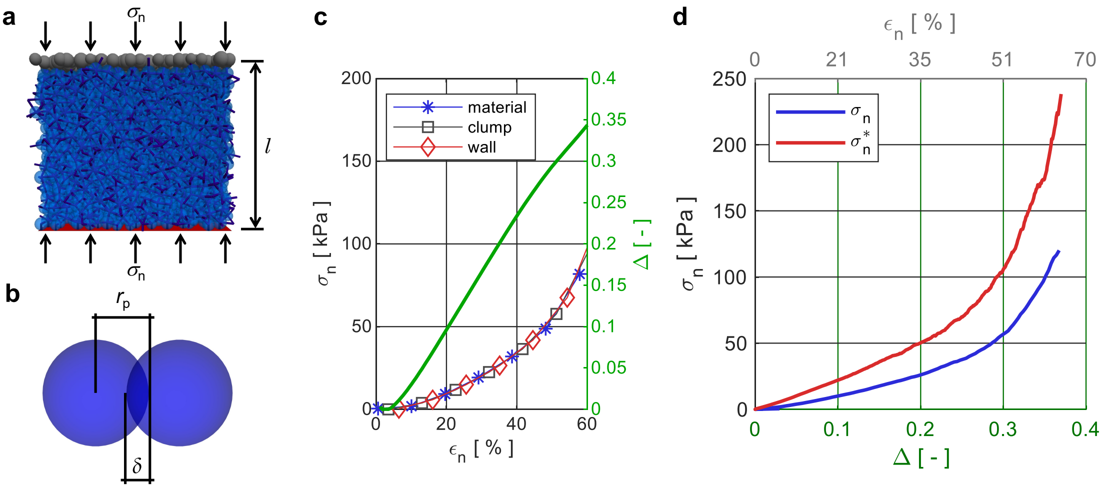

Figure 3.3 – Panel a shows the setup of the compression test, where the material (blue particles and contact network) is compressed between a wall (red) at the bottom and a clump (gray) at the top. For better visibility the particles are not to scale with the sample size. Panel b shows two spherical particles with radius r_p and interpenetration δ. Panel c shows a comparison between σ_n measured at the wall (red), at the clump (gray) and inside the granular material (blue), as well as the resulting Δ (green, right y-axis) in the cohesionless case as a function of the strain ϵ_n. Panel d shows the dependency between the normal stress σ_n in the granular material and the relative interpenetration Δ (bottom x-axis), as well as the macroscopic strain ϵ_n (top x-axis) for the cohesionless ($\sigma_{coh} = 0.0\ \mathrm{kN/m^2}$, blue) and the cohesive ($\sigma_{coh} = 10.0\ \mathrm{kN/m^2}$, red) case.

Panel c in Figure 3.3 shows that the normal stress inside the granular material increases monotonically with increasing compression of the granular material. The concave shape of the ϵ_n-σ_n curve indicates that the normal stress σ_n in the material increases at a higher rate than the interpenetration Δ for large compressive strains. The stresses inside the granular material, on the wall and on the clump are almost identical. Hence, in the following sections we always refer to the normal stress σ_n inside the granular material, which also acts on an obstacle wall in the case where there is one.

Panel d in Figure 3.3 reveals that the cohesive granular material transmits a ~ 1.5 times greater normal stress σ_n^* than the cohesionless material σ_n for the same interpenetration Δ. We use the results of these compression tests to relate the particle interpenetration Δ to the internal stress σ_n in the material. In the following sections we use the notation $\sigma_n(\Delta)$ when relating the two quantities on the basis of the graphs in Figure 3.3.

3.2.5 Definition of the mobilized domain

When a flow interacts with an obstacle we can generally distinguish between two domains. One, at a distance to the obstacle where the flow is not influenced, and another, in the vicinity of the obstacle where the flow is affected by the presence of the obstacle (Haefeli, 1948). For the latter we use the term *mobilized domain* (MD).

We systematically identify the MD by analyzing the normal contact forces F_n between the particles. Because the contacts between the particles are at random locations in the flow field, we discretize the flow domain with a regular grid to obtain a definition of the MD, which is consistent for all simulations. We use the average of the normal contact forces F_n located inside the grid cell as the representative value for the whole cell. A grid cell typically contains more than 15 contacts and is 0.1 m, 0.1 m and 0.3 m in size in the x, y and z direction, respectively. We choose the normal component of the contact force because the impact pressure on the obstacle physically originates from the force chains (Albert et al., 1999). Thus, we consider the normal component to be the most relevant for the transmission of the pressure to the obstacle. Indeed, the analysis can also be performed using the shear component, leading to similar results (Seguin et al., 2016). Finally, we obtain the threshold value by defining a fixed percentile value of the averaged normal contact forces F_n in the discretized grid. More in-depth details of how we define the threshold value are provided in Supplementary Material S.3.

Once the threshold value is obtained, we can define flow regions. The region where F_n is greater than the threshold is considered to be within the MD. Anywhere that F_n is lower is outside of the MD. Therefore, for very low percentile values the whole flow domain is considered the MD, while for very high percentile values the MD vanishes altogether. Hence, a physically relevant threshold value must be in between the extreme values.

For the present study we choose the 80th percentile of the normal contact forces as the threshold value. A sensitivity analysis is provided in Supplementary Material S.4 of this article. The analysis reveals that our results only weakly depend on the choice of the threshold in the range of the 70th to 90th percentile. Moreover, in Supplementary Material S.4 we visualize the change in MD for a sample simulation for the 70th, 80th and 90th percentile threshold values.

In Figure 3.4 we show a horizontal section through the flow visualizing the definition of the MD schematically (panel a) and for the example of a 3 m-wide rectangular obstacle (panel b). For our analysis we use four quantities of the MD: (1) the mean streamwise velocity v_{MD} inside the MD, (2) the volume V_{MD} of the MD, (3) the length L_{MD} of the MD extent in the streamwise direction, and (4) the averaged interpenetration Δ_{MD} of the particles inside the MD.

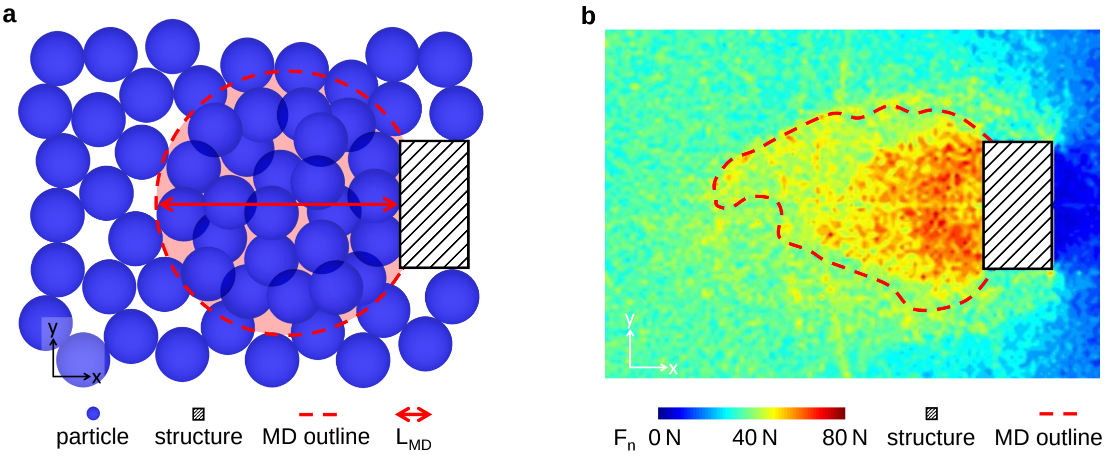

Figure 3.4 – Panel a shows a schematic representation of particles (blue) interacting with an obstacle (hatched black, not to scale) and the MD (red dashed outline and shading). The red arrow shows the length L_{MD} of the MD extent in the streamwise direction. Panel b shows the MD (red dashed outline) extracted from a simulation of an obstacle with a rectangular cross-section of $w = 3$ m. The coloring of the field scales with the normal contact force F_n, which we use to define the MD.

As mentioned in section 3.2.1, we only analyze MD properties at the last time step of the simulation. This is necessary because the vast number of particles and contacts in the system lead to large amounts of data, which cannot be stored for many time steps for all simulations. In Figures 3.8 and 3.9, where we link the impact pressure to the MD properties, we consistently report the impact pressure value of the last time step of the simulation.

3.3 Results

In the following section we first show how the impact pressure depends on the obstacle width and geometry, as well as on the cohesion of the granular material. In the same section we also compare the extent and the properties of the MD in cohesionless flows for different obstacle geometries. Thereafter, we show how cohesion affects the granular material in the MD and how this is linked to the change in impact pressure. Finally, we estimate the impact pressure exerted by the cohesionless flow on the obstacles based on the physical properties of the MD and compare the result with the simulated impact pressure.

3.3.1 Influence of the obstacle width and geometry on the impact pressure and the MD

As described in section 3.2.2, we study the pressure p_x contributing to the impact force in the flow direction. Figure 3.5 shows p_x as a function of the obstacle width w for the obstacles with a rectangular, circular or triangular cross-section. On the top x-axis we indicate the ratio of obstacle width w to particle diameter d_p. This ratio may be critical for the interaction processes when the size of the particle is of the same order as the width of the obstacle (Takada and Hayakawa, 2020; Kumar et al., 2017).

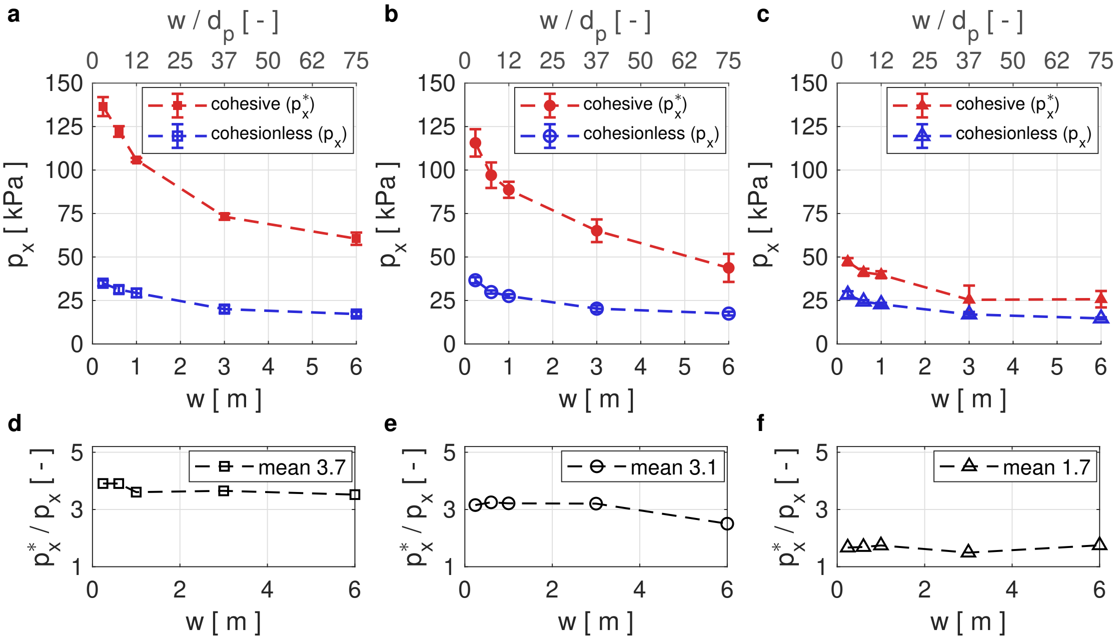

Figure 3.5 – Panels a, b and c show the impact pressure on obstacles of varying widths w with rectangular, circular and triangular cross-sections, respectively. The blue and red curves show the impact pressure exerted by a cohesionless and a cohesive flow, respectively. The top x-axis shows the width of the obstacle relative to the particle diameter w/d_p. The error bars indicate the standard deviation from the mean value of the pressure. Panels d, e and f show the impact pressure ratio of cohesive and cohesionless flows on obstacles of varying widths w with rectangular, circular and triangular cross-sections, respectively.

In Figure 3.5, we observe that the impact pressure p_x on all geometries decreases in a non-linear fashion for increasing obstacle width w. The impact pressure is highest on the obstacles with the rectangular and circular cross-sections, while it is significantly lower on the triangular obstacle. In the cohesionless cases the maximum pressure on the rectangular and cylindrical obstacles is ~ 1.3 times higher than the pressure on the triangular obstacle. The average impact pressure exerted by the $v = 3$ m/s and $h = 2.5$ m cohesionless flow on all considered obstacle geometries lies between 15 kPa and 37 kPa. In the cohesive case the pressures on the narrowest $w = 0.24$ m and the widest $w = 6$ m obstacle vary considerably: 61 – 137 kPa, 44 – 116 kPa and 26 – 47 kPa for the rectangular, circular and triangular cross-sections, respectively. Hence, as visualized in Figure 3.5 d–f for our cohesive scenario where $\sigma_{coh} = 10.0$ kN/m^2, the impact pressure is approximately 3.7, 3.1 and 1.7 times higher than in the cohesionless case for the rectangular, circular and triangular cross-sections, respectively. Similarly, the maximum pressure on the rectangular and cylindrical obstacles is ~ 2.5 times higher than the pressure on the triangular obstacle, which is higher than the pressure differences between the different geometries in the cohesionless case. It is important to note that these are approximate average values which vary for the different widths, as Figure 3.5 clearly shows.

In Figure 3.6 a–f we visualize the mobilized domains in the cohesionless case for all geometries by shadowing the region outside the MD with a semi-transparent overlay. The white area trailing the black and white hatched obstacle cross-section is a particle-free region caused by the detachment of the flow from the obstacle contour. The colored plots show the velocity field (upper half of plots) and the contact forces (lower half) in the vicinity of the obstacle in a horizontal section at mid-flow depth. Panels a–f therefore show that the MD has a distinct shape for all three geometries. The size of the MD scales approximately proportionately to the width of the obstacle. Moreover, in Figure 3.6 a–f we demonstrate that the extent of the zone influenced by the obstacle is mostly consistent between the contact forces and the velocity field.

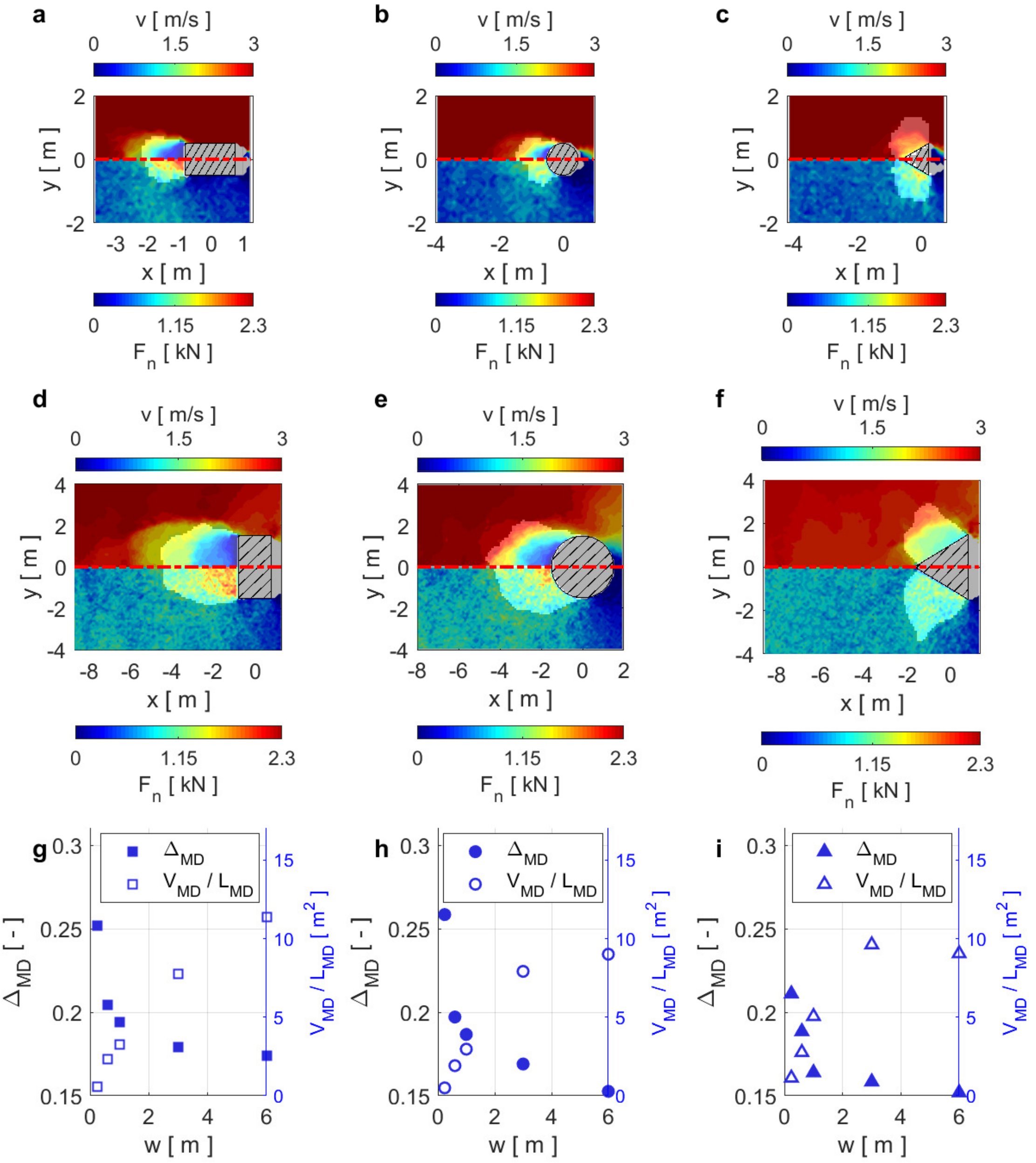

Figure 3.6 – Analysis of the velocity field, the contact forces and the MD in cohesionless flows around the obstacle. The left, middle and right columns show the results for the rectangular, circular and triangular cross-sections (hatched areas), respectively. Panels a–c and d–f show obstacles with width $w = 1$ m and $w = 3$ m, respectively. Panels a–f show the velocity field in the upper half and the contact forces in the lower half. The region outside the MD is shadowed with a semi-transparent overlay. Panels g–i show the physical properties Δ_{MD} (filled symbols, left y-axis) and V_{MD}/L_{MD} (open symbols, right y-axis) of the MD for different obstacle widths w.

In the panels g–i of Figure 3.6, we show how the physical parameters Δ_{MD} and V_{MD}/L_{MD} of the MD depend on the obstacle width w. We use these quantities in section 3.3.3 to estimate the impact pressure on the obstacle in the cohesionless case.

Figure 3.6 g–i shows that the average particle interpenetration Δ_{MD} inside the MD decreases with increasing obstacle width w, similarly to the impact pressure in Figure 3.5. Because Δ_{MD} reflects the interpenetration of the particles at the micro scale, we use it as an indicator of the compression of the material inside the MD. Δ_{MD} ranges from 0.15 to 0.26 for the rectangular and cylindrical obstacles and from 0.15 to 0.21 for the triangular obstacle. Hence, similar to p_x, Δ_{MD} is mostly highest for the rectangular obstacles, followed by the cylindrical obstacles, and is lowest for the triangular obstacles.

The volume-to-length ratio V_{MD}/L_{MD} is a measure of the size of the MD and how far upstream the MD extends from the obstacle. V_{MD}/L_{MD} increases almost linearly with obstacle width and levels off slightly for the obstacles with $w \geq 3$ m. For the 6 m-wide cylindrical and triangular obstacles V_{MD}/L_{MD} is considerably lower than the linear trend. The deviation from the linear trend may be a consequence of the MD occupying a large portion of the simulation domain for the widest obstacles with $w = 6$ m.

To assess whether the relationship between the MD properties and p_x observed in Figure 3.6 g–i for the last simulation time step also holds on a temporal scale, in Figure 3.7 we compare the temporal evolution of V_{MD}/L_{MD} and Δ_{MD} with p_x. Figure 3.7 shows the data for the examples of obstacles with $w = 1$ m impacted by cohesionless flows. For these plots we select the same time window as used to average the impact pressure for the data shown in Figure 3.5.

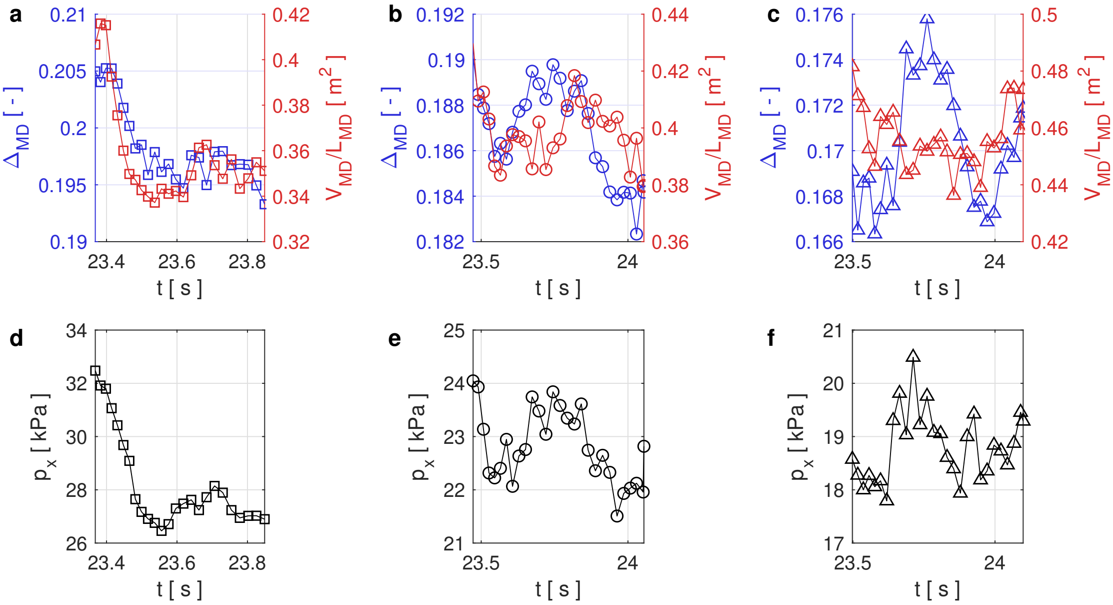

Figure 3.7 – Comparison between time series of V_{MD}/L_{MD}, Δ_{MD} (panels a–c) and p_x (panels d–f). The first, second and third columns show the data for the obstacles with rectangular, circular and triangular cross-sections, respectively.

While all quantities visualized in Figure 3.7 exhibit temporal fluctuations, we can identify a striking similarity between the qualitative temporal evolution of Δ_{MD} (blue curves) in the upper plots and the black curves for p_x in the lower plots. V_{MD}/L_{MD}, which we interpret as a measure of the spatial extent of the MD, also shows mostly good agreement with p_x, except in Figure 3.7 c and f. There the qualitative behavior of Δ_{MD} and V_{MD}/L_{MD} are almost inverted, indicating—in agreement with Figure 3.6 g–i—that V_{MD}/L_{MD} probably plays a subordinate role in the impact pressure compared with Δ_{MD}.

3.3.2 Influence of cohesion on the impact pressure and the MD

In this section we investigate the difference between the MD in the cohesionless ($\sigma_{coh} = 0.0\,\mathrm{kN/m^2}$) and the cohesive ($\sigma_{coh} = 10.0\,\mathrm{kN/m^2}$) case in order to understand the pressure difference observed between the two cases. In order to investigate the origin of the impact pressure increase due to cohesion, here we consider Δ_{MD} to reflect the material compression inside the MD.

Figure 3.8 a–c shows that the relative interpenetrations Δ_{MD} in the cohesive case decrease for obstacles of increasing width, similarly to the cohesionless case already shown in Figure 3.6 g–i. The difference in Δ_{MD} between the cohesionless and the cohesive case is ~ 4 times larger for the rectangular and cylindrical obstacles than for the triangular obstacles and is larger for narrow obstacles $w \leq 1$ m than for wider obstacles.

In order to estimate how much more stress is transmitted by the cohesive granular material compared with the cohesionless flow, we convert the interpenetration in the MD to normal stresses $\sigma_n^*(\Delta_{MD}^*)$ and $\sigma_n(\Delta_{MD})$ based on the results of the compression tests in Figure 3.3 d. The panels d–f in Figure 3.8 show the ratio of the normal stresses $\sigma_n^*(\Delta_{MD}^*)/\sigma_n(\Delta_{MD})$. This ratio reflects the stress level inside the MD in the cohesive material relative to the cohesionless case. While $\sigma_n^*(\Delta_{MD}^*)/\sigma_n(\Delta_{MD})$ shows a decreasing tendency for obstacles of increasing width, the mean values are 3.5, 3.2 and 2.1 for the rectangular, circular and triangular geometries, respectively.

To test how the relative change in the normal stress in the MD between the cohesionless and the cohesive case is related to the difference in impact pressure, we multiply the pressure of the cohesionless case p_x by the normal stress ratio $\sigma_n^*(\Delta_{MD}^*)/\sigma_n(\Delta_{MD})$. Hence, we calculate the estimated impact pressure $p_{x,calc}^*$ of the cohesive scenario according to equation (3.1).

$$p_{x,calc}^* = p_x \sigma_n^*(\Delta_{MD}^*)/\sigma_n(\Delta_{MD}) \tag{3.1}$$

Figure 3.8 g–i shows the estimated impact pressures $p_{x,calc}^*$ for all obstacle geometries. From these panels we observe that the stress ratios $\sigma_n^*(\Delta_{MD}^*)/\sigma_n(\Delta_{MD})$ agree well with the impact pressure increase due to cohesion.

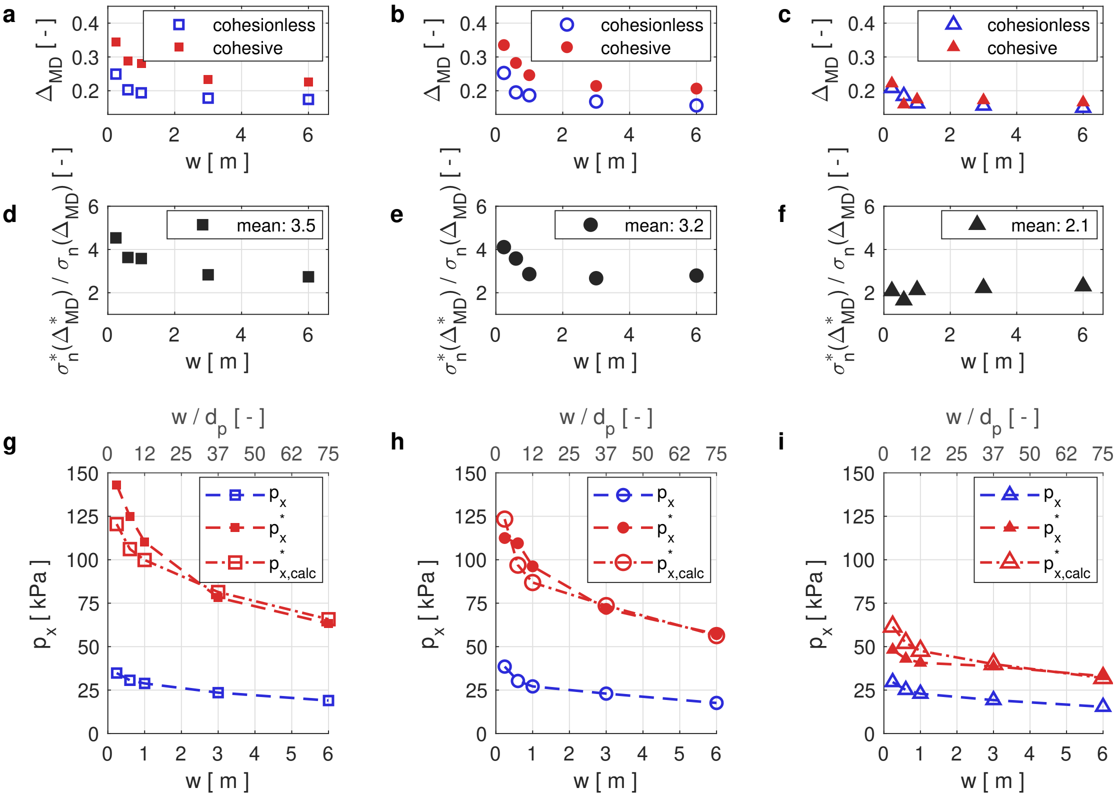

Figure 3.8 – Influence of cohesion on the contact network inside the MD. The open blue symbols and red filled symbols represent data from the cohesionless and cohesive cases, respectively. Data for the obstacles with rectangular, circular and triangular cross-sections are shown in the left, middle and right columns, respectively. All panels show how the respective quantities vary with the obstacle width w. Panels a–c show the relative particle interpenetrations Δ. Panels d–f show the ratio of the normal stresses in the cohesive and cohesionless case $\sigma_n^*(\Delta_{MD}^*)/\sigma_n(\Delta_{MD})$. Panels g–i show a comparison between the simulated impact pressure exerted by the cohesive flow and the pressure estimation calculated from the impact pressure in the cohesionless case multiplied by the normal stress ratio $p_{x,calc}^* = p_x \sigma_n^*(\Delta_{MD}^*)/\sigma_n(\Delta_{MD})$ (open red symbols).

3.3.3 Analytical model to quantitatively link the MD properties to the impact pressure

In this section we derive an expression from basic physical concepts to estimate the impact pressure exerted by cohesionless flows. For this calculation we use properties of the MD from the simulations to investigate the relevance of the MD for the resulting impact pressure on the obstacle. Hence, the pressure calculation is not predictive but should highlight the physical link between the properties of the MD and the impact pressure.

Similarly to in other studies (Faug, 2015; Sovilla et al., 2016), we divide the impact force into an inertial $F_{x,i}$ and a gravitational $F_{x,g}$ contribution. Hence, the calculated pressure p_x is the sum of the two contributions divided by the frontal area A_{yz}:

$$p_{x,calc} = (F_{x,i} + F_{x,g})/A_{yz} = p_{x,i} + p_{x,g} \tag{3.2}$$

The individual contributions are calculated as follows:

1. Inertial contribution:

   $$F_{x,i} = \frac{1}{2}(v^2 - v_{MD}^2)\frac{m_{MD}}{L_{MD}} = \frac{\rho}{2}(v^2 - v_{MD}^2)\frac{V_{MD}}{L_{MD}} \tag{3.3}$$

   We calculate the inertial contribution based on the change in kinetic energy of the granular mass $m_{MD} = \rho V_{MD}$, initially travelling at the free flow velocity v, which is decelerated to the mean velocity of the particles in the MD v_{MD} within the streamwise extent L_{MD} of the MD, due to the obstacle's resistance to the flow.

2. Gravitational contribution:

   $$F_{x,g} = \zeta\frac{1}{2}\rho g h^2 w \tag{3.4}$$

   The gravitational contribution is calculated as a hydrostatic-like force increasing with the flow depth squared (Albert et al., 1999). The factor $\zeta = \sigma_n(\Delta_{MD})/\sigma_z$ reflects the stress concentration inside the MD due to the densification of the contact network $\sigma_n(\Delta_{MD})$ with respect to the hydrostatic stress $\sigma_z = \rho g h$.

Figure 3.9 a–c shows a comparison of the impact pressures calculated with equations (3.3) to (3.4) and the simulated pressures in the cohesionless scenario for all obstacle geometries and widths. The shaded areas represent the calculated contributions $p_{x,g}$ (dark shade of blue) and $p_{x,i}$ (light shade of blue), respectively. The calculated pressure is the sum of the gravitational and the inertial contribution and is shown by the filled blue symbols.

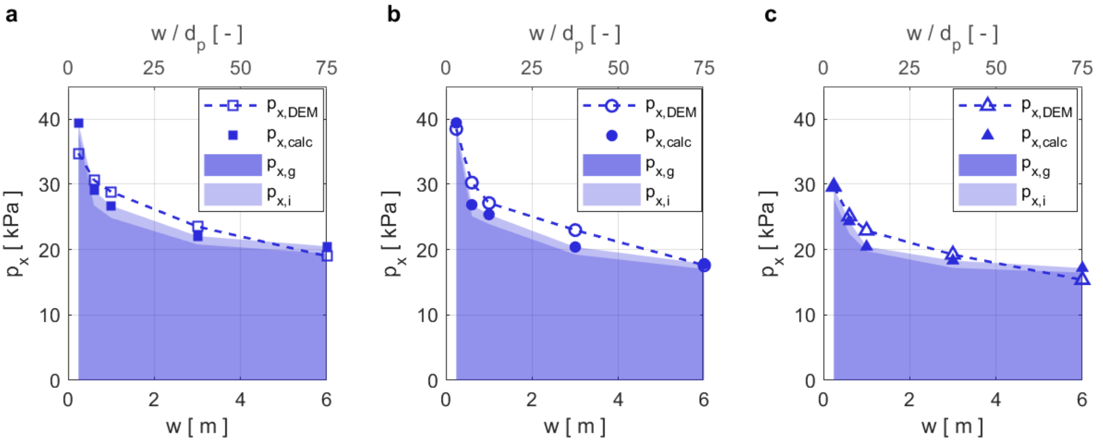

Figure 3.9 – The blue symbols in panels a, b and c show the comparison of the calculated impact pressure according to equations (3.2) to (3.4) with the simulated impact pressure of a cohesionless flow on obstacles of varying widths w with a rectangular, circular and triangular cross-sections, respectively. The top x-axis shows the width of the obstacle relative to the particle diameter w/d_p. The dark and light blue shaded areas represent the calculated gravitational and inertial contributions, respectively.

The calculated impact pressure $p_{x,calc}$ shown in Figure 3.9 decreases non-linearly for obstacles of increasing width. Hence, it agrees well with the qualitative trend of the simulated impact pressure $p_{x,DEM}$. For all cross-sections the calculation overestimates the simulated impact pressure for the narrowest ($w = 0.24$ m) and widest obstacles ($w = 6$ m). The impact pressure on the obstacles of intermediate width (0.6 m$\leq w \leq$ 3 m) is slightly underestimated. For the rectangular and the cylindrical obstacles $p_{x,calc}$ is lower than $p_{x,DEM}$ for the narrow obstacles ($w \leq 1$ m), while it is larger for the wide obstacles ($w \geq 3$ m). The average relative error between the calculated and the simulated impact pressure is 7 % for all cross-sections.

For all calculations $p_{x,g}$ contributes 95 % and $p_{x,i}$ 5 % to the total impact pressure $p_{x,calc}$. This highlights that, for the present case where $Fr = 0.61$, both contributions are present and the gravitational contribution is considerably larger than the inertial contribution. While $p_{x,i}$ is almost constant for all widths and geometries, $p_{x,g}$ varies similarly to the simulated impact pressure $p_{x,DEM}$.

3.4 Discussion

3.4.1 Physical processes governing the flow–obstacle interaction and impact pressure for varying obstacle geometries

The simulated impact pressure shown in section 3.3.1 is in agreement with previous research showing that the pressure on obstacles offering high resistance to the flow is higher than for pointed obstacles (Favier et al., 2009b; Albert et al., 2001). In chapter 2, we performed a study on the avalanche pressure on a particular geometry of an existing instrumented steel pylon (Sovilla et al., 2010), and we concluded that the size of the MD and the resulting impact pressure build-up depends on the obstacle geometry. The evident variation in MD size in Figure 3.6 and the impact pressure in Figure 3.5 for the differing obstacle geometries and widths confirms this dependency. The linearly increasing trend of the MD size parameter V_{MD}/L_{MD} for obstacles with increasing width for $w < 6$ m is consistent with the result in Figure 8 a in Faug (2015). Faug reports that a linear increase of the MD's typical length scale is a robust feature appearing in a number of experimental and numerical studies on the impact of granular flows on obstacles.

Interestingly, we find that the average pressure p_x on the obstacle decreases non-linearly for obstacles of increasing width w. This phenomenon is known to occur with creeping snow and granular snow avalanches (Haefeli, 1948; Margreth, 2007). Studies on the relative motion of intruders in dense granular materials at low Fr often report the drag force on the intruder. In these cases the drag force increases with the size of the intruder (Hilton and Tordesillas, 2013; Kumar et al., 2017; Panaitescu et al., 2017). However, if the data from these studies is analyzed with respect to the pressure rather than the force, the trend of decreasing impact pressure for increasing intruder size is confirmed (Supplementary Material S.5).

A tentative explanation for the decreasing pressure on obstacles of increasing width can be given for the obstacles with rectangular cross-sections. Figure 3.4 b demonstrates shows that an arch of strong contact forces forms upstream of the edge facing the flow, especially for wide obstacles $w \gtrsim 1$ m with rectangular cross-sections. Hence, the middle part of the obstacle is largely sheltered from the impact of the incoming flow by the arch. However, this fails to explain the decrease in impact pressure on the circular and triangular cross-sections of increasing width, because the formation of the arch is not evident, e.g. in Figure 3.6 e–f.

More comprehensively, for varying obstacle widths of all cross-sections, the particle interpenetrations in MD (Figure 3.6 g–i) and the impact pressure (Figure 3.5) qualitatively show a high degree of similarity. This suggests that the impact pressure is governed by the compression state of the granular material inside the MD. In the MD of the narrow obstacles the particles are jammed closer together than in the MD of the wider obstacles. From the compression test in Figure 3.3 d we learn that increasing Δ_{MD} leads to an increased stress level in the granular material, resulting in a higher pressure on the obstacle. In the absence of rigorous evidence, we speculate that Δ_{MD} is lower for wide obstacles because of the higher shearing of the material, which is necessary for the particles to travel around the obstacle. This causes higher shear dilation and leads to a looser packing of the particles in the MD of wide obstacles. This is consistent with the finding of Seguin et al. (2016), who show that although the material inside the MD is almost stagnant, zones of high shear and dilation are located in the vicinity of the upstream boundary of the obstacle.

As shown in Figure 3.6 g–i, we identify the varying degrees of material compression in the MD Δ_{MD} as the predominant origin of the differing impact pressure on the three geometries. Obstacles offering high resistance to the flow, such as the rectangular and circular cross-section in Figure 3.6 g and h, cause the granular material to jam upstream, which leads to high Δ_{MD}. Pointed obstacles, such as the triangular cross-section in Figure 3.6 i, tend to deflect the flowing material without causing particle jamming. This leads to lower Δ_{MD} and consequentially to lower impact pressure.

Hence, in our results we can consistently correlate Δ_{MD} to the impact pressure on obstacles of varying geometry and width. This provides further evidence supporting the assumption of Chehata et al. (2003) that the “granular drag must result from the compressive stresses acting on the upstream stagnation region”.

As shown in Figures 3.6, 3.8 and 3.9, we are able to show that the instantaneous impact pressure and MD properties correlate for various obstacle geometries, for cohesive and cohesionless flows. Figure 3.7 confirms that the impact pressure and MD properties correlate on a temporal scale as well. Hence, as the flow characteristics of real avalanches and other gravity-driven granular flows evolve over time, we are confident that the link between the instantaneous MD properties and impact pressure is still valid for subcritical granular dense flows interacting with obstacles. When considering applications to structural engineering, note that real-world scenarios may deviate substantially from the steady subcritical granular dense flow considered here. Among other things initial impact or large material accumulations upstream of the obstacles may critically damage the obstacle.

3.4.2 Influence of cohesion on the flow–obstacle interaction processes

The results displayed in Figure 3.5 confirm previous research that a cohesive flowing granular material exerts significantly more pressure than the same material without cohesion (Favier et al. (2013) and chapter 2). Indeed, in a previous study we found a scaling (see Supplementary Material S.6) for the pressure increase due to cohesion, relating the impact pressure increase to the ratio of Fr and the Bond number Bo, where Bo is the cohesive strength σ_{coh} normalized by the vertical stress inside the granular material (chapter 2). When evaluating the scaling for the Froude and Bond numbers in the present study, we calculate a pressure increase factor of ~ 2.3. Considering that the impact pressure increase due to cohesion may vary as a result of differing obstacle geometries, this is in the range of impact pressure increase factors of 1.7–3.7, as observed in Figure 3.5.

In Figure 3.8 a–c, we observe that in the cohesive case the particle interpenetration Δ_{MD} in the MD is larger than in the cohesionless case. We assume that a higher Δ_{MD} arises because the cohesive granular material sustains more loading from the upstream flow before rearrangements of the force chains within the granular material allow the particles to flow around the obstacle. On the particle scale the force chain rearrangement is inhibited by the cohesive bonds connecting the particles. Similarly to the increase in impact pressure (Figure 3.5) due to cohesion, we also observe a greater increase in particle interpenetration Δ_{MD} for the rectangular and cylindrical obstacles than for the triangular obstacle.

Using Δ_{MD} and the compression tests (Figure 3.3 d), we calculate the ratio of the stress inside the granular material in the cohesive and cohesionless cases (Figure 3.8 d–f). Based on the analysis of the cohesionless flows (section 3.4.1), we suspect that the pressure increase due to cohesion also originates from the jammed material state inside the MD. Hence, multiplying this ratio by the impact pressure of the cohesionless scenario according to equation (3.1) gives us an estimate of the impact pressure increase due to cohesion. A comparison between the simulated impact pressure p_x^* and $p_{x,calc}^*$ in Figure 3.8 g–i shows that the factor $\sigma_n^*(\Delta_{MD}^*)/\sigma_n(\Delta_{MD})$ mostly reproduces the pressure increase due to cohesion for most of the obstacles of differing widths and geometries. The small deviations between the simulated and the estimated cohesive impact pressure may be caused by secondary processes which do not scale proportionally with the width of the obstacle, such as the arch formation for the rectangular obstacles mentioned in section 3.4.

Nevertheless, the good agreement between p_x^* and $p_{x,calc}^*$ indicates that the pressure increase is a direct consequence of the enhanced stress transmission between cohesive particles compared with cohesionless particles.

The fact that $\sigma_n^*(\Delta_{MD}^*)/\sigma_n(\Delta_{MD})$ varies for the different geometries highlights that the pressure increase due to cohesion depends not only on cohesion itself, but also on the obstacle geometry. We conclude that, the force transmission through the cohesive force chains is more efficient if the cohesion increases and, similar to the cohesionless case, if the flow impacts the obstacle surface at a right angle.

3.4.3 Analytical model to quantitatively link the MD properties to the impact pressure

In order to establish a quantitative link between the MD and the impact pressure, we estimate the pressure based on the MD properties using an analytical model. Because estimating the MD properties is no less complex than determining the impact pressure itself, the model is descriptive rather than predictive. We model the impact pressure in the cohesionless case as the sum of an inertial and a gravitational contribution, as suggested by previous studies (Faug, 2015; Sovilla et al., 2016). The results of section 3.3.3 show that the pressure estimated with the two contributions (equations (3.2) to (3.4)) mostly reproduces the simulated impact pressure of the cohesionless scenario. The average relative error of the calculated pressure is 7 % compared with the simulated pressure $p_{x,DEM}$. Hence, the qualitative agreement of the calculated and the simulated impact pressure highlights again that the geometrical properties of the MD and the physical material properties within the domain govern the pressure on the obstacle. Furthermore, the agreement also indicates that a model considering an inertial $F_{x,i}$ and a gravitational $F_{x,g}$ contribution is able to capture the main physical processes involved in the flow–obstacle interaction.

In literature the inertial contribution $F_{x,i}$ of the drag force is often calculated using the empirical drag coefficient C_D. Previous studies suggest that C_D can be divided into a flow regime and a part that is dependent on structure geometry (Favier et al., 2009b; Wassgren et al., 2003; Thibert et al., 2008). In equation (3.3) it is the material's deceleration $v^2 - v_{MD}^2$ that accounts for the influence of geometry. For example, due to its shape with the wedge facing the flow, the flowing material is more deflected than decelerated in the case of the triangular obstacle compared with e.g. the rectangular cross-sections. This leads to a smaller velocity difference $v^2 - v_{MD}^2$ for the triangular cross-section. This trend is analogous to the C_D values usually reported in the literature, which are higher for the rectangular cross-section than for the triangular cross-section (Favier et al., 2009a; Sauermoser et al., 2012).

The ratio of the MD volume and length, V_{MD}/L_{MD}, has the dimensions of an area and accounts for the size and the shape of the MD. In chapter 2 we show that the shape and size of the MD is mainly controlled by Fr. Hence, we interpret the factor V_{MD}/L_{MD} as the part of the drag coefficient that is dependent on the flow regime.

For the gravitational $F_{x,g}$ contribution, in their seminal article Albert et al. (1999) introduce a proportionality factor that accounts for the particle properties. In equation (3.4) we define an analogous factor ζ. In our formulation, however, the factor is defined as the ratio of the normal contact stresses derived from the particle interpenetration $\sigma_n(\Delta_{MD})$ and the theoretical hydrostatic stress σ_z. ζ therefore considers the compressive behavior of the material inside the MD, which governs the impact pressure due to build-up of the MD.

In our flow scenario with $Fr = 0.61$, we find that the calculated pressure is composed of 95 % gravitational and 5 % inertial contributions. This agrees with the observation of Faug (2015) that for a wide range of Froude numbers, $0.1 \lesssim Fr \lesssim 10$, both the inertial and the gravitational contribution of the impact pressure are present. At low velocities the dominance of the gravitational pressure contribution is probably responsible for the fact that the pressure is often observed to be independent of the velocity in this range of low Fr (Wieghardt, 1975; Albert et al., 1999). The inertial contribution increases quadratically with increasing speed and consequentially outweighs the gravitational contribution only at higher velocities. When Fr becomes supercritical, the MD changes substantially from the rounded shapes in Figure 3.6 to a bow shock (chapter 2, Hauksson et al. (2007) and Cui and Gray (2013)). Hence, it is not clear whether the interaction processes and the analytical model presented in this study still hold in the supercritical regime. Similar to in real experiments, the impact pressure contributions in DEM simulations cannot be identified individually. Simulations with higher flow velocities, where the inertial contribution is dominant, could help to determine whether the inertial contribution is adequately formulated in our model.

Figure 3.9 shows that the calculated impact pressure $p_{x,calc}$ overestimates the simulated impact pressure of the obstacles with $w = 0.24$ m and $w = 6$ m, while the pressure on the obstacles of intermediate width $0.6\ \text{m} \leq w \leq 3$ m is underestimated. This difference probably arises because of the varying proportion between the size of the whole simulation domain and the area occupied by the obstacle. Although we only consider a fraction of the domain for the MD threshold calculation, to keep the ratio between the considered domain size and varying obstacle sizes constant (Supplementary Material S.3), the error persists. The error could probably be reduced more efficiently by increasing the size of the simulation domain, which is currently not possible with the computational resources available.

3.4.4 Limitations

Although we are able to find good agreement between the simulated and the estimated pressure using the MD properties, we identify two main limitations of the present analysis.

First, as described in section 3.2.5, we use a percentile threshold of the normal contact forces to identify the MD, which is the basis for our results. We perform a sensitivity analysis (Supplementary Material S.4) and show that our results do not crucially depend on the threshold value within the range of the 70th to 90th percentile. Nevertheless, the deviations between the simulated and calculated impact pressure, as well as the deviation from the linear trend of V_{MD}/L_{MD} for $w = 6$ m in Figure 3.6 g–i show the limitations of our approach, as the MD identification is delicate. Hence, in the future it would be preferable to establish a threshold based on the physical properties of the material surrounding the MD to distinguish the MD from the rest of the flow domain. In order to achieve this, various variables can be considered potential candidates for identifying the MD or may be linked to the impact pressure, such as shear force, shear rate, bulk density, coordination number, velocity (Chehata et al., 2003; Favier et al., 2009b), and stress anisotropy (Chung et al., 2019). After testing a number of variables, we conclude that, among these variables, Δ allows us to make the most comprehensive analysis. Second, the computational resources needed for the DEM simulations presented here are considerable. While we aim to minimize the computational time, we also want to ensure that our results are not affected by domain boundary influences. This results in large computational domains, while the simulated physical interaction times are only a few seconds. The simulations show that the MD of wide obstacles in cohesive flows takes longer to establish compared with the MD of narrow obstacles in cohesionless flows. Hence, in the case of narrow obstacles with $w \leq 1$ m, we are confident that a steady state impact force is reached within our simulations. For the interaction of wide obstacles and cohesive flows, even longer simulations are needed to confirm that the pressure does not change significantly anymore. Therefore, the pressure difference between the narrow and wide obstacles may be slightly overestimated here. However, the trend of decreasing average impact pressure on obstacles of increasing width has also been found in other studies (Supplementary Material S.5) and is therefore not an artefact of our numerical procedure. Moreover, in section 3.3.3 we estimate the impact pressure based on the instantaneous MD properties and compare it to the impact pressure at the same time step. Hence, even in cases where a steady state is not reached, this highlights once more how crucially the impact pressure is linked to the instantaneous physical properties of the MD.

3.5 Conclusions

In this study, we demonstrate that the non-linear decrease in the impact pressure on obstacles of increasing width is linked to the compression of the granular material in the MD, as the particle interpenetration Δ_{MD} decreases in a similar fashion for increasing w. Furthermore, we show that the stress ratio of the cohesive to the cohesionless case $\sigma_n^*(\Delta_{MD})/\sigma_n(\Delta_{MD})$ agrees well with the increase in the average impact pressure due to cohesion for different obstacle geometries. Hence, we identify two main mechanisms causing the pressure increase due to cohesion. First, the particle interpenetration Δ_{MD} and thus the material compression in the MD is higher than in the cohesionless case, probably because the cohesive bonds inhibit the rearrangement of force chains and thus the particle flow around the obstacle. Second, the force transmission between the particles is higher than in the cohesionless case because the particles are connected more rigidly through the cohesive bond (Figure 3.3). The analysis also shows that further processes might be present but play a subordinate role to the two processes mentioned above.

Finally, we estimate the impact pressure in the cohesionless case based on the MD properties and considering an inertial and a gravitational contribution. The agreement of the calculated and the simulated impact pressure values provides a further indication that the MD fundamentally governs the pressure on the obstacle (Chehata et al., 2003; Faug, 2015).

By calculating the pressure of a cohesionless and cohesive granular flow impacting an obstacle using the physical properties of the MD, we show that the impact pressure exerted by a subcritical flow on an obstacle is quantitatively linked to the physical properties of the MD. The calculations highlight that the jamming and compression of the material inside the MD govern the pressure build-up on the obstacle.

We identify limitations of our model linked to the computational cost of the simulations and the MD identification. Nonetheless, in the future the presented method could help to estimate impact pressures on obstacles based on the jamming of the granular material predicted for specific geometries and using compression tests.

Acknowledgements

Michael Kyburz, Betty Sovilla and Christophe Ancey acknowledge the Swiss National Science Foundation for funding this project “Pressure on obstacles induced by granular snow avalanches” (grant no. 200021_169640). Johan Gaume acknowledges financial support from the Swiss National Science Foundation (grant no. PCEFP2_181227). The Supplementary Material and the code to be used with the Itasca PFC3D software to reproduce the data presented in this paper are available in the open access data repository Zenodo, which is financed by the Horizon 2020 project OpenAIRE and hosted by CERN. The associated entry can be accessed via Kyburz M., Sovilla, B., Gaume J., & Ancey C. (2020). The concept of the mobilized domain: how it can explain and predict the forces exerted by a cohesive granular avalanche on an obstacle [Supplementary Material]. Zenodo. https://doi.org/10.5281/zenodo.4079357.

We kindly acknowledge the efforts made by the editor François Nicot and four anonymous reviewers for their interesting comments and the fruitful discussions, which helped to improve the manuscript. We appreciate the quick and diligent language editing by Melissa Dawes.

4 Physics-based estimates of drag coefficients for the impact pressure calculation of dense snow avalanches

Authors

M. L. Kyburz[1,2], B. Sovilla[1], J. Gaume[1,3], C. Ancey[3]

[1] WSL Institute for Snow and Avalanche Research SLF, Davos, Switzerland
[2] Environmental Hydraulics Laboratory, École Polytechnique Fédérale de Lausanne, Lausanne, Switzerland
[3] Snow and Avalanche Simulation Laboratory SLAB, École Polytechnique Fédérale de Lausanne, Lausanne, Switzerland

Publication

This chapter is a modified version of the publication:
Kyburz M.L., Sovilla B., Gaume J., Ancey C.: Physics-based estimates of drag coefficients for the impact pressure calculation of dense snow avalanches. Engineering Structures (2021)

Authors' contributions

Michael L. Kyburz: Conceptualization, Methodology, Software, Formal Analysis, Investigation, Visualization, Writing - Original Draft; **Betty Sovilla:** Funding Acquisition, Conceptualization, Experimental Data Curation & Investigation, Writing - Review & Editing, Supervision; **Johan Gaume:** Methodology, Writing - Review & Editing; **Christophe Ancey:** Writing - Review & Editing, Supervision.

4.1 Chapter summary

In this chapter we aim to make a step towards physics-based and practice-oriented computation of impact avalanche forces. In order to achieve this, we reuse the DEM setup described in the previous chapter 3 to simulate the interaction of avalanches and obstacles. We extract pressure and velocity measurements from the Vallée de la Sionne database to test the DEM code, calibrate the model parameters, and elaborate avalanche scenarios. The four selected avalanche scenarios are related to distinct flow regimes of the avalanche's dense core. Within the range of tested values, we find good agreement between simulated impact pressure and field data. Building on earlier research, we generalize an empirical equation for computing the impact pressure as a function of snow cohesion, velocity, flow regime, and structure shape and size. By defining and calibrating various coefficients from our DEM data and based on physical considerations, we propose a physics-based practical method for estimating the drag coefficient C_D depending on flow regime and obstacle geometry. We test the calculation method using data from three obstacles with different geometries from Vallée de la Sionne and find that the impact pressure profiles calculated based on the C_D estimates agree well with the full-scale measurement data.

4.2 Simulation of avalanche impact pressure on obstacles with DEM

4.2.1 Avalanche modeling setup and parameters

Flow avalanches have often been considered to behave like dry granular flows (Scheiwiller and Hutter, 1982; Salm and Gubler, 1985; Hutter, 1996), and this analogy has thus been used to model them on the laboratory scale or numerically. In this study, we applied the Discrete Element Method (DEM) to simulate avalanches moving past rigid obstacles using the PFC software from Itasca (Minneapolis, MN, USA). This software is based on the soft-contact algorithm (Cundall and Strack, 1979; Potyondy and Cundall, 2004) to model the interaction between cohesive particles. In this numerical framework, no fluid–solid coupling is considered, and thus the bulk dynamics is entirely ruled by particle contact. This means that in our study we simulated only the avalanche's dense flow part, assuming that the interaction between the solid phase and the interstitial air is negligibly small.

To simulate how avalanches interact with fixed obstacles, we used the numerical setup implemented in chapter 3. This setup extended the procedure in chapter 2 and made it possible to study obstacles wider than 0.6 m, which corresponds to the Vallée de la Sionne's pylon considered initially (section 4.2.2). In chapter 2 we showed that our numerical code could reproduce impact pressure measurements on the pylon.

In order to minimize the computational cost of simulations, we considered an isolated volume of granular material flowing past the obstacle. The flowing granular material mimicked a snow avalanche in an area of 11–22×28 m^2 around the obstacle (the exact size depended on the obstacle width). The particle flux was imposed at the up- and downstream boundary. We chose the boundary velocity such that it matched the vertical velocity profile of the selected avalanche scenario. In our setup, the x, y and z directions corresponded to the streamwise, transverse and vertical directions, respectively.

Estimating the material properties of snow mobilized by avalanches is challenging because most studies on the mechanical properties of snow are related to snow samples from an undisturbed snowpack (e.g., Shapiro et al., 1997; Scapozza, 2004), and from small-scale chute experiments (e.g., Salm, 1964; Rognon et al., 2008a). However, to the best of our knowledge, the mechanical properties of snow inside avalanches, where snow may experience large shear rates and thermo-mechanical transformations (Steinkogler et al., 2015; Kern et al., 2009), is not available. This lack of information led us to use available data on undisturbed snow. For this reason, our study's model parameters must be considered with caution: they are plausible values, not measured ones. In this paper, we use the material properties and contact law parameters used in chapter 2. Table 4.1 is a list of the most important material parameters used. Further information on how the contact forces were modeled and our code can be found in chapters 2 and 3.

Table 4.1 – Material properties for the Discrete Element Method (DEM) simulations.

Parameter	Symbol	Value / Range
Particle radius	r_p	40 ± 8 mm
Particle density	ρ_p	500 kg/m^3
Bulk density[†]	ρ_b	338–379 kg/m^3
Young's modulus	E	10^5 Pa
Friction coefficient	μ	0.5

[†] ρ_b results from ρ_p and interstitial voids between the particles and is not a controllable input parameter.

4.2.2 Obstacle geometries

Vallée de la Sionne measurement obstacles in DEM

In this study, we used measurements collected at the Vallée de la Sionne site to test whether our DEM model was able to reproduce impact pressure measurements on obstacles and sensors of different sizes and geometries. In Vallée de la Sionne, the test site's release area covers 30 ha, and it feeds two main corridors that converge just upstream of the zone where the obstacles and sensors are located (near 1700 m a.s.l.) (Ammann, 1999). Since the late 1990s, more than 70 avalanches (involving artificial and natural releases) have reached the obstacles and have been recorded. Figure 4.1 shows side views of the three obstacles in Vallée de la Sionne and the positions of the pressure sensors. These obstacles include a steel pylon of rectangular cross-section, a small concrete wall and a narrow steel wedge (Sovilla et al., 2010; Sovilla et al., 2014). We implemented these geometries in our DEM to simulate avalanche pressure on the Vallée de la Sionne obstacles.

The pylon is a 20 m tall steel cantilever with an elongated cross-section in the flow direction of

$1.6 \times 0.6\,\text{m}^2$. It is equipped with 6 cylindrical pressure sensors with a vertical spacing of 1 m from 0.5 m to 5.5 m above the ground. The cylindrical sensors have a diameter of 0.1 m and protrude upstream into the flow. The avalanche flow velocity is measured at the pylon using 46 optoelectronic sensor pairs vertically distributed from 0.25 m up to 6.0 m above the ground (Kern et al., 2010). In the DEM simulations, we reproduced the exact cross-section of the pylon but chose a smaller vertical spacing of 0.26 m instead of the 1 m between the pressure sensors on the real measurement pylon in Vallée de la Sionne to enhance the resolution of the vertical pressure profile. The spacing of 0.26 m corresponded to the vertical location of every second velocity sensor on the pylon.

The second obstacle is a narrow wedge with a flat beam mounted at the leading edge with a frontal width of 0.24 m and a height of 4.5 m. The beam accommodates four cylindrical pressure sensors with a diameter of 0.25 m, which protrude upstream into the flow. The sensors are located 1.3 m, 2.3 m, 3.3 m and 4.3 m above the ground. The sidewall of the wedge is at an opening angle of 5° from the symmetry axis of the obstacle in the flow direction. Instead of the flat beam at the front and the small wedge angle of 5°, our DEM codes approximated the wedge with a flat front and parallel side walls, similar to a rectangular cross-section. As for the real measurement structure, we implemented the cylindrical pressure sensors of diameter 0.25 m protruding upstream from the beam at the same locations above the ground.

The third obstacle in Vallée de la Sionne is a concrete wall, 1.0 m in width and 4.5 m in height. There, the impact pressure is measured using two types of sensors. The first probe consists of a 1 × 1 m measurement plate centered at a height of 3 m above the ground. The second type involves three cylindrical pressure sensors identical to the ones used on the pylon, which are located in the middle of the wall at 1.5 m, 2.25 m and 3.75 m above the ground. These cylindrical pressure sensors were mounted in 2015. The DEM code reproduced the exact geometry and positions of the 1 × 1 m measurement plate and cylindrical sensors, although the cylindrical sensors are not present in measurements older than 2015.

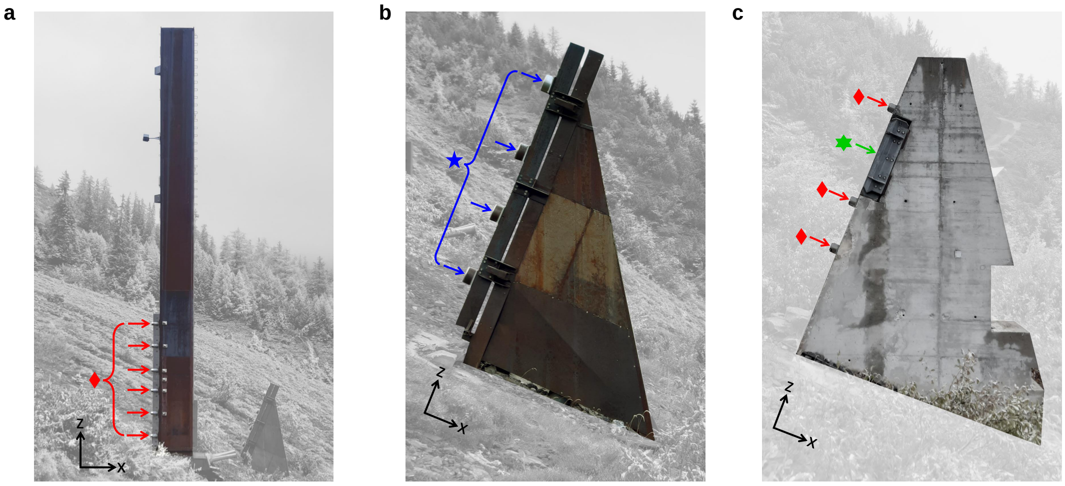

Figure 4.1 – Vallée de la Sionne measurement obstacles. Panels a, b and c show side views of the pylon, wedge and wall obstacles, respectively. The positions of the cylindrical sensors with a diameter of 0.1 m (red diamond), the cylindrical sensors with a diameter of 0.25 m (blue five-pointed star) and the 1 m^2 measurement plate (green six-pointed star) are highlighted with arrows in the corresponding colors.

Generic obstacles in DEM

To obtain a broader understanding of how impact pressure is affected by obstacle shape and size, we additionally simulated the interaction between avalanches and prismatic obstacles, including rectangular, circular and triangular cross-sections. Varied widths were considered. These geometries are commonplace in buildings, dams, cable car stations, protection structures and other infrastructures in avalanche-prone terrain. For all these obstacles, we chose a height of 5.7 m, which corresponded to the height of the highest velocity probe on the pylon (see section 4.2.2). This height was sufficient to prevent the granular mass from overflowing the obstacle.

For the rectangular obstacles, the width w of the faces normal to the flow direction could be varied. The faces parallel to the flow direction were 1.6 m long in all simulations, which corresponded to the length of the pylon. For the triangular obstacles, we used wedges whose apex angle was $\alpha = 60°$ and which faced the flow. The wedge base was normal to the flow direction, and its width w could be altered.

Finally, for the cylindrical obstacles with circular cross sections, the width w was the diameter. For all cross-sections we used the following array of values: $w = [0.24, 0.6, 1.0, 3.0, 6.0]$ m. The widths $w \leq 1$ m matched the widths of the Vallée de la Sionne measurement obstacles.

In order to investigate how the impact pressure was distributed on the obstacles, the obstacles' surface was discretized into smaller areas. In the vertical direction, we divided all rectangular, triangular and cylindrical obstacles into 22 sections, each 0.26 m in height, which again corresponded to the vertical location of every second velocity sensor on the pylon (see section 4.2.2). In the horizontal direction, we further divided the obstacle surfaces facing the granular flow into segments of equal widths. For most simulations the segment width was approximately 0.1 m. Only for the very narrow obstacles with $w = 0.24$ m, the segments were approximately 0.05 m wide to obtain a higher resolution of the impact pressure distribution. From left to right, Figure 4.2 shows a perspective view of a rectangular, cylindrical and triangular obstacle with a width $w = 1$ m.

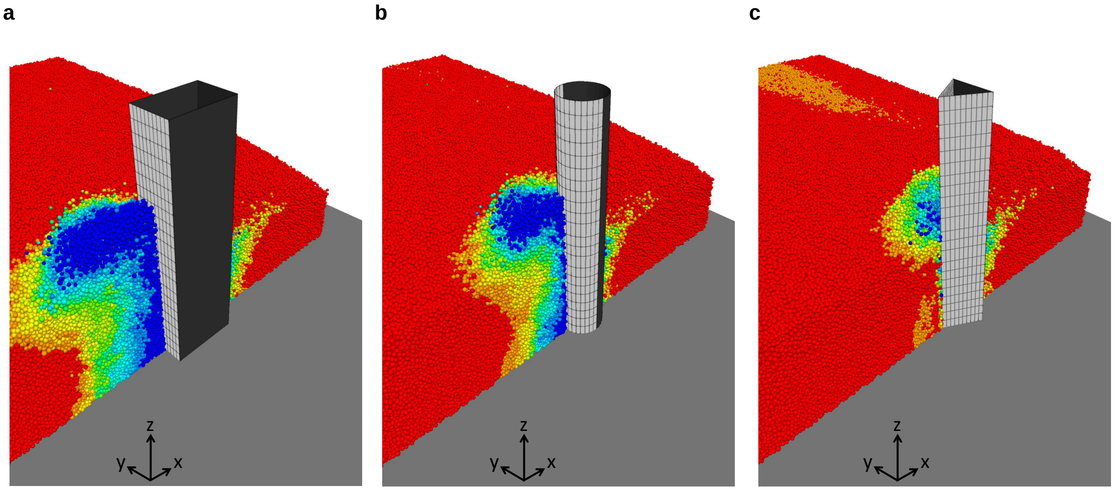

Figure 4.2 – Perspective views of the obstacles with a rectangular (a), circular (b) and triangular (c) cross-section. The black grid visualizes the discretization of the impact surface (shown in light gray). The obstacles are shown while interacting with an avalanche, which is cut vertically in the middle of the flow domain. The particles are colored according to their streamwise velocity, where red corresponds to 3 m/s and blue to 0 m/s.

4.2.3 Avalanche scenarios

Generic avalanche scenarios in DEM

In our study, we selected four typical scenarios of flow avalanches based on the data collected over the last 20 years at the Vallée de la Sionne test site (Köhler et al., 2018b; Kern et al., 2009). These include two scenarios of fast avalanches and two scenarios of slow avalanches. The fast-avalanche scenarios are mostly relevant for avalanches in the fully developed flow regime, whereas the slow-avalanche scenarios would better describe avalanches in the runout phase.

- **Cold shear flow regime** (also called cold dense flow regime in Köhler et al. (2018b)): this regime is characterized by a nonuniform vertical velocity profile, with velocity increasing substantially from the bottom (where it is close to zero) to the free surface of the flow (where it can be as high as 30 m/s in Vallée de la Sionne). This velocity profile implies that the flow experiences high frictional resistance at its base. Owing to high velocities, cold shear flows are often supercritical ($Fr > 1$) and are therefore considered inertial flows. The cold shear flow regime is also typical of the dense core in powder snow avalanches. The avalanche's dense layer is usually shallow, with flow depths of less than 4 m (Köhler et al., 2018b). To model this scenario, we simulated a velocity profile increasing linearly from 0 m/s at the bottom to 30 m/s at the flow's free surface. We considered a flow depth of 2.5 m for all runs. Cold snow below $-1\,^{\circ}$C usually exhibits low cohesion (see section 1.1), and we thus simulated a cohesionless granular material with the cohesive bond strength $\sigma_{coh} = 0.0$ kPa for this scenario.

- **Warm shear flow regime:** this regime refers to cases for which the vertical velocity profile may reach peak values of $v \simeq 25$ m/s. In contrast to cold snow, the snow in warm avalanches is considered to be highly cohesive, which may lead to large snow aggregation (clogging) within the avalanche (Köhler et al., 2018b; Rognon et al., 2008b; Rognon et al., 2006). Snow clogging is, however, counterbalanced by fragmentation induced by collisions and high velocities within the flow. The vertical velocity profile is similar to that observed for the cold shear flow regime (Köhler et al., 2018b). We simulated the warm shear flow regime with the same flow depth (2.5 m) and, despite the small velocity deviation, with the same vertical velocity profile as in the cold shear flow regime. To account for the high cohesion, we set the cohesive bond strength to $\sigma_{coh} = 10.0$ kPa. This cohesive strength value is higher than the back-calculated σ_{coh} for a range of typical warm avalanches documented by Sovilla et al. (2010), but lower than for extremely cohesive avalanches (chapter 2).

- **Cold plug flow regime:** this regime is characterized by a low shear rate in the vertical velocity profile above the sliding surface (Kern et al., 2009). Because the cold snow in this type of avalanche has little or no cohesion, a uniform velocity profile (plug flow) is observed when basal friction is low. On the contrary, a sheared velocity profile develops when the basal friction is sufficiently high. Plug flows typically occur in the tail of large cold snow avalanches, after the avalanche head has smoothed out the sliding surface, or in the runout of a cold, dry dense avalanche. Indeed, in this flow regime, velocities are usually lower than 10 m/s, which is often the case in the runout zone. Owing to the low velocity, cold plug flows are mostly subcritical ($Fr < 1$) and are, therefore, considered to be gravitational avalanches. In this flow regime, impact pressure is proportional to flow depth and independent of flow velocity (Sovilla et al., 2010). To model this regime, we simulated a granular mass moving at an arbitrary velocity of 3 m/s uniformly across the flow depth. The flow was assumed to be cohesionless (cohesive strength $\sigma_{coh} = 0.0$ kPa). The flow depth was 2.5 m.

- **Warm plug flow regime:** this regime, defined by Köhler et al. (2018b), is often observed for avalanches with snow temperature close to 0°C. This flow regime is typical of dense wet snow avalanches. The snow in such avalanches is highly cohesive, and thus experiences clogging. The avalanche takes the form of a slow displacement of blocks gliding along the ground or snow cover (Köhler et al., 2018b; Issler, 2003). To model this regime, we simulated a flow identical to the one in the cold plug flow regime, but with a cohesive strength of $\sigma_{coh} = 10$ kPa between the particles. Although the flow depth can reach $5-7$ m (Sovilla et al., 2016), we still considered a flow depth of 2.5 m for the sake of comparison with the other flow regimes and to reduce the computational effort.

We summarize the properties of these four flow scenarios in Table 4.2 a.

Vallée de la Sionne avalanche scenarios in DEM

In order to test our DEM model, we compared simulated to measured impact pressure on the obstacles in Vallée de la Sionne. Hence, we needed to select recordings from the Vallée de la Sionne measurement archive, in which the three obstacles, located within an area of 16.5 m in radius, were hit simultaneously by the flow. For these real-world avalanche scenarios, we chose two typical examples including a warm plug flow regime avalanche and a cold shear flow regime avalanche, which are described below. To be able to compare impact pressure between real-world and simulated avalanche flows, we chose a vertical velocity profile in the simulations that came closest to the velocity profiles measured at the pylon.

- The February 1st 2013 avalanche (naturally released) is a typical example of the warm plug flow regime. Because the avalanche flow characteristics also evolve with time, we selected a sequence of 3 s from the complete recording with a duration of 4 minutes in the Vallée de la Sionne measurement database. In this selected time window, the avalanche's dense flow was moving at ~ 2.5 m/s and had a flow height of approximately 2.7 m. The sliding surface was roughly 1.2 m above the ground. We compared these measurements to simulations where a constant velocity of 2.5 m/s was imposed across the entire flow depth of 3 m. The cohesive strength was set to $\sigma_{coh} = 5.0$ kPa. This value corresponds to a moderate cohesion and is in the middle of the cohesion-less and highly cohesive scenarios defined in section 4.2.3. Moreover, it is in the range of the back-calculated cohesion values for which we to obtain a good agreement between computed and measured impact pressures for a number of warm plug flow avalanche events in Vallée de la Sionne (Sovilla et al., 2010).

- For the experimental data related to the cold shear flow regime, we selected measurements from an artificially released large powder snow avalanche on 8 March 2017. As done previously, we extracted a sequence of 1 s, during which the flow depth of the avalanche's basal flow was ~ 2.5 m. The velocity increased from 0 m/s at the ground to ~ 40 m/s at 2.5 m above the ground. For the comparison, we simulated a flow with a velocity profile increasing linearly from 0 m/s at the ground to 40 m/s at the free surface 2.5 m above the ground. For cold shear avalanches, we expected snow cohesion to be low and thus selected a cohesive strength of $\sigma_{coh} = 0.0$ kPa.

We summarize the two avalanche scenarios in Table 4.2 b.

Table 4.2 – Simulated avalanche flow scenarios.

Flow regime[†]		Typical application[‡]	Velocity profile v	Cohesion σ_{coh}	Flow height h
a) Generic avalanche scenarios in DEM					
gravitational	cold plug |	tail of dry flow avalanche runout	3 m/s constant	0.0 kPa	2.5 m
	warm plug |	wet flow avalanche track, runout	3 m/s constant	10.0 kPa	2.5 m
inertial	cold shear /	dry dense core of powder avalanche track	0–30 m/s shear	0.0 kPa	2.5 m
	warm shear /	wet dense core of powder avalanche track	0–30 m/s shear	10.0 kPa	2.5 m
b) Vallée de la Sionne avalanche scenarios in DEM					
gravitational	warm plug |*	wet flow avalanche track, runout	~ 2.5 m/s constant	5.0 kPa	2.7 m
inertial	cold shear /*	dry dense core of powder avalanche track	0–40 m/s shear	0.0 kPa	2.5 m

[†] Distinction of flow regimes based on Fr and (Steinkogler et al., 2015; Köhler et al., 2018b).
[‡] Avalanche types according to (Quervain, 1981) and
avalanche zones according to (McClung and Schaerer, 2006).

4.3 Comparison of simulated and measured impact pressure on obstacles of varied geometry

In this section, we show that our model was able to simulate the impact pressures on obstacles of different geometries and in different flow regimes. To that end, we compared simulated and recorded impact pressures by implementing pylon, wall and wedge obstacles—described in section 4.2.2—in our DEM code and matched the simulated velocity profile to the velocity measured at the pylon. The first and second rows of Figure 4.3 show the simulated and measured impact pressures in the warm plug flow regime (|*) and the cold shear flow regime (/*), respectively, as described in section 4.2.3.

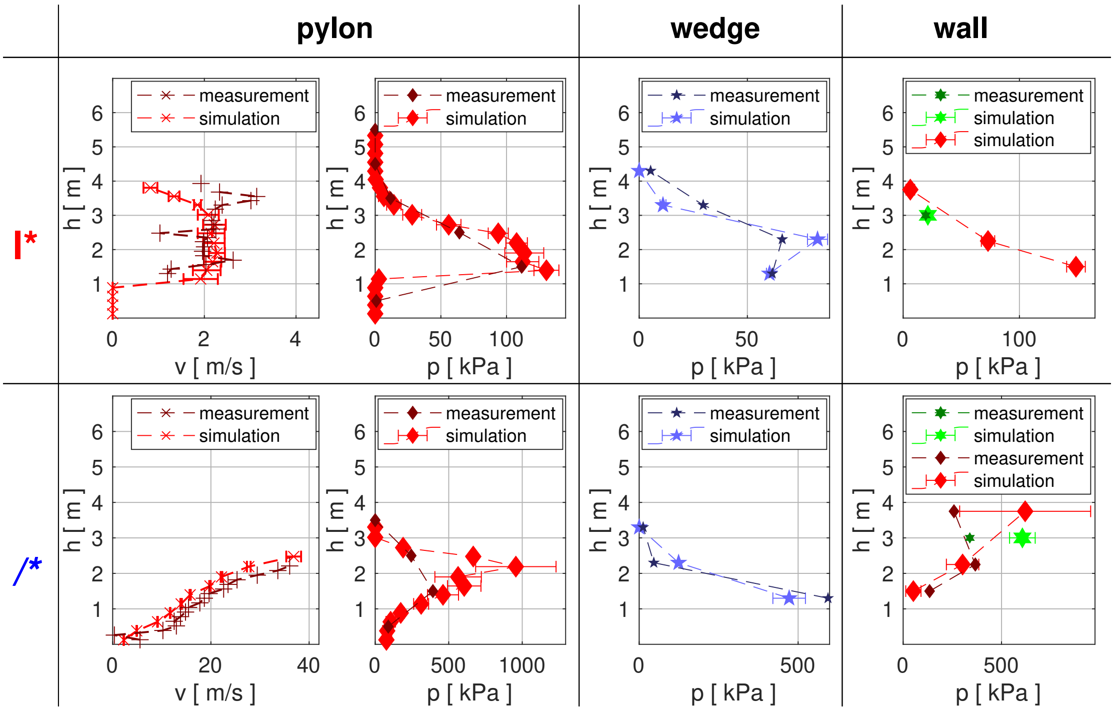

Figure 4.3 – Comparison of simulated and measured impact pressure on the Vallée de la Sionne obstacles. The plots in the first column show the measured (dark red) and simulated (light red) velocity at the pylon. The plots in the second, third and fourth columns show the measured and simulated pressure on the pylon, wedge and wall, respectively. The first and second rows show the impact pressure exerted by an avalanche in the warm plug and cold shear flow regime, respectively. The symbols represent the measured (dark colors) and simulated (light colors) impact pressure on the cylindrical sensors with diameters of 0.1 m (red) and 0.25 m (blue), as well as the 1 m^2 (green) sensor plate. These colors and symbols correspond to the illustration in Figure 4.1.

The comparison exercise in Figure 4.3 demonstrates a good general agreement between the simulated and measured impact pressures in the warm plug flow regime (|*) and the cold shear flow regime (/*). We observe that the model is able to capture the pressure differences measured by the different sensors at the three obstacles. This can be best seen by comparing the pressure on the wall with the square sensor of 1.0 m^2 area in the right column to the pressure values obtained for the cylindrical sensors with a diameter of 0.1 m. For the wall no measurements of the cylindrical sensors are available because these sensors were not yet mounted when this avalanche occurred in 2013 (see section 4.2.2). However, the simulated pressure on the cylindrical sensors with a diameter of 0.1 m sensors on the wall is in good agreement with the pressure measured on the pylon with the same sensors and at the same height. In the warm plug flow regime (wall, |*), the simulated and measured pressures on the 1.0 m^2 sensor were considerably lower than the expected pressure for the smaller cylindrical sensors given by the linear interpolation of the values of the sensors at 2.25 m and 3.75 m above the ground.

In the middle (wall,|*), the pressure on lowest cylindrical sensor was lower than on the sensor at 2.2 m above the ground, which deviated from the proportionality of the pressure with the flow depth in the gravitational regime (e.g., Sovilla et al., 2010; Wieghardt, 1975; Albert et al., 1999). However, this could be explained by the fact that the sensor at 1.2 m above the ground was already partially inside the avalanche deposit and therefore not impacted by the avalanche at full thrust.

In the cold shear flow regime (wall,/*), the simulated and measured impact pressures on the larger sensor were higher than on the small sensors. This was the opposite of what we observed in the warm plug flow regime (wall,|*). The qualitative agreement between simulations and measurements for the two different sensor types and in both flow regimes shows that the simulations were able to reproduce the measurements.

We did, however, observe differences between the simulated and the measured impact pressures. In the warm plug flow regime (wall,|*), the simulated pressure on the wedge obstacle increases at a moderately higher rate with flow depth and has a higher pressure peak compared to the measured pressure.

For the cold shear flow impacting the wall (wall,/*), the pressure on the highest cylindrical sensor at the wall 3.75 m above the ground was considerably higher in the simulation than in the measurement. In this case, the uppermost cylindrical sensor in the simulation was impacted by the dense flow. In the measurement of the powder snow avalanche, the sensor might already have been inside the powder cloud or the more dilute flow surrounding the dense layer, which would have exerted less pressure on the sensor.

4.4 Average impact pressure exerted on obstacles of different geometries

In Figure 4.4 a, we show the simulated impact pressures on obstacles of rectangular (□), circular (○) or triangular (△) cross-section of varied width exerted by an avalanche in the cold plug (|) and warm plug (|) flow regime scenarios defined in Table 4.2 a. In both flow regimes, the impact pressure was highest on the rectangular cross-section. On average, the impact pressure on the circular and triangular cross-sections was 17% and 43% lower, respectively, than the pressure on the rectangular cross-sections.

We also observed that the impact pressure p_x decreased with increasing obstacle width for all cross-sections. The impact pressure exerted by a cold plug flow decreased by only 2.7 kPa from $p_{x,w=3\,\mathrm{m}}$ to $p_{x,w=6\,\mathrm{m}}$, while the pressure decreased by 4.6 kPa from $p_{x,w=0.24\,\mathrm{m}}$ to $p_{x,w=0.6\,\mathrm{m}}$ with a much smaller change in w. The decrease in the rate of change in p_x for increasing w indicates that from a certain w value, p_x no longer decreased significantly with further increases in w. As the impact pressure decrease rate with increasing w was already low for $w = 6\,\mathrm{m}$, we assumed that the pressure decrease for $w > 6\,\mathrm{m}$ was negligible. Hence, we used the impact pressure on the widest obstacle $p_{x,w=6\,\mathrm{m}}$ as an approximation of the impact pressure on wider obstacles. In order to quantify the pressure increase on a narrow obstacle compared with that on a wide obstacle in Figure 4.4 b, we divided the impact pressures of varied widths p_x by the impact pressure on the widest obstacle $p_{x,w=6\,\mathrm{m}}$ of the same cross-section type and flow regime.

Figure 4.4 b shows that the pressure decrease in the cold plug flow on obstacles of increasing width was similar for all cross-sections. $p_{x,w=0.24\,\mathrm{m}}$, $p_{x,w=0.6\,\mathrm{m}}$, $p_{x,w=1\,\mathrm{m}}$ and $p_{x,w=3\,\mathrm{m}}$ were on average 2.0, 1.7, 1.6 and 1.2 times higher, respectively, than $p_{x,w=6\,\mathrm{m}}$. In the warm plug flow regime we observed the highest ratio $p_{x,w=0.24\,\mathrm{m}}/p_{x,w=6\,\mathrm{m}} = 2.6$ for the circular cross-section and the lowest value $p_{x,w=0.24\,\mathrm{m}}/p_{x,w=6\,\mathrm{m}} = 1.8$ for the triangular cross-section. Hence, the differences between the pressure ratios of different cross-sections in the warm plug flow regime (|) were slightly larger than the values in the cold plug flow regime (|).

Figure 4.4 c shows the simulated impact pressures on obstacles of varied width exerted by an avalanche in the cold shear (/) and warm shear (/) flow regimes. Similar to in panel a, the impact pressure was highest on the rectangular obstacles, while 22% and 45% less impact pressure was exerted on the cylindrical and triangular obstacles, respectively. The impact pressure increase from the cold shear (/) to the warm shear (/) flow regime due to cohesion was of a factor 1.7 on average. This was considerably lower than the impact pressure increase due to cohesion of a factor of 3.2 in the gravitational regime (|,|).

For all obstacles impacted by the cold shear (/) and warm shear (/) flow avalanche, the pressure decreased for $0.24\,\mathrm{m} \leq w \leq 1\,\mathrm{m}$. For $w > 1\,\mathrm{m}$ the impact pressure either decreased further or increased slightly, depending on the geometry and flow regime.

In Figure 4.4 d, we scaled p_x by $p_{x,w=6\,\mathrm{m}}$ of the same geometry and flow regime, similar to the gravitational flows, although the qualitative trend in p_x was not consistent. Panel d shows more clearly that in the inertial flows (/,/), the dependency of the impact pressure on the obstacle width was generally lower than for the gravitational flows (|,|).

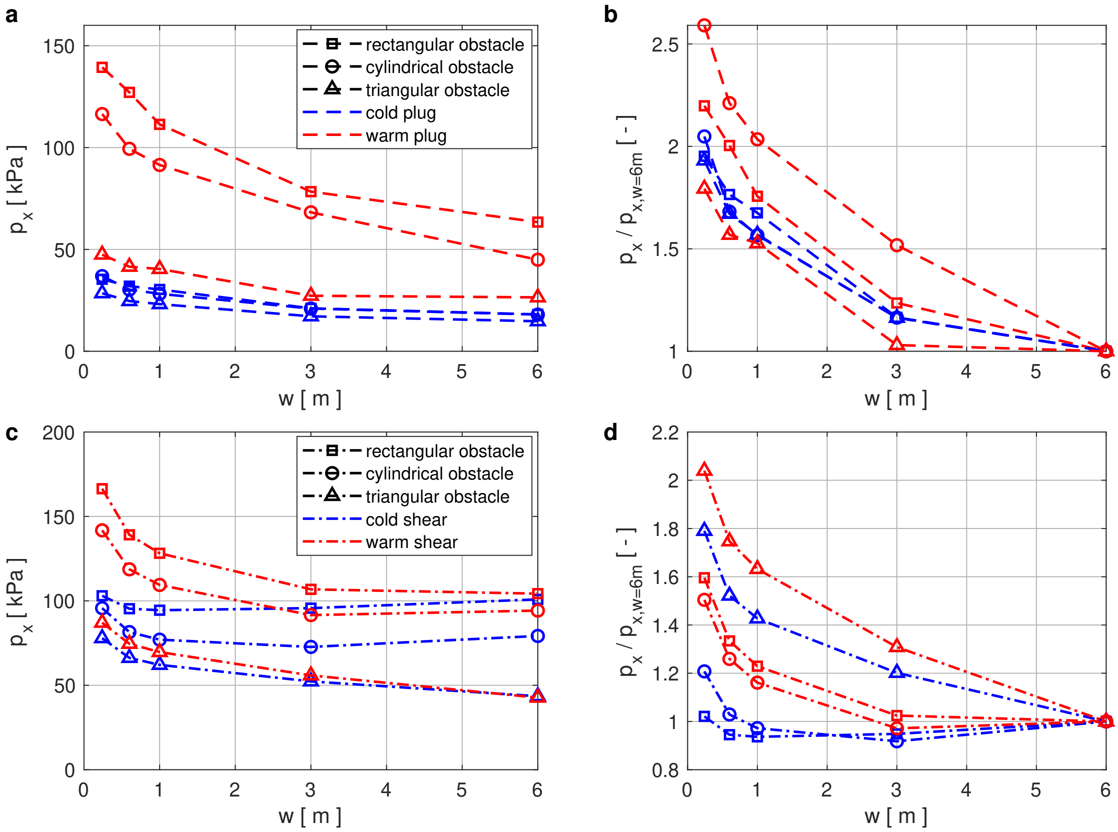

Figure 4.4 – Dependence of impact pressure p_x on obstacle geometry and width w. Panel a shows the impact pressure exerted by a cold plug (dashed, blue) and a warm plug (dashed, red) avalanche flow. Panel c shows the impact pressure exerted by a cold shear (dash-dotted, blue) and a warm shear (dash-dotted, red) avalanche flow. Panels b and d show the impact pressure for obstacles of varying width w relative to the pressure on the 6 m wide obstacle of the same geometry and flow regime in the gravitational and inertial flow regimes, respectively.

4.5 Pressure distribution on obstacles of different geometries

In this section, we present how the impact pressure was distributed on the obstacle surface. For the tested obstacle of width $w = 1$ m, in Figure 4.5, we visualize the distribution of the impact pressure exerted by avalanches of four flow regimes (see section 4.2.3) on obstacles with different cross-sections.

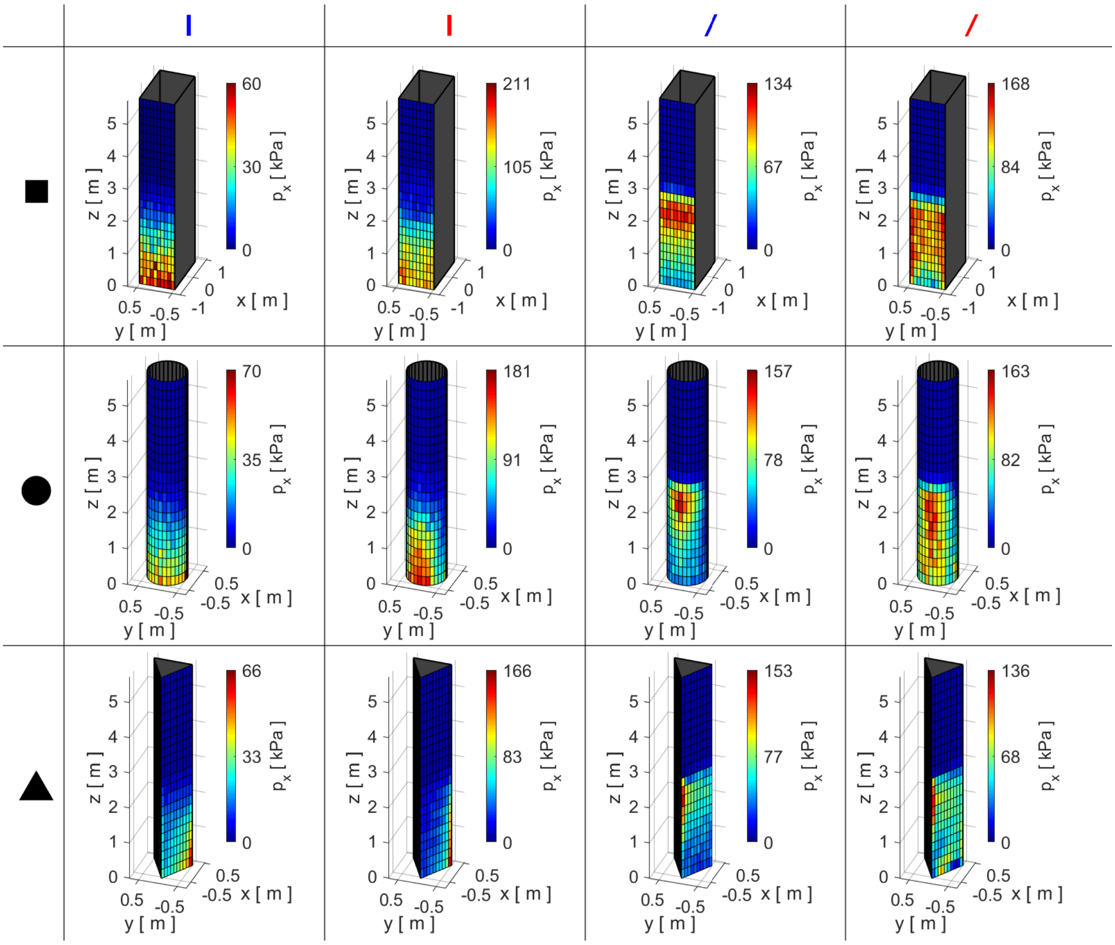

Figure 4.5 – Impact pressure distribution on the discretized impact surface of the prismatic obstacles (w = 1 m) with a rectangular, circular or triangular cross-sections. From left to right the columns show the pressure distribution in the cold plug, warm plug, cold shear and warm shear flow regimes. The colors represent the average impact pressure magnitude on the respective surface.

In the first two columns of Figure 4.5, we observe that the impact pressure was largest at the bottom of the avalanche flow for the plug flow regimes (|,|). For the cold shear flow regime (/) in the third column, the impact pressure was highest at the flow surface, 2.5 m above the ground. In the warm shear flow regime (/), in the right column, the highest pressure was also located near the flow surface, but the pressure peak was more spread out towards the ground compared with in the cold shear regime (/).

In the horizontal direction, the pressure distribution was variable for the different geometries and flow regimes. In order to analyze the horizontal pressure distribution more closely in Figure 4.6, we plotted the impact pressure as a function of the y coordinate transverse to the flow direction at different heights z. To improve the visibility of the horizontal pressure variations, we scaled the local impact pressure $p_x(y,z)$ by the average pressure $p_{x,mean}(z)$ at the respective height and the y coordinate with the width w of the obstacle.

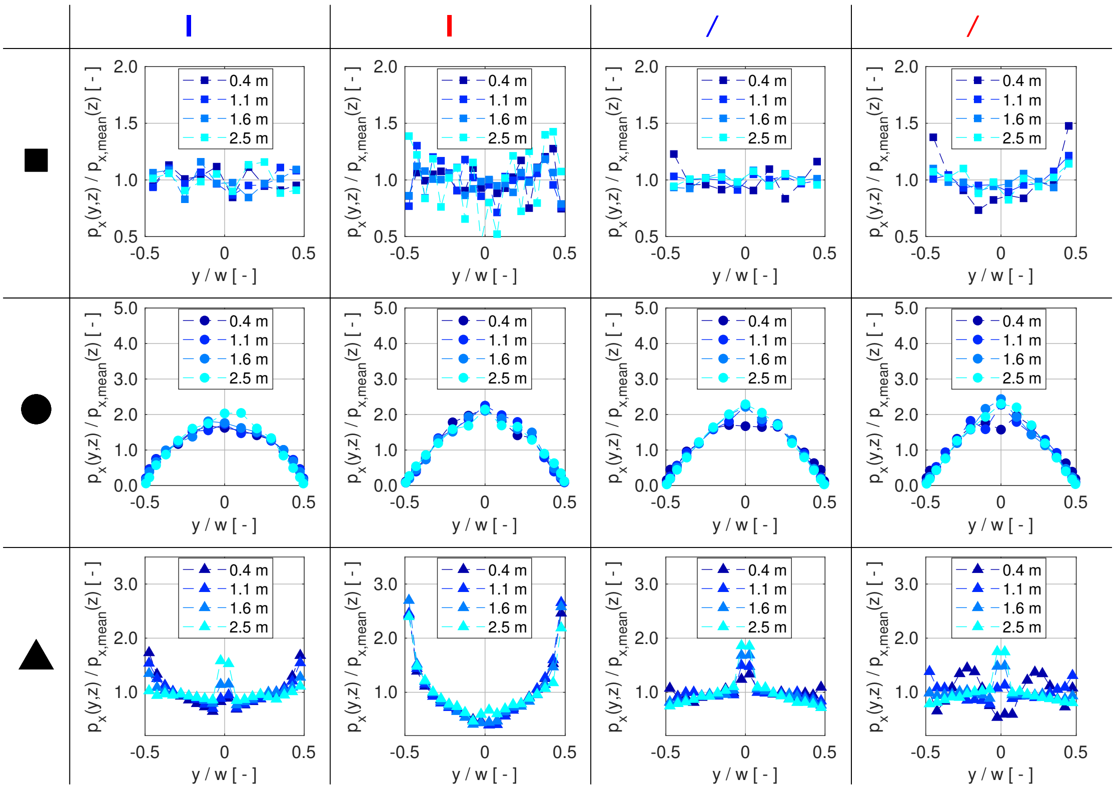

Figure 4.6 – Horizontal pressure distribution on obstacles with $w = 1$ m normalized by the average pressure at the respective height. The first, second and third rows show the pressure distribution on the obstacles with rectangular, circular and triangular cross-sections, respectively. From left to right the columns show the pressure distribution in the cold plug, warm plug, cold shear and warm shear flow regimes.

In the first row in Figure 4.6, we observe that the impact pressure on the rectangular obstacle (□) exerted by the cold regimes (|,/) was evenly distributed in the *y*-direction. In contrast, the impact pressure exerted by the warm regimes (|,/) was up to ~ 1.5 times higher at the outer edges than in the middle of the obstacle. In the warm shear regime (/), these pressure concentrations at the edges were most pronounced at the bottom of the flow.

For the circular cross-sections (◯) in the middle row, the pressure distribution showed no significant differences for the four flow regimes tested. The impact pressure was highest in the middle of the obstacle, where the flow impacted the obstacle at a right angle, and was lowest at the sides where the obstacle surface was tangential to the flow.

Depending on the flow regime and flow depth, the horizontal pressure distribution on the triangular obstacles (△) in Figure 4.6 shows pressure concentrations both at the obstacle outer edges and at the leading edge. A pressure peak at the leading edge of ~ 2 times the average pressure was present in most cases (|,/,/), but not in the warm plug regime (|) or near the ground for the warm shear regime (/). A pressure peak at the outer edges of the obstacle, where the pressure was up to ~ 2.5 times higher than the average pressure, occurred across the whole flow height in the warm plug regime (|) and was most pronounced near the ground in the cold plug regime (|).

4.6 Impact pressure calculation

Here, we propose a physics-based and practice-oriented method for estimating C_D values depending on the obstacle geometry and the avalanche flow characteristics. In section 4.6.1, we present a method for estimating C_D for cohesionless avalanches (e.g., |,/), which are often relevant in practice, as they are representative of dry fast avalanches in the avalanche track and runout. In section 4.6.2, we show how the impact pressure increase caused by cohesion (e.g., |,/) can be calculated.

4.6.1 Estimation of drag coefficients for cohesionless avalanches

Based on similar findings in previous studies (Thibert et al., 2008; Gauer and Kristensen, 2016; Faug, 2013; Thibert et al., 2015), we propose a physics-based definition of the drag coefficient C_D, similar to equation (1.4), as follows:

$$C_D = C_{geo}\, C_r = C_{geo}\left(1 + \frac{K}{Fr^2}\right) \tag{4.1}$$

where we first divide C_D into two factors (Thibert et al., 2008): (1) C_{geo}, which is solely related to the geometry of the obstacle, and (2) C_r, which depends on the flow regime of the avalanche. Furthermore, we rewrite the coefficient C_r according to equation (1.6) (Thibert et al., 2013; Faug, 2013).

The average impact pressure of an avalanche with a flow depth h and velocity v can be calculated according to equation (4.2):

$$p_{x,calc} = C_D \frac{\rho}{2} v^2 = C_{geo} \frac{\rho}{2} v^2 + \zeta \rho g \frac{h}{2} \tag{4.2}$$

where we use the definition of $Fr = v/\sqrt{g\,h}$ and set $\zeta = C_{geo}K$ to obtain a formulation similar to that used by Sovilla et al. (2016).

For the gravitational plug flow regime (|) in Figure 4.4 a, we find that the impact pressure decreased for obstacles of increased width for all geometries. Hence, as shown by equation (4.3), we further decompose the geometry factor C_{geo} into a coefficient C_o considering only the obstacle's geometrical shape and a coefficient $C_w = p_x/p_{x,w=6\,\mathrm{m}}$ depending on the obstacle width, as presented in Figure 4.4.

For the impact of avalanches in the inertial shear flow regime (/) in Figure 4.4 c, the width influence was not monotonic or similar for all geometries. For lack of a better understanding of the physical processes involved, and given the qualitative trend exhibited by the width influence on the pressure in these regimes, we set $C_w = 1$ in the cold shear (/) flow regime for all w:

$$C_{geo} = C_o\, C_w \tag{4.3}$$

To estimate the geometrical part C_o of the drag coefficient C_{geo} of an obstacle, for which C_o is not known *a priori*, we propose the heuristic equation (4.4). This method is based on the concept that the resistance to the flow offered by a flat body scales with the cosine of its angle to the flow's direction transverse (the y-direction in our setup). Hence, we discretize the obstacle's impact surface into n piecewise straight segments at an angle θ_n and of width d_n and calculate C_o as the sum of the weighted contributions of the individual straight segments as in equation (4.4). A prerequisite for applying equation (4.4) is that the obstacle's impact surface facing the upstream direction of the flow must be convex.

$$C_o = 1 + \frac{1}{w}\sum_n \cos\theta_n\, d_n \tag{4.4}$$

From equation (4.4), we can identify two limiting cases: (1) $C_o = 1$ for an infinitely narrow object parallel to the flow, and (2) $C_o = 2$ for an obstacle of finite width with a flat face at a right angle to the flow direction. Figure 4.7 a illustrates equation (4.4). Figure 4.7 b shows examples calculations of C_o for the geometries considered in this study.

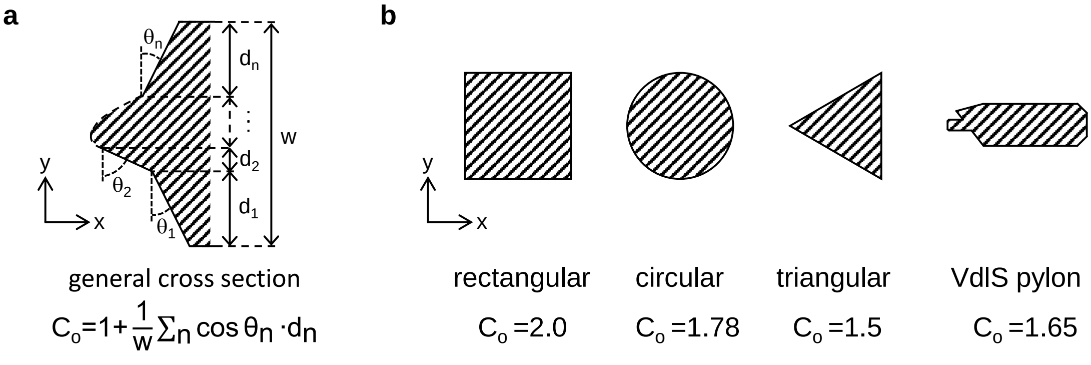

Figure 4.7 – C_o estimation based on equation 4.4 for a general cross-section in panel a and for selected cross-sections in panel b. VdlS = Vallée de la Sionne.

The remaining factor to be determined in equation (4.1) is K, which is associated with the depth-dependent impact pressure contribution of gravitational avalanches (Sovilla et al., 2010). In the gravitational flow regime, the impact pressure on the structure predominantly originates from the material compression inside the flow region, which is influenced by the presence of the obstacle ((Chehata et al., 2003) and chapters 2, 3). The compression of the granular material is mainly caused by particle jamming due to the resistance to the flow offered by the obstacle. Because flow resistance depends on the obstacle geometry, we use C_o as a proxy for how much the material is jamming upstream of the obstacle rather than being deflected. Confined compression tests on a granular material with the same properties as in this study have shown that the axial stress scales approximately with the square of the particle compression (chapter 3). Hence, as an approximation, we set the factor $K = C_o$ such that the second term of the regime-dependent coefficient C_r scales with C_o^2. Considering compression tests of the granular material for calibrating K is in line with the original idea of Faug (2013), where K corresponds to the *pure earth pressure coefficient*, as this accounts for the material's mechanical properties and stress state under compression. Finally, using $K = C_o$, we obtain equation (4.5) for estimating the drag coefficient C_D, which can be used with equation (1.1) to calculate the impact pressure.

$$C_D = C_{geo}\, C_r = C_{geo} + \frac{C_{geo}\, K}{Fr^2} = C_o\, C_w + \frac{C_o^2\, C_w}{Fr^2} \tag{4.5}$$

4.6.2 Impact pressure exerted by cohesive avalanches

Snow cohesion in an avalanche is only relevant for the flow behavior and the impact pressure above a certain cohesion threshold (Steinkogler et al., 2015; Favier et al., 2013). The threshold is not a constant, but depends on the balance between the collisional forces, proportional to the flow velocity, and the cohesive strength between the particles. Below the threshold value, the flow exhibits a predominantly cohesionless behavior, because the collisional forces break snow aggregations apart. Above the threshold value, the avalanche snow is cohesive enough to aggregate more snow particles than the collisional forces can break. This interplay between collisional and cohesive forces, which also governs the impact pressure increase due to cohesion, can be captured by considering the Bond to Froude number ratio $q_{Bo,Fr} = Bo/Fr$ (chapter 2). The dimensionless Bond number $Bo = \sigma_{coh}/p_{conf}$ is the cohesive strength σ_{coh} divided by the confining pressure p_{conf} (Roy et al., 2017), which is the vertical component of the local stress tensor.

As already demonstrated in chapter 2, the impact pressure exerted by a cohesive avalanche $p^*_{x,calc}$ can be simply calculated according to equation (4.6), by multiplying a factor $f_{coh}(q_{Bo,Fr})$, based on the ratio of the Bond number, by the impact pressure exerted by a cohesionless flow with the same flow height and velocity $p_{x,calc}$:

$$p^*_{x,calc} = p_{x,calc}\, f_{coh}(q_{Bo,Fr}) \tag{4.6}$$

We assume that f_{coh} varies slightly depending on the obstacle geometry. However, many simulation runs with varying v and σ_{coh} are needed to obtain f_{coh} as a function of $q_{Bo,Fr}$ for a specific geometry, making it cumbersome to find f_{coh} for all geometries in this study. Hence, as an approximation, we use the scaling available in chapter 2 using the Vallée de la Sionne pylon, which we fit with equation (4.7):

$$f_{coh} = c_1/(c_2 + q_{Bo,Fr}) + c_3 \tag{4.7}$$

where $c_1 = -3.6$, $c_2 = 1.5$ and $c_3 = 3.4$ are the fitting parameters.

4.7 Comparison of calculated impact pressure with simulations and measurements

4.7.1 Cohesionless avalanches

Using the method for the estimation of C_o, C_w and K described in the previous section, we calculate the impact pressure $p_{x,calc}$ of a cold plug flow (|) and a cold shear flow (/) on obstacles of varied geometry. We compare the calculated and simulated impact pressure $p_{x,DEM}$, as shown in Figure 4.8.

For the calculation, we choose C_w according to the pressure ratios $p_x/p_{x,w=6\,\mathrm{m}}$ of the cold plug flow (|) in Figure 4.4 b and assume $C_w = 1$ in the cold shear regime (/) (see section 4.6.1). C_o is calculated using equation (4.4).

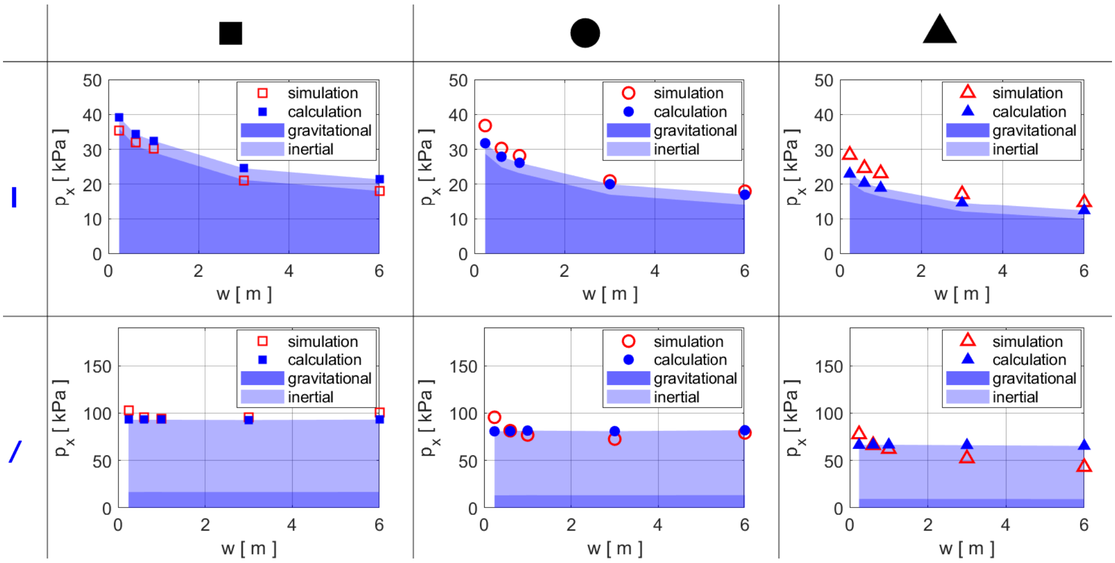

Figure 4.8 – Comparison of simulated impact pressure (red symbols) and pressure calculations (blue symbols) using equations (1.1) and (4.5) for varying obstacle widths w. The first, second and third columns show the pressure comparison for the obstacles with rectangular, circular and triangular cross-sections, respectively. The pressure exerted by an avalanche in the cold plug (first row) and the cold shear (bottom row) flow regime are shown. The dark blue shaded areas represent the calculated gravitational pressure contribution, where the impact pressure is proportional to the flow depth, while the light blue shaded areas represent the calculated inertial contribution, where the impact pressure is proportional to velocity squared.

In Figure 4.8, we observe that the calculated impact pressure agrees relatively well with the simulated values. For the impact pressures exerted by the cold plug flow (|) in the first row, the pressure on the rectangular obstacle is slightly overestimated, while the pressure on the cylindrical and the triangular obstacles is slightly underestimated for all obstacles widths. In the inertial cold shear flow regime (/), the influence of obstacle width on the pressure is not captured because we assume $C_w = 1$ in this regime for all w. The mean relative error between the simulated and the calculated pressure is 12% in the cold plug flow and 15% in the cold shear flow.

In the cold plug flow regime (|), the flow depth-dependent gravitational pressure contribution (dark blue area) is dominant, with a share of 85% of the total calculated impact pressure. Using equation (4.2), we can calculate the proportionality factor $\zeta = C_o^2 C_w$ is associated with the gravitational pressure contribution from the data in Figure 4.8. The corresponding ζ values in Figure 4.8 are $2.3 \leq \zeta \leq 7.9$, where the highest value corresponds to the narrowest rectangular obstacle and the lowest value corresponds to the widest triangular obstacle.

In the inertial cold shear flow (/) the pressure contribution proportional to velocity square (light blue area) has a share of 80% of the total calculated impact pressure. Hence, in this regime the geometry dependent coefficient C_{geo} prevails.

4.7.2 Real avalanche scenarios

To assess how realistic the drag coefficient is for a real-world avalanche, we calculate the vertical impact pressure profile for the warm plug (|*) and cold shear (/*) avalanches on the Vallée de la Sionne obstacles and compare it to the measured and simulated impact pressure in the real avalanche scenarios (|*,/*) described in section 4.2.3. Again, we estimate C_D values in the cohesionless flows, using the method proposed in section 4.6.1 to calculate the average impact pressure. In the warm plug regime (|*), we consider the impact pressure increase due to cohesion by calculating the pressure increase factor $f_{coh} = 1.94$ according to section 4.6.2, using the scaling law from chapter 2 with $Bo = 0.50$ and $Fr = 0.49$.

In order to calculate the vertical pressure profile, we calculate the gravitational and inertial pressure contribution from equation (4.2) individually. Subsequently, we use the proportionality of the pressure with the flow depth in the gravitational regime (e.g., Sovilla et al., 2010; Wieghardt, 1975; Albert et al., 1999) and with velocity squared in the inertial regime (e.g., Voellmy, 1955d; Voellmy, 1955c; Voellmy, 1955b; Voellmy, 1955a; Salm and Gubler, 1985; McClung and Schaerer, 1985) to determine the vertical distribution. Further information on how we calculated the impact pressure profiles is provided in the Supplementary Material in chapter C.

In Figure 4.9, we plot the simulated and measured impact pressures from Figure 4.3, and we compare it to the pressure calculations.

Figure 4.9 shows that the calculated vertical impact pressure profiles qualitatively agree well with the simulated and measured pressure profiles. For the cold shear flow regime (/*) impacting the wedge obstacle, the comparison is made difficult by the fact that the measured dense flow at this particular obstacle was probably below the sensor at 2.3 m above the ground, leaving only the lowest sensor at 1.3 m measuring the impact pressure of the dense flow.

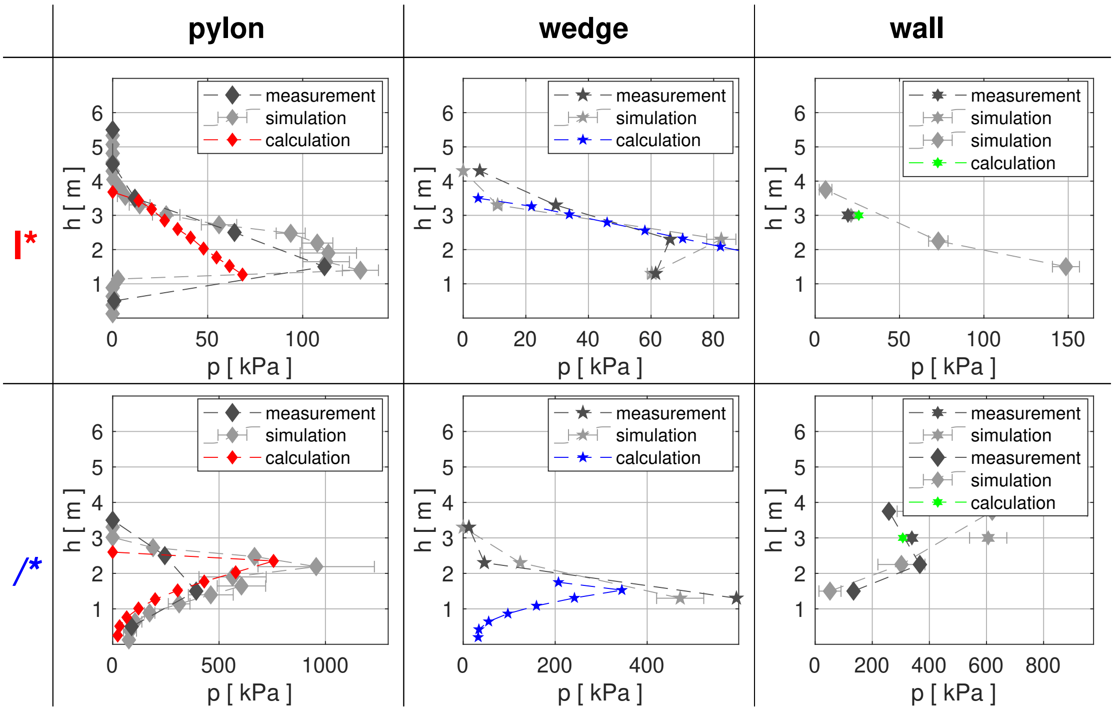

Figure 4.9 – Comparison of calculated (colors) with simulated (light gray) and measured (dark gray) impact pressure profiles on the Vallée de la Sionne measurement obstacles. From left to right the columns show the comparison for the pylon, the wedge and the wall obstacle. The first and second rows show the impact pressure exerted by an avalanche in the warm plug and cold shear flow regime, respectively. The colors and symbols correspond to the illustration in Figure 4.1.

Although we obtain fairly good qualitative agreement between most computed and measured pressure calculations, we observe significant differences between calculations and measurements for two scenarios. The calculated impact pressure is 34% lower than the measured pressure for the pylon impacted by the warm plug flow avalanche (|*) and 42% lower for the wedge impacted by the cold shear flow (/*).

The reason for this difference for the pylon may originate from the choice of C_w based on the assumption that the pylon's overall width $w = 0.6$ m is relevant for the impact pressure (Sovilla et al., 2016). Actually, the sensors at the pylon have a diameter of only 0.1 m and protrude upstream into the flow. Hence, it is difficult to determine which w is relevant when choosing C_w.

For the cold shear flow (/*) impacting the wedge, the error probably originates from our assumption that $C_w = 1$ for all obstacles impacted by inertial flows. However, in Figure 4.4 we observe that the impact pressure on the narrow obstacles with the same width as for the wedge ($w = 0.24$ m) is greater than for the other obstacle widths.

4.8 Discussion

4.8.1 Avalanche impact pressure on obstacles of varying geometry

When comparing the simulated and measured impact pressures in Figure 4.3, we find that the DEM code performs well at computing the pressure differences between obstacles and sensors of varied geometry for different flow regimes. The discrepancies observed in section 4.3 between simulations and measurements can be explained by the complex and time-dependent nature of real-world snow avalanches when interacting with obstacles. Examples of this complexity include deposition processes upstream of the obstacle and the coupling between the avalanche's dense and dilute flow phases.

Consistent with findings from earlier studies (e.g., (Favier et al., 2013), chapter 2), panels a and c in Figure 4.4 show that snow cohesion can strongly amplify the impact pressure, particularly in the gravitational regime. It is worth noting that the impact pressure is not limited to the values simulated in our cohesionless or cohesive flow scenarios. The impact pressure varies with σ_{coh} from the blue curves (|,/) up to the red curves (|,/) for any given obstacle geometry and width. If σ_{coh} is higher than assumed in our scenarios, the pressure values may even exceed the red curves.

As a consequence, computations of p_x are fraught with uncertainty for cohesive avalanches: its value depends crucially on the choice of the cohesive strength σ_{coh}. In the absence of hard information on the link between snow temperature and cohesion, no upper limit of σ_{coh} is known. Values as high as $\sigma_{coh} = 15.6\,\text{kPa}$ have been fitted for an avalanche from Vallée de la Sionne (chapter 2), and even higher values are possible.

Figure 4.4 a and c also show that the simulated impact pressure depends heavily on the obstacle geometry. The rectangular obstacles experience the highest impact pressure, and the impact pressure on the triangular obstacles is on average ~ 45% lower. The pressure on the rectangular obstacles is not only higher than the impact pressure on the triangular obstacles, but also shows more dependence on the flow regime, e.g., if the cohesion increases. Hence, for construction in locations where little is known about the behavior of extreme avalanches, the triangular cross-section has the advantage of experiencing lower absolute pressures and smaller pressure variations in different avalanche scenarios compared with other geometries.

In Figure 4.4, we further observe that the impact pressure exerted by gravitational flows (|,|) decreases similarly for all obstacle cross-sections with increasing w. This finding is consistent with the qualitative behavior observed in many contexts where obstacles or intruders move relative to a surrounding medium at subcritical speeds (e.g., (Haefeli, 1948; Huang and Lee, 2013), chapter 3). In chapter 3 we tentatively proposed that decreasing p_x is caused by increasing shear dilation in the flow around obstacles of increasing w, but the physical origin of this trend has yet to be established with certainty.

For gravitational avalanches, we observe that the impact pressure tends to decrease with increasing w, a feature that is of particular relevance to understanding what may happen in the runout of avalanches with a long return period, in which case dwellings would be the obstacles. Special attention should be paid to the warm plug flow regime. In Vallée de la

Sionne, avalanche flow depth can be as large as 5–7 m (Sovilla et al., 2016). Due to the greater flow height, this would result in pressure $p_x \sim 2.5$ times higher than the impact pressure simulated for the warm plug flow regime (|) in this paper. Some extreme avalanches may exhibit snow cohesion greater than $\sigma_{coh} = 10.0$ kPa, which would lead to an even higher impact pressure. In the gravitational regime the impact pressure is linearly distributed across the flow depth (see Figure 4.5) (Sovilla et al., 2010; Wieghardt, 1975; Albert et al., 1999). As the highest pressures are located at the flow base, reinforcing the foundation and lower part of buildings is recommended, e.g. particularly for buildings at low altitudes, where gravitational avalanche flows are most likely.

This behavior of gravitational avalanches contrasts with what is observed for the inertial flow regime in Figure 4.4 c: the impact pressure decreases for all cross-sections and flow regimes (/,/) for $w \leq 1$ m. For $w > 1$ m the qualitative trend of p_x is somewhat unclear and probably negligible. Figure 4.4 d indicates that overall the influence of w on p_x is weaker in the inertial flow regime (/,/) than in the gravitational flow regime (|,|) in panel b. For narrow obstacles, such as masts of chair lifts or power lines in the avalanche track, the influence of w on p_x is admittedly lower, but the position of such obstacles in the avalanche flow zone makes the probability of an inertial flow regime (/,/) very high. The scenario of inertial avalanches is more problematic because in that regime, the impact pressure increases with increasing velocity (Voellmy, 1955d; Voellmy, 1955c; Voellmy, 1955b; Voellmy, 1955a; Salm and Gubler, 1985) and thus is highest near the flow-free surface. As a consequence, masts experience higher bending moments in this regime than in the plug flow regimes, where the highest pressures are observed at the flow base.

Computation of inertial flows is also fraught with higher uncertainty than for gravitation flows, owing to the pressure dependency on the velocity squared. In our simulations, we generated velocities as high as ~ 40 m/s, which is consistent with the fastest velocities observed for dense flows in Vallée de la Sionne. As for dense flows, the maximum velocity depends on the avalanche track topography, and higher values are likely in other sites (Gubler et al. (1986) cites values as high as 60 m/s).

Figure 4.6 shows that, depending on the flow regime, impact pressure is not distributed homogeneously on the obstacle surface: at the outer edges and at the leading edge in the middle of an obstacle, it is up to ~ 2.5 times higher than the average pressure. Local structure reinforcement can be considered an appropriate countermeasure to this punching effect.

4.8.2 Estimation of the drag coefficient

As the drag coefficient C_D varies smoothly between the subcritical and supercritical regimes, equation (4.1) allows us to go beyond the classic dichotomy between gravitational and inertial avalanches. This possibility is essential for a physics-based estimation of C_D because avalanches can undergo flow regime transitions and multiple flow regimes may coexist in a single avalanche (Köhler et al., 2018b; Faug et al., 2018). With equation (4.1) the impact pressure can be interpreted as the sum of a velocity squared and a flow depth-dependent contribution, as suggested in a number of studies on snow avalanches and other gravity-driven flows (e.g., Faug, 2015; Sovilla et al., 2016; Armanini, 1997). In equation (4.1), the Froude number determines the relative importance of the inertial and gravitational contributions to impact pressure:

- For subcritical flows ($Fr < 1$), the contribution weighted by K, which is related to the gravitational contribution, is the dominant term;
- For supercritical flows ($Fr > 1$), K/Fr^2 becomes smaller whereas C_{geo} becomes larger.

In addition to the Froude number Fr, the parameters C_o, C_w and K have to be determined to calculate C_D (see equation (4.5)). In chapter 3, we showed that for the gravitational regime, impact pressure depends on material compression in the domain of influence around the obstacle, and based on the present study, we can assume that $K = C_o$ (see section 4.6.1), which reduces the number of variables to only two (C_w and C_o).

For the width-dependent coefficient C_w, we use $p_{x,w}/p_{x,w=6\,\mathrm{m}}$ factors derived from our simulations in the gravitational regime (Figure 4.4 b), but this may be a source of error because we neglect a further decrease in p_x for $w > 6$ m. In the absence of knowledge on the physical processes underlying the dependency of p_x on w, we assume $C_w = 1$ in the inertial regime.

To calculate the coefficient C_o, we propose the heuristic equation (4.4), which provides C_o estimates that are similar to the values available in the literature related to snow avalanches and granular flows, where $C_o = 2$, $C_o = 1.5$–1.7, $C_o = 1.5$ are reported for rectangular, cylindrical and triangular geometries, respectively (Favier et al., 2009a; Jóhannesson et al., 2009).

We can indirectly assess the accuracy of the estimates of C_o, C_w and K by comparing the estimated factor $\zeta = C_o^2 C_w = C_o C_w K$ in the gravitational regime to measured values from avalanches with flow heights of up to 5.4 m and velocities of $1-8$ m/s reported by Sovilla et al. (2010). For the comparison, we assume, based on the Vallée de la Sionne pylon's geometry (see Figure 4.7), that the ζ values on the pylon must approximately correspond to the average of the estimated values of the cylindrical and triangular obstacles. For the factor C_w, we consider $w = 0.6$ m to be the relevant width, which corresponds to the width of the pylon (Sovilla et al., 2016). In these configurations, we estimate $\zeta = 5.4$ for the cylindrical obstacle and $\zeta = 3.8$ for the triangular obstacle impacted by a cold plug flow (|). The lower bound of $\zeta = 4.6$ from the Vallée de la Sionne measurement data is consistent with the average of the estimated values. This consistency confirms that the estimation procedure yields reasonable results for the cold plug flow (|). Considering that the pressure increase induced by cohesion in these specific avalanches from Sovilla et al. (2010) may be of a factor of 2.0 to 2.5 (chapter 2), we estimate $\zeta = 7.6$ for the cylindrical obstacle and $\zeta = 13.5$ for the triangular obstacle. The upper bound of $\zeta = 10.4$ from measurements corresponds almost to mean value of the estimated ones. Hence, considering the uncertainty of the choice of the cohesive strength σ_{coh} and the potential dependency of f_{coh} on the geometry, the estimated values are remarkably close to the measured ones.

In order to assess the practical relevance of the proposed method to estimate C_D in real avalanche scenarios (|*,/*), we compare impact pressure calculations based on the C_D estimates to the pressure measured on the Vallée de la Sionne obstacles in Figure 4.9. Although p_x

is underestimated in two cases, due to a uncertain choice of C_w (see section 4.7.2), considering the simplicity of the proposed method we can assert that the calculated pressure profiles show good agreement with the measured profiles. We show that by considering the gravitational and inertial contributions with the proposed method, we can calculate the vertical pressure distributions on the obstacle. As mentioned in section 4.8.1, this may be of interest for the calculation of critical bending moments in inertial avalanches or high pressures at the flow base of gravitational avalanches.

4.9 Conclusions

In the present study, we have shown that our DEM simulations were able to reproduce how a snow avalanche impinges on obstacles of different geometries. Simulated and measured pressures showed good agreement. We simulated impact pressures on obstacles with rectangular, circular and triangular cross-sections in four typical avalanche flow scenarios, and we quantified how the impact pressure varied as a function of the obstacle geometry, width and avalanche flow regime. Furthermore, we documented how impact pressure was distributed on the obstacle surface for different geometries and flow regimes.

Based on previous studies on avalanche impact pressure—through field measurements (Thibert et al., 2013; Sovilla et al., 2010; Sovilla et al., 2016; Thibert et al., 2015) and DEM simulations (chapters 2, 3)—and the new simulations presented in this paper, we have proposed a physics-based method for estimating the drag coefficient C_D involved in the definition of the impact pressure. An innovative point of our study is that the proposed calculation method can be applied to various obstacle geometries by using the specific geometry coefficient C_o.

An important outcome is that C_D varies continuously between the subcritical and supercritical regimes, and thus by using Eqs (1.1) and (4.5) one can compute impact pressure with no assumption about the flow regime. When computing average impact pressures and vertical pressure profiles using the new method for estimating C_D, we obtained good qualitative agreement between impact pressure measurements and simulations for all flow regimes. On average, impact pressure can be predicted with a relative uncertainty lower than $\sim 20\%$.

Further work is needed to elucidate the physical processes underlying the dependence of impact pressure on obstacle width (through the C_w factor). The assumption $K = C_o$ is a coarse approximation based on an earlier study, where we showed that impact pressure depends on material compression inside the domain of influence around the obstacle (chapter 3). Further improvements of our method could be achieved by calibrating the dependence of factor K on the flow regime, e.g., by conducting a study on the behavior of snow subject to large compressive deformations.

Acknowledgments

Michael Kyburz, Betty Sovilla and Christophe Ancey acknowledge the Swiss National Science Foundation for funding the project “Pressure on obstacles induced by granular snow avalanches" (grant no. 200021_169640). Johan Gaume acknowledges financial support from the Swiss National Science Foundation (grant no. PCEFP2_181227).

The code that can be used with the Itasca PFC3D software to reproduce the data presented in this paper is available in the open access data repository Zenodo, which is financed by the Horizon 2020 project OpenAIRE and hosted by CERN. The associated entry can be accessed via Kyburz M., Sovilla, B., Gaume J., & Ancey C. (2021). Physics-based estimates of drag coefficients for the impact pressure calculation of dense snow avalanches. Zenodo. https://doi.org/10.5281/zenodo.4394455.

5 Conclusions

5.1 Context and goal of the thesis

While to date detailed physical knowledge on the avalanche flow and avalanche–obstacle interaction processes is scarce, today's impact pressure calculation procedures mostly rely on empirical relationships. Therefore, even for experienced experts it is challenging to correctly choose suitable empirical constants for the pressure calculation. Field measurements provide essential information on the physics of avalanche flows. Yet the interpretation of the measurements is complex, as they often include a superposition of a multitude of processes. Therefore, in this thesis we use DEM simulations to gain a better understanding of the relevant physical processes governing the avalanche–obstacle interaction and the impact pressure build-up on obstacles. Ultimately, we want to progress from the empirical relationships towards a physics-based framework for the avalanche impact pressure calculation. This framework should enable engineers to better consider the influence of the avalanche flow regime and the obstacle geometry in the calculation of impact pressure.

5.2 DEM model for avalanche–obstacle interaction

In order to achieve the aforementioned goals, we implement a DEM model, which allows us to simulate the interaction of cohesive granular flows and obstacles. Our results show that the DEM model correctly reproduces the flow depth and velocity square proportional impact pressure profiles for subcritical ($Fr < 1$) and supercritical ($Fr > 1$) avalanches, respectively. This indicates that the model captures the most important avalanche–obstacle interaction processes. The model results also shows good quantitative agreement between simulated and measured impact pressures on obstacles of varying geometry and in multiple flow regimes in sections 2.3.1 and 4.3. The good quantitative agreement is notable considering that little information on mechanical snow properties in avalanches is available and the material properties for the simulations are therefore rough estimates, as discussed in sections 2.2.4 and 2.5.

Further limitations of the model are associated with the modelling of the complex mechanical behavior of snow as mentioned in sections 2.4.1 and 2.5, as well as the limited computational resources restricting the size of the simulation domain and particle count as discussed in detail in section 3.4.4.

5.3 Impact pressure — from the physical origin to impact pressure calculations

One of the chief objectives of this thesis is to identify relevant avalanche–obstacle interaction processes to improve the physical understanding of the impact pressure build-up.

In the study on the interaction of cohesive avalanches with the VdlS pylon in chapter 2, we find that the impact pressure can be interpreted as the superposition of the inertial, the frictional and the cohesive pressure contribution. Except for the cohesive contribution in cohesionless flows, all three impact pressure contributions are present in all avalanche flow regimes, but with changing importance for the overall impact pressure depending on the Froude number Fr.

Based on our investigations on the avalanche–obstacle interaction processes and knowledge from the literature, in section 4.6 we propose an impact pressure calculation method, which accounts for all three pressure contributions for avalanche flows in a wide range of Froude numbers.

Below, we discuss each pressure contribution, its physical origin and how it can practically be calculated with the method proposed in chapter 4.

- The **inertial contribution**, which is proportional to velocity square, is predominant at high avalanche velocities where $Fr \gtrsim 10$ and occurs due to the inertial impact of the granular mass on the obstacle. In chapter 3, we show that the inertial contribution can be quantitatively linked to the change in kinetic energy of the granular material inside the MD, which is slowed down by the obstacle. In the inertial regime the MD's shape, which is mostly controlled by Fr (chapter 2), is similar to a bow shock. This shape is observed in many studies on supercritical granular flows around obstacles (e.g., Cui and Gray, 2013; Hauksson et al., 2007). Because the inertial pressure contribution is proportional to velocity squared, it corresponds to the Bernoulli-like term in equation (4.2). The proportionality factor C_{geo} associated with the inertial contribution depends only on the obstacle geometry. We split C_{geo} in two individual factors C_o and C_w. C_o accounts for the influence of the obstacle's cross-section on the impact pressure. Based on the idea that obstacle surfaces at a right angle to the flow direction create more resistance to the flow than surfaces which are more oriented in the flow direction, we propose equation (4.4) to calculate C_o for any convex obstacle surface facing the flow. By applying equation (4.4) to rectangular, circular and triangular cross-section, we find $C_o = 2.0$, $C_o = 1.8$ and $C_o = 1.5$, respectively. These C_o values agree well with values reported in the literature (e.g., Favier et al., 2009a; Jóhannesson et al., 2009). C_w accounts for the influence of the obstacle's width on the impact pressure. We calibrate this coefficient using the simulated impact pressure in Figure 4.4 for obstacles with widths between 0.24 m and 6.0 m. In this range, C_w is as high as ~ 2 for obstacles with widths of 0.24 m in subcritical avalanche flows and is lower for obstacles of increasing width or in supercritical flows.

- The **frictional contribution** is mostly significant in the gravitational regime. In order to flow around the obstacle, the particles in a granular flow rearrange continuously leading to the perpetual formation and destruction of force chains (Geng and Behringer, 2005). The MD is formed by force chains originating from the impact surface of the obstacle extending upstream into the flow, leading to a rounded shape of the MD in subcritical flows where the frictional contribution is of importance. Compared to the surrounding flow, which is not affected by the obstacle's presence, the force chains in the MD are markedly stronger. The strong force chains are a consequence of the particles jamming around the obstacle, which causes the granular material to compress inside the MD. Simulating axial compression tests (chapter 3), we show that the material compression inside the MD can be linked quantitatively to the impact pressure on the obstacle in the gravitational regime, confirming the findings of Chehata et al. (2003).
  Because the frictional contribution is most relevant for avalanches with low Fr (section 2.3.2), this contribution is related to the regime-dependent term in equation (4.2), which is weighted by $1/Fr^2$. Consequently, this term is dependent on the flow depth and is proportional to $C_o^2 C_w / Fr^2$. Similarly to the inertial contribution $C_o C_w$ accounts for the influence of the obstacle geometry on the impact pressure. The additional factor C_o in the regime-dependent term of equation (4.5) reflects the effect of the particle jamming in the MD in subcritical flows. The proportionality with C_o^2 is also consistent with the results from compression tests (section 3.2.4), where we find that the stress in the granular material scales approximately with the particle interpenetration squared, which is related to the particle jamming.

- The **cohesive contribution**, which is mostly significant in the gravitational regime, originates from the non-zero tensile and shear strength between neighbouring particles, increasing the persistence of force chains and densifying the contact network (Favier et al., 2013; Rognon et al., 2008b). Cohesion therefore reduces the material's ability to flow around the obstacle, causing more particle jamming and greater material compression inside the MD compared to the cohesionless case. The impact pressure is even further increased by the enhanced force transmission in cohesive contacts due to the presence of the cohesive bond. Compared to the cohesionless case the increased particle jamming and enhanced force transmission in cohesive flows lead to an increase in impact pressure by factors up to 3.7 depending on the obstacle geometry (section 3.3.1) and cohesive strength (section 2.3.2).

In chapter 2, we find a scaling, which allows us to quantify the influence of cohesion on the impact pressure and thus to calculate the impact pressure of a cohesive flow on the VdlS pylon for a large range of Bo and Fr. The scaling is based on the concept of the competition of collisional forces, which depend on the flow velocity and thus Fr, and the cohesive forces between the particles expressed by the Bond number Bo. In order to obtain the impact pressure exerted by a cohesive flow, the impact pressure exerted by a corresponding cohesionless flow can be multiplied with a factor based on the ratio of the Bond number and the Froude number. Hence, the calculation of the impact pressure exerted by a cohesive flow includes considering the inertial and frictional contributions as mentioned above, as well as calculating the pressure increase factor f_{coh} based on the Froude and the Bond number, e.g. by using equation (4.7).
Qualitatively, the scaling is in agreement with previous studies reporting that the effect of cohesion mostly becomes apparent above a threshold cohesion value and is similar to the cohesionless case otherwise (e.g., Favier et al., 2013; Macaulay and Rognon, 2021; Rognon et al., 2006).
Although, we assume that the scaling may depend on the obstacle geometry, we also apply it to other obstacles with different geometries. In the tested cases in chapters 3 and 4, the impact pressure increase estimated with the scaling agrees well with simulated and measured impact pressure exerted by cohesive flows. We therefore assume that also for other geometries the pressure amplifications due to cohesion are in the same order of magnitude as for the VdlS pylon. Hence, while there may be deviations from the amplification estimated with the scaling for the VdlS pylon due to differing geometries, we assume this error is small compared to the uncertainty of the estimated cohesive strength. Moreover, if a specific geometry is of particular interest the study in chapter 2 could be conducted for different geometries.

5.4 Influence of the flow regime and the obstacle geometry on the impact pressure

As our numerical setup allows us to independently control the granular flow characteristics and the obstacle geometry, we are able to methodically asses the influence of various parameters, such as the cohesion, the flow velocity and height, as well as the obstacle geometry, on the impact pressure.
In agreement with the literature, we observe that impact pressure is proportional to velocity squared in supercritical flows with Froude numbers close to or greater than 10 (e.g., Voellmy, 1955d; Voellmy, 1955c; Voellmy, 1955b; Voellmy, 1955a; Thibert et al., 2008; Faug, 2015). Physically this proportionality can be explained by the dominance of the inertial impact pressure contribution in this regime, in which the impact pressure originates from the deceleration of the impacting granular mass mobilized by the obstacle (section 3.4.3).
In subcritical avalanches ($Fr < 1$), we confirm that the impact pressure is proportional to

the depth below the free flow surface similar to in granular flows (e.g., Sovilla et al., 2010; Wieghardt, 1975; Albert et al., 1999). In this regime the impact pressure is dominated by the frictional and the cohesive pressure contributions. As described in the previous section 5.3, these contributions originate from particle jamming in the MD, which increases with increasing depth below the surface because of the weight of the material above and with increasing cohesion. In intermediate flows with Fr close to unity, all three pressure contributions may be relevant for the impact pressure. Therefore, in these regimes the impact pressure may consist of a superposition of the hydrostatic-like and Bernoulli-like pressure distributions.

By analyzing the pressure distribution in the horizontal direction in section 4.5, we find that local impact pressure concentrations may be as high as ~ 2 times the average pressure. While the pressure concentrations on the rectangular obstacles are mostly located at the outer edges, the pressure concentrations on the cylindrical obstacles are in the middle, where the flow hits the obstacle at a right angle. For the triangular obstacles, concentrations on the outer edges or the leading edge may be observed depending on the flow regime and the snow properties of the avalanche. In order to counteract damages caused by pressure concentrations, the obstacles' structure may be reinforced locally.

The simulation outcomes also confirm previous studies, that out of three typical obstacle geometries the drag force on a rectangular obstacle is highest followed by drag on a cylindrical and a triangular obstacle (e.g., Favier et al., 2009a; Jóhannesson et al., 2009). We find that it is the particle jamming inside the MD, which is higher for obstacles offering more resistance to the flow e.g. the rectangular obstacles, causing a higher impact pressure than e.g. on triangular obstacles offering less resistance (section 3.4.1).

Furthermore, we quantify the influence of obstacle width on the impact pressure (section 4.4). In subcritical flows we find that the impact pressure decreases on obstacles of increasing width regardless of the cross-section. While this trend has first been qualitatively observed and documented decades ago (e.g., Haefeli, 1948; Margreth, 2007), to our knowledge there is no comprehensive study elucidating the physical origin or giving quantitative estimates of this size effect. Although strong evidence is still lacking, we find indications that in subcritical flows the particle interpenetration in the MD is lower for wide obstacles because of the higher shearing of the material (section 3.4.1). In supercritical flows, however, the impact pressure decrease is not monotonic for all obstacle widths and cohesion values. This indicates that further research is needed to gain a comprehensive understanding of the dependency of the pressure on the obstacle width.

In summary, in the present thesis we successfully identify the most relevant avalanche–obstacle interaction processes (chapters 2 and 3), quantify the link between the MD and the impact pressure (chapter 3) and finally bridge the gap to the physics-based calculation of impact pressures on obstacles (chapter 4). Hence, while further research is needed to overcome our model's shortcomings and limitations (chapter 6), we are convinced that with the present thesis we make a considerable step forward in progressing from empirical towards physics-based impact pressure calculation.

6 Outlook

6.1 Modelling avalanche-obstacle interaction with DEM

The DEM model presented in this thesis allows us to conduct an in-depth investigation on the interaction of granular flows and obstacles. Below, we identify limitations of the model, which could be addressed in the future to improve the model's accuracy and performance for further studies:

- **Contact model:** The contact model used in our studies is a standard contact model implemented in the Itasca PFC3D software (Itasca Consulting Group, Inc., 2014) for cohesive geomaterials. Although our results show that the model is able to reproduce the fundamental behavior of snow in avalanches, we identify two deficiencies, which are not well represented in our model compared to real snow behavior.
  First, the compressive behavior of the material, which is highly plastic in real snow, is not well calibrated in our contact model (see e.g. section 2.4.1). Second, while our contact model allows for instantaneous cohesive bonding whenever two particles become in contact, the sintering process in snow usually depends on the contact time and force (e.g., Gubler, 1978; Szabo and Schneebeli, 2007). These two deficiencies could be addressed in the future by improving the parallel-bond model to account for the compressive behavior and the time dependence of the bond strength, as well as by calibrating the model with measurement data of mechanical snow properties.

- **Fluid coupling:** An important limitation of the model is the restriction to dense flows. This limitation could be overcome by implementing a fluid coupling between the solid particles and the interstitial air. As the suspended particles in the dilute phase of the avalanche are usually smaller than the snow aggregations in the dense flow, this also entails to reduce the size of the discrete elements and thus increasing the particle count as well as the computational effort.

- **Computational effort:** Despite several measures to reduce the computational effort of our simulations, with the current DEM setup we operate at the limit of our computational resources. Already the simulations of the isolated volume around the obstacle are very time consuming. A simulation of a large scale flow on an inclined plane would not be feasible.
  Indeed, a more efficient numerical method should be used in the future to simulate the avalanche from release to runout, including the avalanche track and the interaction with obstacles. In this case the challenge will be to correctly capture the granular nature of dense avalanches with a numerical method other than DEM. One promising numerical framework to overcome the issue of the computational effort is the material point method (MPM). This method was already successfully used for modelling snow avalanches (e.g., Gaume et al., 2018b; Li et al., 2020) and is able to reproduce the impact dynamics on obstacles similarly to DEM (Ceccato et al., 2018).
  An alternative could also be to use a coupling between a 3D continuum solver for the slope scale dynamics and DEM simulations in the vicinity of the obstacle. With this approach, however, one must still consider the DEM's limitation for large obstacles which require large simulation domains.

6.2 Determining and calibrating the crucial parameter of cohesion

In our study cohesion is one of the most important quantities influencing the simulated impact pressure. In avalanche scenarios with cold snow, where we expect the snow cohesion to be very low, the impact pressure simulated using $\sigma_{coh} = 0.0\,\text{kPa}$ agrees well with measured pressures (e.g., Figure 4.3). In warm avalanches, where cohesion heavily influences the flow behavior and impact pressure, it is important to accurately calibrate and estimate the cohesion in the DEM model. Thus, an important question for the dimensioning of structures is the maximum cohesive strength of snow in extreme avalanche scenarios. It would therefore be important to explore the physical range of mechanical snow properties in the avalanche e.g. on a laboratory scale similarly to Steinkogler et al. (2015) or Fischer et al. (2018), and to accurately calibrate the cohesion in the DEM model.

6.3 Existence and properties of the mobilized domain

In chapter 3 we highlight the importance of the concept of the MD by quantitatively linking the material properties inside the domain to the impact pressure in the gravitational regime. First, it would be enlightening to confirm the MD's existence in the field. To verify the domain's existence, in 2017 we installed a high-speed camera at the VdlS measurement pylon capturing the dense flow surface at a frequency of 140 Hz with a field of view of $\sim 12 \times 12\,\text{m}$ on the ground around the pylon. As part of ongoing research, we aim to identify the MD based on the velocity field at the flow surface recorded by the camera using a velocimetry technique.

Moreover, in the event of a field experiment with an artificially released avalanche, in-situ shear strength and density measurements of the avalanche deposit could be performed in the vicinity of obstacles. However, such manual field measurements can only give indications of the mechanical snow properties inside the MD and it's extent in the instant when the avalanche stops.

Second, the DEM simulations indicate that the material compression inside the MD is closely related to the impact pressure. In the future it would therefore be of importance to better quantify the link between large compressive snow deformation and the material stress state in a relevant range of temperatures, e.g. -10 – 0 °C. As mentioned in section 4.9, these tests would also assist the practical pressure calculation, as the parameter K could be calibrated using the results of the compression tests.

6.4 Relevance of the thesis results for practical avalanche engineering

In the present thesis, we propose a new method to calculate the impact pressure distributions on obstacles of different shape and dimension and for different avalanche flow regimes. The inputs for the pressure calculation, which include the snow properties, the flow velocity and the flow depth of the avalanche impacting an obstacle, have to be known or estimated. Hence, the presented calculation method may well be applied when the avalanche characteristics are known or can be estimated, e.g. in the case of back-calculations. For avalanche tracks close to historic settlements and important traffic routes, estimates of the dynamic avalanche characteristics may be available from observations. In remote areas numerical simulations are often the only way to obtain estimates of the avalanche characteristics. However, to date simulating the avalanche flow dynamics on the slope scale is still a challenge, as this includes the modeling of highly complex processes on large scales. Moreover, the prediction of the release area and volume of the avalanche, which is usually based on statistical analyses of the return periods, may be fraught with considerable uncertainties in scarcely monitored areas and due to changing snow conditions as a consequence of climate change (Lazar and Williams, 2008; Castebrunet et al., 2014). While the presented calculation method is independent from how the avalanche characteristics are obtained, to make predictive impact pressure calculations further advances need to be made in quantitatively predicting the avalanche release and flow dynamics.

A Supplementary material for chapter 2

A.1 Formulation of the Discrete Element Method

To study the interaction of a cohesive granular flow, such as snow avalanches, and structures we developed a new model based on the Discrete Element Method (DEM). For this we use the Itasca PFC 3D software, which implements the soft-contact algorithm, first described by Cundall and Strack (1979). In the Discrete Element Method the material and flow properties of the simulated matter are governed by the properties of the elements and the contact law. In our model we have two types of elements: the discrete elements are spheres called *balls*, and the *walls*. In contrast to the balls, the walls do not react to external forces. The walls are either static or move at a user-defined speed.

At each time step the displacements of the balls are calculated from their current state and the sum of the contact forces F_c and moments M_c according to Newton's second law of motion (equation A.1 and A.2):

$$m \cdot a = \sum F_c \tag{A.1}$$

$$J \cdot \dot{\omega} = \sum M_c \tag{A.2}$$

where a is the translatory acceleration, m is the ball mass, J is the moment of inertia and $\dot{\omega}$ is the angular acceleration.

After the displacement is applied, the new position of each element is evaluated. The resulting relative positions of the elements are the basis to calculate the contact forces F_c from the contact law. In our study we use the *parallel bond* contact model, which is used in previous studies for modelling snow (e.g. by Gaume et al. (2015b)). In this contact law a linear component acts in parallel to a solid bond connecting two balls. The linear component consists of a linear elastic spring and a dashpot for the normal force. The tangential force is modelled with of a linear elastic spring and a Coulombian friction limit. The bond, which mimics the cohesive sintering of snow, is modelled as a solid connection between the balls. Hence, the bond can sustain not only normal and tangential forces but also bending and torsional moments. The cross-section of the bond is constant and is equal to the cross-section area A of the balls:

$$A = r_p^2 \cdot \pi \tag{A.3}$$

where r_p is the ball radius.

In our implementation, the bond forms whenever a new physical contact between two elements, balls or walls, occurs. Figure A.1 a shows two elements and the components of the contact model. Figure A.1 b shows a typical life cycle of a contact between two balls.

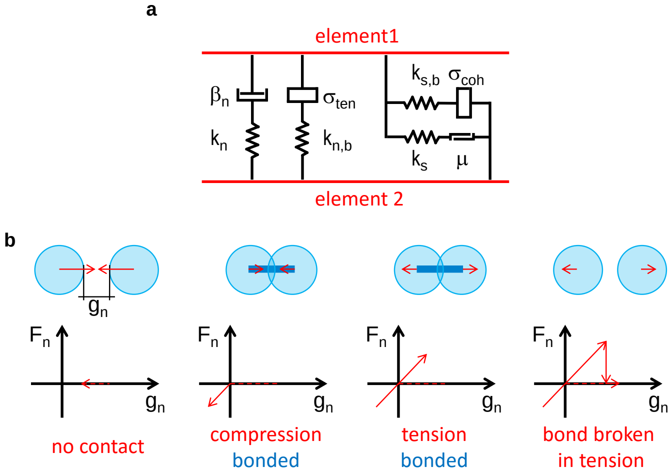

Figure A.1 – Panel a shows a schematic view of the *parallel bond model* between two elements. Panel b shows a typical life cycle of two colliding elements.

The elastic behavior of the discrete elements is characterized by the Young's modulus E_{linear}. The code calculates the normal (k_n) and shear (k_s) stiffness according to equations A.4 and A.5.

$$k_n = A \cdot E_{linear} / L \tag{A.4}$$

$$k_s = k_n / k_{linear} \tag{A.5}$$

where L is distance between centroids of the elements.

Similarly, also for the bond the Young's modulus E_{bond} is converted to a normal and shear stiffness $k_{n,b}$ and $k_{s,b}$, respectively.

The detailed parameters used for the particle properties and the contact law are summarized in Table A.1.

Table A.1 – Parameters for the DEM simulations in the gravitational and inertial regime

Parameter	Symbol	Unit	Value
Ball attributes			
Density	ρ_p	kg/m^3	500
Normal restitution coefficient	e	–	0.05
Ball radius	r_p	mm	40 ± 8
Ball-ball contact properties			
Young's modulus linear part	E_{linear}	Pa	10^5
Linear normal-to-shear stiffness ratio	k_{linear}	–	2.0
Friction coefficient	μ	–	0.5
Normal critical damping ratio	β_n	–	0.0
Shear critical damping ratio	β_s	–	0.0
Young's modulus parallel bond	E_{bond}	Pa	$E_{bond} = E_{linear}$
Bond normal-to-shear stiffness ratio	k_{bond}	–	$k_{bond} = k_{linear}$
Bond cohesive strength	σ_{coh}	Pa	$0.0 - 2.0 \cdot 10^4$
Bond tensile strength	σ_{ten}	Pa	$\sigma_{ten} = \sigma_{coh}$
Ball-facet contact properties			
Young's modulus linear part	E_{linear}	Pa	10^6
Linear normal-to-shear stiffness ratio	k_{linear}	–	2.0
Friction coefficient	μ	–	0.1
Normal critical damping ratio	β_n	–	0.0
Shear critical damping ratio	β_s	–	0.0
Young's modulus parallel bond	E_{bond}	Pa	$E_{bond} = E_{linear}$
Bond normal-to-shear stiffness ratio	k_{bond}	–	$k_{bond} = k_{linear}$
Bond cohesive strength	σ_{coh}	Pa	0.0
Bond tensile strength	σ_{ten}	Pa	$\sigma_{ten} = \sigma_{coh}$

In the parallel bond model, the contact force F_c is the sum of the linear (F^l), the dashpot (F^d) and the bond (F^b) contribution (equation A.6).

$$F_c = F^l + F^d + F^b \tag{A.6}$$

Because we set $\beta_n = \beta_s = 0$ at all times (Table A.1), the dashpot force is also zero ($F^d = 0$). The linear force F^l can be divided into a normal (F_n^l) and a shear (F_s^l) contribution (equation A.7). The same is done for the bond force F^b, where F_n^b is the normal and F_s^b is the shear contribution (equation A.8).

$$F^l = F_n^l + F_s^l \tag{A.7}$$

$$F^b = -F_n^b \hat{n_c} + F_s^b \tag{A.8}$$

where $\hat{n_c}$ is the direction normal to the contact-plane.

The normal force of the linear part F_n^l is calculated using the normal stiffness k_n and the gap g_n between two elements (equation A.9). For the linear shear contribution F_s^l, the Coulombian friction is implemented according to equations A.10 and A.11.

$$F_n^l = \begin{cases} g_n \cdot k_n & g_n < 0\,(with overlap) \\ 0 & otherwise \end{cases} \tag{A.9}$$

$$F_s^l = \begin{cases} F_s^* & \|F_s^*\| \le -\mu F_n^l \\ -\mu F_n^l \cdot (F_s^* / \|F_s^*\|) & otherwise \end{cases} \tag{A.10}$$

$$F_s^* = (F_s^l)_0 - k_s \cdot \Delta\delta_s \tag{A.11}$$

where $\|\cdot\|$ denotes the vector magnitude, $(\cdot)_0$ the value of a quantity of the last time step and $\Delta\delta_s$ the relative shear-displacement increment of a time step.

Starting from the formation of the bond, the normal F_n^b and shear F_s^b bond force contributions are computed incrementally using the bond normal $k_{n,b}$ and bond shear $k_{n,s}$ stiffness (equations A.12 and A.13), respectively.

$$F_n^b = (F_n^b)_0 + k_{n,b} A \Delta\delta_n \tag{A.12}$$

$$F_s^b = (F_s^b)_0 - k_{s,b} A \Delta\delta_s \tag{A.13}$$

where $\Delta\delta_n$ the relative normal-displacement increment of a time step.

The only moment M_c acting at the contact is the moment emerging from the parallel bond M^b (equation A.14). M^b is the sum of a torsional (M_t^b) and a bending moment (M_b^b) contribution (equation A.15) (Crandall et al., 1978).

$$M_c = M^b \tag{A.14}$$

$$M^b = M_t^b \hat{n}_c + M_b^b \tag{A.15}$$

For more precise information on the implementation refer to the Itasca PFC 3D documentation (Itasca Consulting Group, Inc., 2014).

A.2 Model setup

Our simulation setup consists of the following elements visualized also in Figure A.2:

1. Balls (blue circles in Figure A.2), mimicking the avalanche granules.
2. Horizontal wall (orange line in Figure A.2), acting as a ground or sliding surface of the avalanche.
3. Pushing walls (red boxes in Figure A.2), used to enforce the velocity profile of the flow.
4. Obstacle (green structure in Figure A.2).

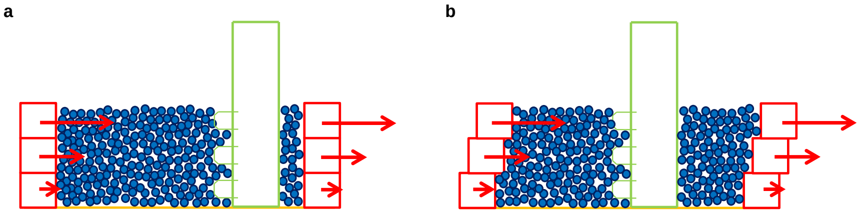

Figure A.2 – Initial (panel a) and final state (panel b) of a simulation imposing a shear velocity profile. The arrows (red) indicate the imposed velocity of the pushing walls. The obstacle (green), where the pressure is evaluated, is partially immersed in the discrete elements (blue) mimicking the avalanche.

In streamwise direction the balls are confined within the pushing walls. In the transverse direction we define a periodic boundary condition.

The obstacle in the simulation has the same cross-section and sensor geometry as the steel pylon in VdlS. The only significant difference between the real pylon and the modeled structure is that the pressure gauges in the model are distributed with smaller vertical gaps than in reality in order to achieve a higher spatial resolution of the pressure profile. The simulated (panel a) and the real (panel b) structure are compared in Figure A.3.

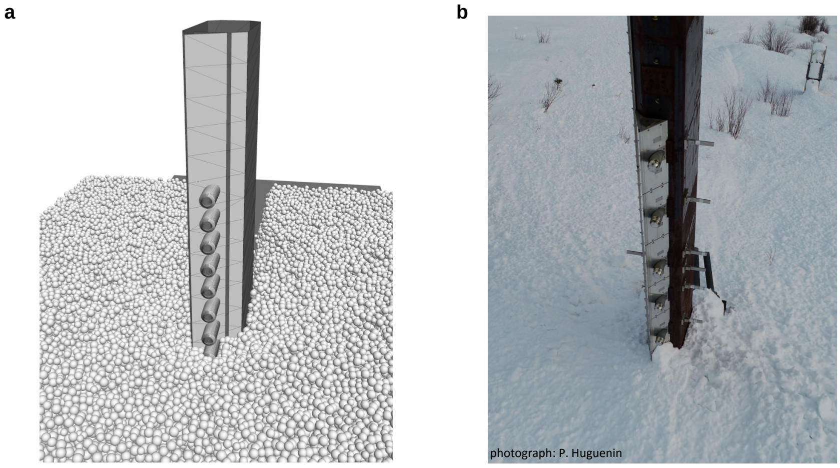

Figure A.3 – Simulated obstacle (panel a) and pylon at the VdlS test site (panel b).

A.3 Simulation procedure

The simulation starts by imposing a given velocity to the pushing walls and the balls. This velocity is chosen according to the velocity profile we want to reproduce (e.g. shear flow profile, Figure A.2 a). During the course of the simulation the walls maintain their fixed velocity. The balls, however, are free to move according to the laws of motion and the forces at the contact points with other elements (see section A.1). Hence, the velocity, flow direction and contact forces of the balls may alter due to the presence of the obstacle. Initially the balls are not in contact with the obstacle. The contact is established shortly after the start of the simulation, when the balls are pushed past the obstacle. Hence, the flow around the obstacle evolves during the course of the simulation and finally reaches a steady state. In order to avoid a distortion of the result due to the pushing walls, the simulation is stopped before the walls are too close to the obstacle or the influenced zone in the flow. Hence, in the current configuration we stop the simulation when the closest wall is half way of the domain length in streamwise direction from the obstacle (Figure A.2 b). This limits the simulated time of the particles flowing and interacting with the obstacle. Depending on the maximum velocity of the pushing walls, the simulated time is between 0.025 s and 1.0 s. In this period we obtain time resolved impact pressures and velocities at the pylon from our simulations. We find that in most cases the flow around the pylon reaches a steady state after about 25 % of the simulated time. Hence, to obtain the impact pressure values used in Figures 2 - 4 and 8, we average the impact pressure values of the latter 75 % of the simulations. This is depicted for sample simulations of a plug flow at 4 m/s and a shear flow at 15 m/s in Figure A.4 panel a and b, respectively.

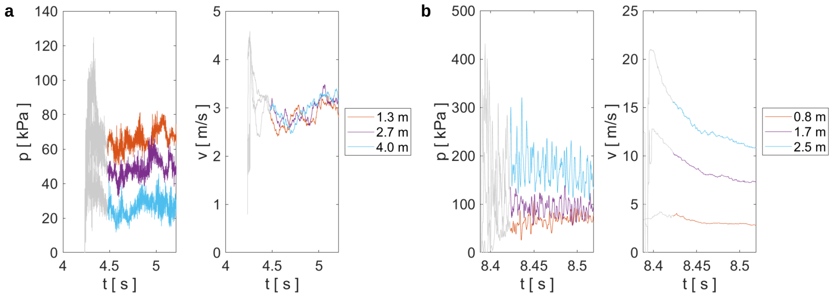

Figure A.4 – Temporal evolution of the impact pressure and velocity at the pylon during a simulation at different heights in the flow. Panel a shows a plug flow moving at 4 m/s and panel b a shear flow moving at 15 m/s. The colored part of each line visualizes the part of the time series averaged to obtain the impact pressure value used in the results.

A sensitivity analysis on this threshold shows that changing the averaging range from 10 % to 100% of the time resolved signal results in a relative change of 6 % of the absolute impact pressure values. Figure A.5 depicts the impact pressure values obtained by averaging the last 10 % and the entire time series in panel a and b, respectively. Thus, the results of our analysis do not change as a function of the averaging time.

A.4 Clarification of the quantities used for the analyses

In this section we want to clarify how the quantities used for the analyses are exactly obtained from the model.

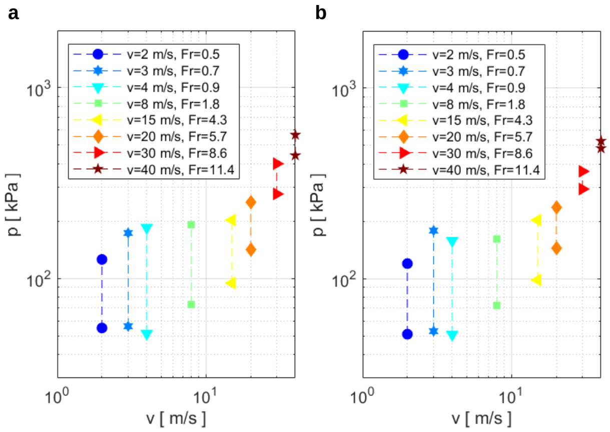

Figure A.5 – Resulting impact pressures (graph similar to Figure 4 a) from averaging the last 10 % and 100 % of the simulated pressure time series in panel a and b, respectively.

A.4.1 Vertical location

To compare simulations, we always use a representative value of contact force, velocity at the pylon, imposed velocity, confining pressure and impact pressure, which corresponds to the value at mid flow depth. Because the imposed shear velocity profile is linearly increasing and the imposed plug flow is constant, the velocities in the middle correspond also to the depth averaged velocities. The full vertical profiles of impact pressure and velocity at the pylon are only used for the comparisons of simulations and measurements in Figures 2, 5 and 8.

A.4.2 Velocity

In the scope of this article we distinguish between the imposed velocity far from the obstacle and the velocity measured at the obstacle (Figure 1 c). The flow regime far away governs the impact pressure at the obstacle. This is also true in fluid dynamics, where drag forces and boundary layer calculations are performed using the freestream velocity (e.g. calculation of the Reynolds number). Hence, we also consider the freestream velocity rather than the velocity at the pylon to relate to the load on the structure. The velocity at the structure in the simulation is solely used to be matched to the velocity measured in the real experiments at the VdlS pylon (Figure 2 and 3). This serves as a boundary condition to compare the corresponding impact pressure values from measurements and simulations. The velocity is measured in practice as reported by Kern et al. (2009). In the numerical model we evaluate the velocity at the same location on the structure as in the field experiments (Figure 1 c). For this we average the velocity of the balls, whose centroids are at most one particle diameter away from the surface.

A.4.3 Impact pressure

If not mentioned otherwise, in the present study we use the term *pressure* to refer to the impact pressure exerted by the granular flow on the obstacle. The impact pressure p on the structure is determined according to equation A.16. We sum up the face normal contribution of the contact forces of all discrete elements in contact with the sensor measurement surface and divide this force value by the area of this surface A_{sensor}:

$$p = \frac{1}{A_{sensor}} \sum_{N_c} \vec{F}_c \hat{n}_c \tag{A.16}$$

where N_c is the number of contacts.

The pressure sensing surface is at the tip of cylindrical pressure gauges protruding into the flow (Figure 1 c, Figure A.3, or Sovilla et al. (2016)). The sampling of the force values in the simulation is done at 7.5 kHz. This is the same frequency as the sampling rate of the real pressure sensors in VdlS.

A.4.4 Confining pressure

In order to use the dimensionless Bond number Bo, we also calculate the confining pressure. As described in section 2.2.4 we use the vertical component of the local stress tensor as the confining pressure $p_{conf} \equiv \sigma_{zz}$. In contrast to the impact pressure, the confining pressure is a quantity measured in the flow. In order to determine the stress value we use an average of the contact stresses of all contacts within a sphere of radius of 10 times the ball radius. The average stress in the volume V of the sphere is computed as (Christoffersen et al., 1981):

$$\vec{\sigma} = -\frac{1}{V} \sum_{N_c} \vec{F}_c \otimes \vec{L}_c \tag{A.17}$$

where $\vec{\sigma}$ is the stress tensor, V the measurement sphere volume, $\otimes$ the outer product and $\vec{L}_c$ the branch vector joining the centroids of two elements in contact.

A.4.5 Contact forces and mobilized domain

With a ball count of more than 800’000 and 3.5 million contacts in one simulation, the analysis of the contact forces and hence, the mobilized domain, is far more elaborate than determining the impact pressure. Therefore, we perform the analysis of the whole flow field only at the last time step of every simulation. Hence, the analyses in Figures 5 - 7 (except panels c, f, i in

Figure 5, which contain time averaged impact pressure values as described in section A.4.3) are snapshots of the flow around the obstacle in the last time step. However, as we mentioned earlier, we are convinced, that at this point the flow around the obstacle, and hence the mobilized domain, has sufficiently evolved and reached a quasi steady state.

B Supplementary material for chapter 3

B.1 Temporal evolution of the impact pressure during simulations

In section 2.1 of the main article we state that the reported impact pressure values are the temporal average of the pressure on the obstacle during the second simulation phase. Figure B.1 shows the temporal evolution of the impact pressure during simulations of a cohesionless flow (a–c) and a cohesive flow (d–f) for the examples with width $w = 1$ m for all cross-sections.

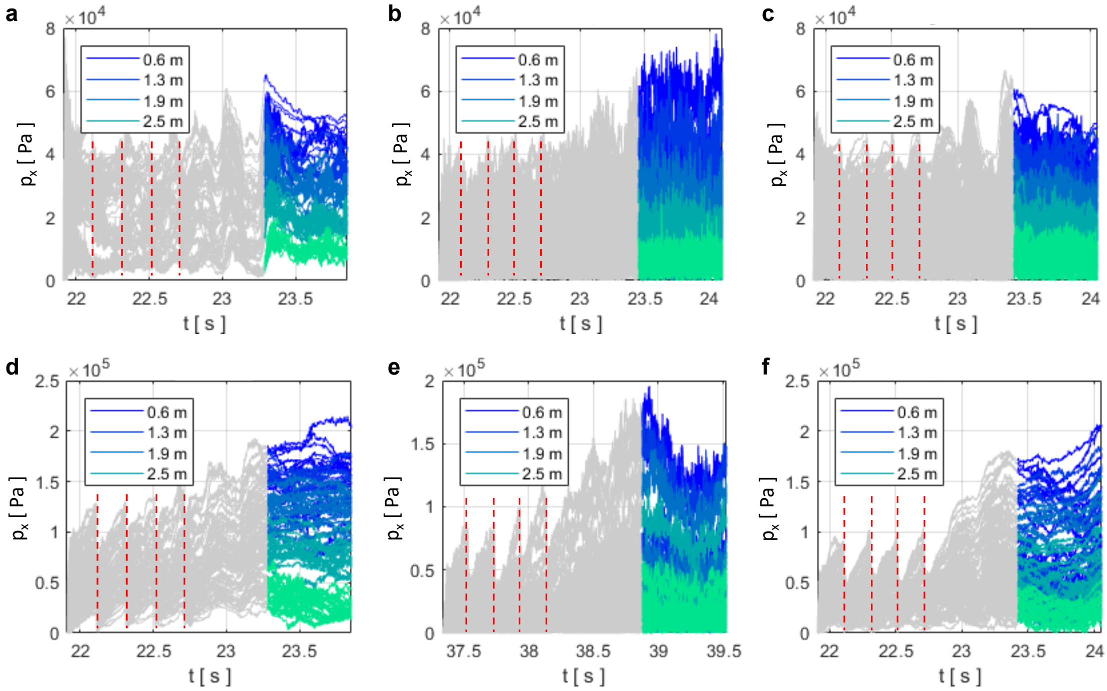

Figure B.1 – Time series of the simulated pressure in various positions on the obstacle (no distinction made) in the cohesionless (top row) and the cohesive (bottom row) scenario for an obstacle with a rectangular (left), circular (middle) or triangular (right) cross-section.

In the impact pressure graphs in Figure B.1 above, we can identify the fluctuations due to the generation of new particles in the first simulation phase (marked with red dashed lines). The colored parts of the graphs in the second simulation phase (see main article section 2.1) are averaged to obtain the impact pressure values presented in the article. More specifically, we average only the last 30 % of the whole time series, including the first and the second phase, because we expect this time segment to be the closest to the steady state impact pressure.

B.2 Sensitivity analysis of axial compression tests

A large portion of the main article's results depend on the relationship between the relative particle interpenetration Δ and the normal stress σ_n obtained from compression tests (section 2.4). To assess the robustness of the compression tests' results, we run a number of compression tests varying the sample size s_0, the compression speed and restitution coefficient e_r.

- **Sample size:** We vary the size of the compression sample in the range of our obstacle widths $0.24\ \mathrm{m} \leq w \leq 6\ \mathrm{m}$. Figure B.2 a shows that, relative to the largest sample with $s_0 = 6$ m in the cohesionless case, the normal stress σ_n deviates by 25.3 %, 8.2 %, 7.3 % and 2.9 % for the samples with s_0 of 0.24 m, 0.6 m, 1.0 m and 3.0 m, respectively. Similarly, the results of the compression tests with the cohesive material also converge towards the results obtained with $s_0 = 6$ m.

- **Compression speed:** The compression test reported in the main manuscript corresponds to a *quasi-static* compression test. In these tests we compress the sample by a small increment and run the simulation until the material reaches a mechanical equilibrium criterion. This process is repeated until the target strain is reached. In the *dynamic* test we compress the sample by moving the upper clump (see Figure 3 in the main manuscript) at a constant speed of 3 m/s. This corresponds to the approach speed $v = 3$ m/s of the flow used in our simulations.
  Hence, to assess the influence of the strain rate, in Figure B.2 b we compare the stresses of a quasi-static and a dynamic compression test. The results of the *quasi-static* and *dynamic* compression tests differ by 3.4 % and 0.5 % in the cohesionless and the cohesive case, respectively.

- **Restitution coefficient:** In this study we choose e_r in accordance with our earlier study Kyburz et al., 2020, where we choose a low damping $e_r = 0.05$ (section 2.3). In order to estimate the influence of this choice on the resulting impact pressure, we perform compression tests of the granular material, as described in the article and varying e_r of the cohesionless material, where we expect a stronger influence of e_r. Figure B.2 c below shows that we do not expect significant differences in the impact pressure even if we greatly increase e_r to $e_r = 0.5$, as the stresses within the material, on the wall and on the clump, are practically identical. The differences between the two cases are < 0.5 % and are therefore negligible.

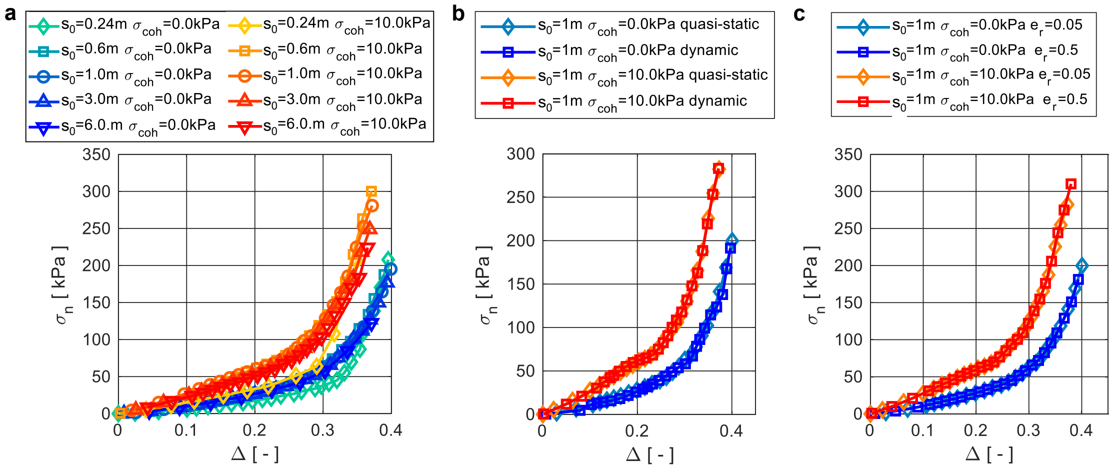

Figure B.2 – Sensitivity analysis for the axial compression tests with varying sample size (a), compression speed (b) and restitution coefficient (c).

B.3 Definition of the mobilized domain (MD)

As described in the main article, we use a percentile threshold of the contact forces between the particles to systematically identify the mobilized domain (MD). Even in an undisturbed granular bed the contact forces increase analogous to a hydrostatic pressure for increasing depth from the free surface. Hence, we calculate the threshold for every height increment of the discretized flow field in the vertical direction individually.

The percentile threshold we use for the MD identification is only consistent if the ratio of particles inside and outside the MD is similar for all simulations. However, in our simulations we vary the obstacle size ($0.24\ \mathrm{m} \leq w \leq 6\ \mathrm{m}$) and use two different flow domain widths ($D_y = 11$ m, $D_y = 22$ m). This leads to different proportions of particles inside and outside of the MD. In order to improve the consistency of the MD threshold values between all simulations, we must keep the ratio between particles inside and outside of the MD approximately constant. Therefore, for the MD threshold calculation in simulations where $w < 6$ m we consider only a smaller part of the flow domain proportional to w, which scales with MD size. We visualize the flow domain and the domain considered for the MD threshold calculation schematically in a horizontal section in Figure B.3. The considered domain is limited by the simulation of the 6 m-wide cylindrical obstacle, where the simulation domain around the obstacle is the smallest compared with the extent of the obstacle itself. For the identification of the MD itself, the threshold value is applied to the whole flow domain.

Moreover, we use a Gaussian filter to smooth the contours of the MD.

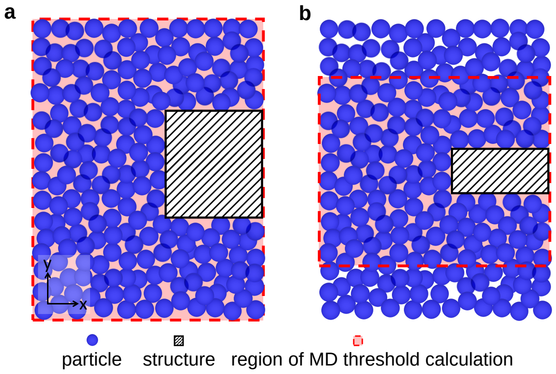

Figure B.3 – Schematic drawing of a horizontal cross-section through the flow domain for a wide (a) obstacle (black and white hatched area) and a narrow (b) obstacle. The domain considered for the MD threshold calculation is shaded in red and outlined with a red dashed line. The flow domain, the particles and the obstacle are not to scale.

B.4 Sensitivity of the results on the MD threshold value

In this study the definition of the MD is crucial. Hence, we perform a sensitivity analysis on the percentile threshold we use to identify the MD. There are the two extreme cases. For the 0th percentile the whole flow domain is considered as the MD. For the case of the 100th percentile the MD vanishes altogether. Hence, a physically relevant threshold value has to be chosen in between these two values.

In order to evaluate how much our results vary if we change the threshold for the MD calculation, we perform a sensitivity analysis. Figure B.4 a and b show the streamwise and transverse extent of the identified MD normalized by the respective flow domain size as a function of the threshold. Figure B.4 c shows the relative error between the simulated impact pressure values, which are independent of the MD definition, and the estimated impact pressure values (sections 3.2 and 3.3 of the main article), which are based on the properties of the identified domain.

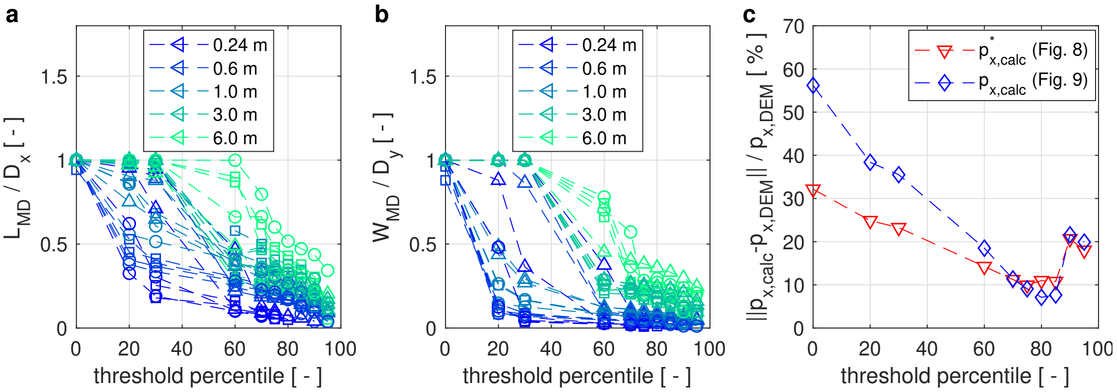

Figure B.4 – Sensitivity of the results on the MD threshold value. The MD length L_{MD} (a), the MD width W_{MD} (b) and the relative errors of the calculated pressures $p_{x,calc}$, $p^{*}_{x,calc}$ (c) are shown for different MD thresholds. The color in the left and the middle panel corresponds to the obstacle width.

Figure B.4 a and b show, that for thresholds below the 30th percentile in most simulations, the whole flow domain is considered the MD. For thresholds above 95th percentile the MD is almost vanishing in most simulations. Figure B.4 c confirms that the relative errors are highest for extremely low and extremely high threshold values. For the values higher than 95th percentile we cannot calculate the error because the MD vanishes in most simulations altogether. Both curves of relative error for the estimation of the cohesionless $p_{x,calc}$ and the cohesive pressure $p^{*}_{x,calc}$ have a robust minimum around a threshold value of 80th percentile. Hence, varying the threshold value between the 70th percentile and the 90th percentile does not influence the outcome of our results considerably. The change in the extent of the MD in these bounds of the threshold is visualized in Figure B.5, analogous to Figure 4 b in the main article.

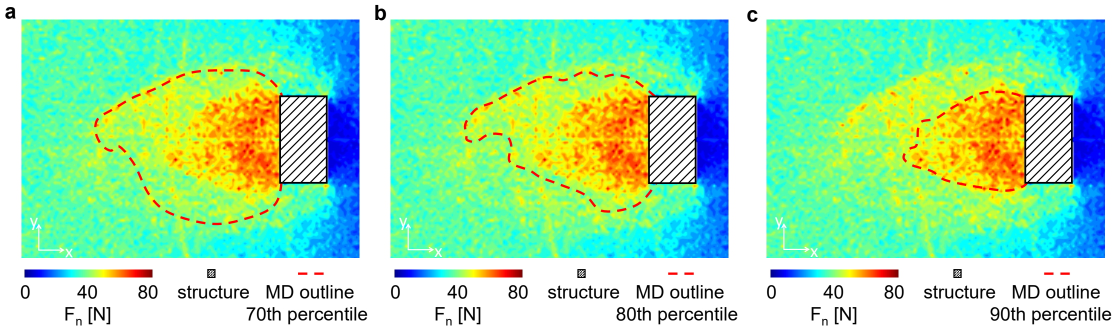

Figure B.5 – Sensitivity of the MD extent on the MD threshold value. Panels a, b and c show the MD extent for threshold values of 70th, 80th and 90th percentile, respectively.

B.5 Impact pressure calculated from reported drag forces in the literature

Existing literature on the interaction of granular materials and immersed intruders moving relative to each other often report the drag force exerted on the intruder by the granular material. In our main article we are mostly concerned with the average impact pressure on an obstacle exerted by the granular flow. We find that the average impact pressure decreases non-linearly for increasing obstacle widths. Although it seems counterintuitive at first, this trend is known to be true for granular snow avalanches Margreth, 2007. In order to find out whether this behavior is common for various configurations of granular materials interacting with intruders, we recalculate the reported drag force in the existing literature Kumar et al., 2017; Hilton and Tordesillas, 2013; Panaitescu et al., 2017 as the average impact pressure and plot them as a function of the intruder's characteristic size in Figure B.6. The results in Figure B.6 clearly confirm the trend of decreasing impact pressure for intruders of increasing width.

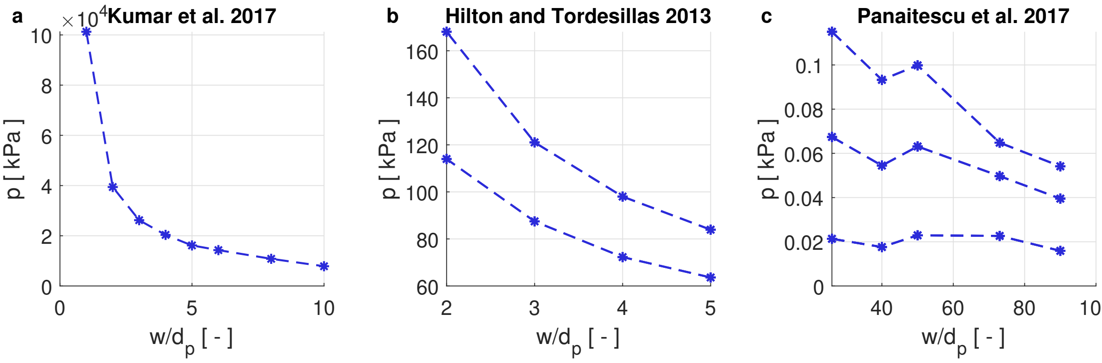

Figure B.6 – Impact pressure calculated from reported drag forces from the literature. Panels a, b and c show the data from Kumar et al., 2017, Hilton and Tordesillas, 2013 and Panaitescu et al., 2017, respectively.

B.5.1 Impact pressure scaling law for cohesive avalanches

In an earlier paper Kyburz et al., 2020, we found that the impact pressure increase due to cohesion depends on the competition of cohesive and inertial forces of the impacting granular flow. Hence, according to Eq. (B.1) the pressure exerted by a cohesionless flow with the same flow height and velocity $p_{x,calc}$ can be multiplied by a factor $f_{coh}(q_{Bo,Fr})$ to obtain the impact pressure $p^*_{x,calc}$ of an equivalent but cohesive flow. For a specific obstacle geometry the factor $f_{coh}(q_{Bo,Fr})$ is a unique function of the ratio of the Bond and the Froude number $q_{Bo,Fr} = Bo/Fr$ Kyburz et al., 2020. The dimensionless Bond number $Bo = \sigma_{coh}/p_{conf}$ is the cohesive strength σ_{coh} divided by the confining pressure p_{conf} Roy et al., 2017, which is the vertical component of the local stress tensor.

$$p^*_{x,calc} = p_{x,calc}\, f_{coh}(q_{Bo,Fr}) \tag{B.1}$$

The results from Kyburz et al., 2020 are specific for the geometry of an existing measurement structure at the “Vallée de la Sionne” avalanche test site in Valais, Switzerland. While we assume that f_{coh} varies depending on the obstacle geometry, f_{coh} could be obtained for other structure geometries by performing a number of simulations in which the granular flow velocity and cohesion are varied. Because this is a computationally intensive undertaking, we use the values found in Kyburz et al., 2020 as an approximation.

C Supplementary material for chapter 4

C.1 Simulation procedure

In this section we provide a detailed description of the simulation procedure used to obtain the simulation results presented in the main article. The procedure is identical to the one used in our earlier paper (Kyburz et al., submitted), although here we use it not only for constant velocity over the whole flow height, but also for sheared vertical velocity profiles.

The DEM simulation setup and procedure described in the following is visualized in Figure C.1. To minimize the computational effort for the simulations, we only consider an isolated volume of granular material flowing around the obstacle, instead of simulating an entire avalanche flowing down a slope. Furthermore, we split the simulation procedure into two phases. For more details on the simulation procedure, refer to (Kyburz et al., submitted; Kyburz et al., 2020) and the corresponding supporting information.

The flow of the granular material, which mimics the flowing snow avalanche, is imposed by fixing the streamwise velocity at the up- and down-stream boundaries enclosing the isolated volume in the streamwise x direction. The streamwise length of the simulation domain in the x direction is $D_x = 11$ m in simulations with obstacle widths $w \leq 1.0$ m and $D_x = 22$ m for wider obstacles to avoid the boundary influencing the flow around the obstacle. In the y direction, transverse to the flow, the granular material is confined by a periodic boundary condition. The domain width of $D_y = 28$ m is sufficient to avoid boundary influence for all obstacle widths. In the vertical z direction the domain height is $D_z = 28$ m. The particles are bound to a wall at the bottom by gravity acting in the vertical direction.

In the preparatory *phase I*, we establish the particle flow around the obstacle. At the beginning of a simulation the obstacle is placed inside the volume of granular material. To avoid large interpenetrations of the obstacle walls and particles, the particles in the volume occupied by the obstacle and it's vicinity are removed. Hence, the obstacle is initially partially immersed in the granular material, but not yet in physical contact with it. We initialize all particles starting with an initial velocity in the streamwise direction, which corresponds to the boundary velocity. We launch the simulation from the initial state until a target period Δt_1 is simulated. In this *phase I*, the boundary velocity is implemented by fixing the streamwise velocity of the particles at the up- and downstream boundaries of the granular volume. Meanwhile the particles between the boundaries can interact freely with each other and the obstacle. After Δt_1 is simulated, we generate new particles at the upstream boundary of the system and delete existing particles at the downstream boundary. We repeat *phase I* three times until the particles are flowing around the obstacle rather than impacting it directly and thus have formed a mobilized domain. However, due to the periodic generation of particles at the upstream boundary, we observe impact pressure fluctuations on the obstacle.

Because in *phase II* we start to register the impact pressure on the obstacle, which is the main result of the simulations, we want to avoid these fluctuations from *phase I* and therefore let the particles flow continuously. Hence, in *phase II* we use a larger simulation period $\Delta t_2 > \Delta t_1$ during which the granular mass is flowing continuously. To impose the desired velocity of the avalanche scenario on the freely moving particles, we use rigid walls moving at the speed of the boundary velocity. As a consequence of the long simulation period Δt_2, the upstream walls approach the obstacle as the simulation progresses. We therefore limit Δt_2 to avoid any influence of the upstream boundary on the flow field around the obstacle.

The simulated impact pressure values reported in the main article are the time average of the impact pressure during *phase II*.

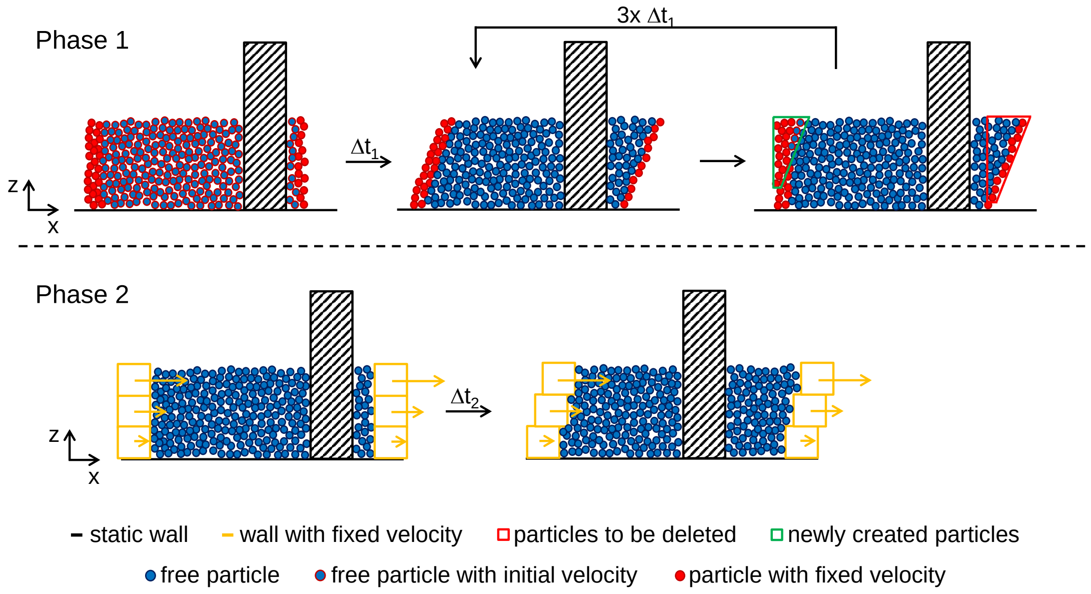

Figure C.1 – Simulation procedure in two phases for the example of a vertical shear velocity profile. *Phase I* (top) with continuous particle generation and deletion at the system boundaries. *Phase II* (bottom) with steady flow imposed by the boundary walls.

C.2 DEM parameters

In our DEM simulations individual snow flakes are not resolved as discrete elements, as this would result in prohibitive calculation times. Hence, the discrete elements correspond to aggregated snow particles with a particle radius of 32 mm $\leq r_p \leq$ 48 mm. Therefore, the physical properties of the elements also correspond to properties of snow granules.

We define the density of the spherical discrete particles as $\rho_p = 500\,\mathrm{kg/m^3}$. This results in a mean bulk density ρ_b of the undisturbed flowing material, which ranges from 361 kg/m^3 to 379 kg/m^3 in the plug flow scenarios and from 338 kg/m^3 to 340 kg/m^3 in the shear flow scenarios. For the particles' Young's modulus, we use a value of $E = 10^5$ Pa.

Aside from the particle properties, in DEM the material behavior also heavily depends on the contact law, which specifies how particles interact with each other. Here, we use the parallel-bond model, which has been used in other studies to simulate avalanches and snow on various scales (Steinkogler et al., 2015; Bobillier et al., 2020; Gaume et al., 2015b; Kyburz et al., 2020).

The contact model consists of two parallel components, whose individual force contributions are summed to obtain the contact force between two particles. The first is a linear viscoelastic component consisting of a spring and a dashpot in the normal direction, as well as a spring and a coulomb friction limit in the tangential direction. The contact stiffness of the spring is calculated via the particle's Young's modulus and the friction force using a friction coefficient of $\mu = 0.5$. The second, cohesive component is a bond connecting the particles. The bond acts mechanically like a beam and can sustain tensile, bending, shear and torsional forces. Hence, the cohesion of the granular material is controlled by the strength σ_{coh} of the cohesive bond, which we vary according to the selected avalanche scenario (see main article). For the bond's Young's modulus, we use the same value as for the particles. In our simulations, a cohesive bond is formed whenever two unbonded particles become in contact.

For more in-depth information on the particle and contact law properties, please refer to the supplementary material of our earlier paper (Kyburz et al., 2020).

C.3 Pressure calculation for real avalanche scenarios: parameter choice

In order to calculate the impact pressure profiles shown in Fig. 9 of the main article, we use the following values and assumptions:

- **C_o:** We set $C_o = 2.0$ for the wall and the wedge, who's frontal surfaces facing the avalanche are flat, as well as $C_o = 1.65$ for the pylon obstacle.

- **C_w:** We set $C_w = 1.7$ for the pylon, $C_w = 2.0$ for the wedge and $C_w = 1.6$ for the wall in the warm plug regime. Although the sensor on the pylon is smaller than the structure width, we consider the whole structure width to be representative of the pressure in the warm plug regime (Sovilla et al., 2016). In the cold dense regime we set $C_w = 1$ for all obstacles.

- **Density:** We choose densities of 375 kg/m^3 and 340 kg/m^3 in the warm plug and cold dense regime, respectively. These values correspond to the mean of the ρ_b ranges in the respective regime (see Table 1 in the main article).

- **Velocity:** For the velocity v, we consider the approach velocity far from the obstacle, where the avalanche flow is not influenced by the presence of the obstacle. In the simulation this corresponds to the imposed boundary velocity, which is slightly higher than the velocity measured directly at the pylon obstacle.

- **Cohesion:** In the warm plug flow, we take the effect of cohesion into account by using the scaling law from Kyburz et al. (2020). For the warm plug flow we obtain $f_{coh} = 1.94$ and for the cold shear flow $f_{coh} = 1.0$.

- **Vertical velocity and pressure profiles:** In the gravitational regime, we assume that the impact pressure increases linearly from 0 kPa at the free surface of the flow to $2\,p_x$ at the bottom of the flow (Wieghardt, 1975; Sovilla et al., 2010; Sovilla et al., 2016). In the inertial regime, the pressure is proportional to velocity squared. Hence, we calculate the pressure profile proportional to the imposed boundary velocity profile, which increases linearly from 0 m/s at the bottom to the maximum velocity at the free surface of the flow.

Bibliography

Albaba, A., S. Lambert, F. Nicot, and B. Chareyre (2015). “Relation between microstructure and loading applied by a granular flow to a rigid wall using DEM modeling”. In: *Granular Matter* 17(5), pp. 603–616. DOI: https://doi.org/10.1007/s10035-015-0579-8.

Albert, I., J. G. Sample, A. J. Morss, S. Rajagopalan, A.-L. Barabási, and P. Schiffer (2001). “Granular drag on a discrete object: Shape effects on jamming”. In: *Physical Review E* 64 (6), p. 061303. DOI: https://doi.org/10.1103/PhysRevE.64.061303.

Albert, I., P. Tegzes, B. Kahng, R. Albert, J. G. Sample, M. Pfeifer, A.-L. Barabási, T. Vicsek, and P. Schiffer (2000). “Jamming and Fluctuations in Granular Drag”. In: *Physical Review Letters* 84 (22), pp. 5122–5125. DOI: https://doi.org/10.1103/PhysRevLett.84.5122.

Albert, R, M. Pfeifer, A.-L. Barabasi, and P Schiffer (1999). “Slow Drag in a Granular Medium”. In: *Physical Review Letters* 82, pp. 205–208. DOI: https://doi.org/10.1103/PhysRevLett.82.205.

Allix, A. (1925). “Les avalanches”. In: *Revue de Géographie Alpine* 13, pp. 359–419.

Ammann, W. J. (1999). “A new Swiss test-site for avalanche experiments in the Vallée de la Sionne/Valais”. In: *Cold Regions Science and Technology* 30(1), pp. 3–11. DOI: https://doi.org/10.1016/S0165-232X(99)00010-5.

Ancey, C. (2016). “Snow Avalanches”. In: *Natural Hazard Science*. Ed. by S. Cutter. Oxford University Press: Oxford. DOI: https://doi.org/10.1093/acrefore/9780199389407.013.17.

Ancey, C. (2006). *Dynamique des avalanches*. Ed. by V. Bain. Presses Polytechniques et Universitaires Romandes: Lausanne. ISBN: 2-88074-648-5.

Ancey, C. (2012). “Gravity flow on steep slope”. In: *Buoyancy-Driven Flows*. Ed. by E. P. Chassignet, C. Cenedese, and J. Verron. Cambridge University Press, 372—432. DOI: https://doi.org/10.1017/CBO9780511920196.011.

Ancey, C. and V. Bain (2015). “Dynamics of glide avalanches and snow gliding”. In: *Reviews of Geophysics* 53(3). 2015RG000491, pp. 745–784. ISSN: 1944-9208. DOI: https://doi.org/10.1002/2015RG000491.

Andreotti, B., Y. Forterre, and O. Pouliquen (2013). *Granular Media: Between Fluid and Solid*. Cambridge University Press. DOI: https://doi.org/10.1017/CBO9781139541008.

Armanini, A. (1997). “On the dynamic impact of debris flows”. In: *Recent Development on Debris Flows*. Ed. by A. Armanini and M. Michiue. Vol. Lecture Notes in Earth Sciences, 64. Springer: Berlin, pp. 208–226.

Ballard, G. E. H. and R. W. McGaw (1965). *A theory of snow failure*. Tech. rep. Research Report 137.

Baroudi, D., B. Sovilla, and E. Thibert (2011). “Effects of flow regime and sensor geometry on snow avalanche impact-pressure measurements”. In: *Journal of Glaciology* 57(202), 277—288. DOI: https://doi.org/10.3189/002214311796405988.

Bartelt, P. and B. W. McArdell (2009). “Granulometric investigations of snow avalanches”. In: *Journal of Glaciology* 55(193), 829—833. DOI: https://doi.org/10.3189/002214309790152384.

Bobillier, G., B. Bergfeld, A. Capelli, J. Dual, J. Gaume, A. van Herwijnen, and J. Schweizer (2020). “Micromechanical modeling of snow failure”. In: *The Cryosphere* 14(1), pp. 39–49. DOI: https://doi.org/10.5194/tc-14-39-2020.

Bozhinskiy, N. and K. Losev (1998). *The fundamentals of Avalanche Science.* Tech. rep. 55. EISFL.

Brugnot, G. and J.-P. Vila (1985). “Investigation théorique et expérimentale des caractéristiques dynamiques des avalanches de neige dense”. In: *La Houille Blanche* 2, pp. 133–142.

Burkard, A, H. U. Gubler, and B. W. Salm (1990). *Berechnung von Fliesslawinen: eine Anleitung für Praktiker mit Beispielen.* ger. Vol. 47. Mitteilungen des Eidgenössischen Instituts für Schnee- und Lawinenforschung. Eidgenössisches Institut für Schnee- und Lawinenforschung: Davos.

Butlanska, J., M. Arroyo, and A. Gens (2009). “Homogeneity and Symmetry in DEM Models of Cone Penetration”. In: *AIP Conference Proceedings* 1145(1), pp. 425–428. DOI: https://doi.org/10.1063/1.3179952.

Calvetti, F., C. G. di Prisco, and E. Vairaktaris (2017). “DEM assessment of impact forces of dry granular masses on rigid barriers”. In: *Acta Geotechnica* 12(1), pp. 129–144. ISSN: 1861-1133. DOI: https://doi.org/10.1007/s11440-016-0434-z.

Castebrunet, H., N. Eckert, G. Giraud, Y. Durand, and S. Morin (2014). “Projected changes of snow conditions and avalanche activity in a warming climate: the French Alps over the 2020-2050 and 2070-2100 periods”. In: *The Cryosphere* 8(5), pp. 1673–1697. DOI: https://doi.org/10.5194/tc-8-1673-2014.

Ceccato, F., I. Redaelli, C. di Prisco, and P. Simonini (2018). “Impact forces of granular flows on rigid structures: Comparison between discontinuous (DEM) and continuous (MPM) numerical approaches”. In: *Computers and Geotechnics* 103, pp. 201–217. ISSN: 0266-352X. DOI: https://doi.org/10.1016/j.compgeo.2018.07.014.

Chanut, B., T. Faug, and M. Naaim (2009). “Mean Force On A Wall Overflowed By Dense Granular Avalanches: Discrete Numerical Simulations”. In: *AIP Conference Proceedings* 1145(1), pp. 609–612. DOI: https://doi.org/10.1063/1.3180000.

Chehata, D., R. Zenit, and C. R. Wassgren (2003). “Dense granular flow around an immersed cylinder”. In: *Physics of Fluids* 15(6), pp. 1622–1631. DOI: https://doi.org/10.1063/1.1571826.

Christoffersen, J., M. Mehrabadi, and S. Nemat-Nasser (1981). “A Micromechanical Description of Granular Material Behavior”. In: *Journal of Applied Mechanics* 48(2), pp. 339–344. DOI: https://doi.org/10.1115/1.3157619.

Chung, Y., C. Wu, C. Kuo, and S. Hsiau (2019). “A rapid granular chute avalanche impinging on a small fixed obstacle: DEM modeling, experimental validation and exploration of granular stress”. In: *Applied Mathematical Modelling* 74, pp. 540–568. ISSN: 0307-904X. DOI: https://doi.org/10.1016/j.apm.2019.05.003.

Coaz, J. W. F. (1881). *Die Lauinen der Schweizeralpen.* J. Dalp'sche Buch- und Kunsthandlung. DOI: https://doi.org/10.3931/e-rara-21209.

Crandall, S. H., T. J. Lardner, R. R. Archer, N. H. Cook, and N. C. Dahl (1978). *An introduction to the mechanics of solids.* second. Singapore : McGraw-Hill.

Cruz, F. da, S. Emam, M. Prochnow, J.-N. Roux, and F. m. c. Chevoir (2005). “Rheophysics of dense granular materials: Discrete simulation of plane shear flows”. In: *Physical Review E* 72 (2), p. 021309. DOI: https://doi.org/10.1103/PhysRevE.72.021309.

Cui, X. and J. M. N. T. Gray (2013). “Gravity-driven granular free-surface flow around a circular cylinder”. In: *Journal of Fluid Mechanics* 720, 314—337. DOI: https://doi.org/10.1017/jfm.2013.42.

Cundall, P. A. and O. D. L. Strack (1979). “A discrete numerical model for granular assemblies”. In: *Géotechnique* 29(1), pp. 47–65. DOI: https://doi.org/10.1680/geot.1979.29.1.47.

Faug, T., P. Lachamp, and M. Naaim (2002). “Experimental investigation on steady granular flows interacting with an obstacle down an inclined channel: study of the dead zone upstream from the obstacle. Application to interaction between dense snow avalanches and defence structures”. In: *Natural Hazards and Earth System Science* 2(3/4), pp. 187–191. DOI: https://doi.org/10.5194/nhess-2-187-2002.

Faug, T., B. Turnbull, and P. Gauer (2018). “Looking Beyond the Powder/Dense Flow Avalanche Dichotomy”. In: *Journal of Geophysical Research: Earth Surface* 123(6), pp. 1183–1186. DOI: https://doi.org/10.1002/2018JF004665.

Faug, T. (2013). “Granular force on objects and correlation length: Drag coefficient enhancement in low Froude number flow regimes”. In: *AIP Conference Proceedings* 1542(1), pp. 617–621. DOI: https://doi.org/10.1063/1.4812007.

Faug, T. (2015). “Macroscopic force experienced by extended objects in granular flows over a very broad Froude-number range”. In: *The European Physical Journal E* 38(5), p. 34. ISSN: 1292-895X. DOI: https://doi.org/10.1140/epje/i2015-15034-3.

Faug, T., R. Beguin, and B. Chanut (2009). “Mean steady granular force on a wall overflowed by free-surface gravity-driven dense flows”. In: *Physical Review E* 80 (2), p. 021305. DOI: https://doi.org/10.1103/PhysRevE.80.021305.

Favier, L., D. Daudon, F. Donzé, and J. Mazars (2009a). “Discrete element modelling to compute drag coefficients of obstacles impacted by granular flows”. In: *International Snow Science Workshop, Davos, Switzerland*, pp. 500–504.

Favier, L., D. Daudon, and F.-V. Donzé (2013). “Rigid obstacle impacted by a supercritical cohesive granular flow using a 3D discrete element model”. In: *Cold Regions Science and Technology* 85, pp. 232–241. ISSN: 0165-232X. DOI: https://doi.org/10.1016/j.coldregions.2012.09.010.

Favier, L., D. Daudon, F.-V. Donzé, and J. Mazars (2009b). “Predicting the drag coefficient of a granular flow using the discrete element method”. In: *Journal of Statistical Mechanics: Theory and Experiment* 2009(06), P06012. DOI: http://dx.doi.org/10.1088/1742-5468/2009/06/P06012.

Fischer, J.-T., R. Kaitna, K. Heil, and I. Reiweger (2018). “The Heat of the Flow: Thermal Equilibrium in Gravitational Mass Flows”. In: *Geophysical Research Letters* 45(20), pp. 11,219–11,226. DOI: https://doi.org/10.1029/2018GL079585.

Forterre, Y. and O. Pouliquen (2008). “Flows of Dense Granular Media”. In: *Annual Review of Fluid Mechanics* 40(1), pp. 1–24. DOI: https://doi.org/10.1146/annurev.fluid.40.111406.102142.

Gauer, P., D. Issler, K. Lied, K. Kristensen, and F. Sandersen (2008). “On snow avalanche flow regimes: Inferences from observations and measurements”. In: *International Snow Science Workshop*. Whistler, pp. 717–723.

Gauer, P. and T. Jóhannesson (2009). “Loads on masts and narrow obstacles”. In: *The design of avalanche protection dams: Recent practical and theoretical developments*. Ed. by T. Jóhannesson, P. Gauer, D. Issler, and K. Lied. European Commission - Directorate General for Research: Brussels, pp. 95–108.

Gauer, P. and T. Jóhannesson (2009). “The design of avalanche protection dams Recent practical and theoretical developments”. In: Climate Change and Environmental Risks. EUROPEAN COMMISSION. Chap. Loads on walls, pp. 77–94.

Gauer, P. and K. Kristensen (2016). “Four decades of observations from NGI’s full-scale avalanche test site Ryggfonn – Summary of experimental results”. In: *Cold Regions Science and Technology* 125, pp. 162–176. ISSN: 0165-232X. DOI: https://doi.org/10.1016/j.coldregions.2016.02.009.

Gaume, J., G. Chambon, N. Eckert, M. Naaim, and J. Schweizer (2015a). “Influence of weak layer heterogeneity and slab properties on slab tensile failure propensity and avalanche release area”. In: *The Cryosphere* 9(2), pp. 795–804. DOI: https://doi.org/10.5194/tc-9-795-2015.

Gaume, J, T Gast, J Teran, A van Herwijnen, and C Jiang (2018a). “Dynamic anticrack propagation in snow”. In: *Nature communications* 9(1), p. 3047. DOI: https://doi.org/10.1038/s41467-018-05181-w.

Gaume, J., T. F. Gast, J. Teran, A. van Herwijnen, and C Jiang (2018b). “Unified modeling of the release and flow of snow avalanches using the material point method”. In: *International Snow Science Workshop, Innsbruck, Austria*. Innsbruck, Austria, pp. 1–5.

Gaume, J., A. van Herwijnen, G. Chambon, K. W. Birkeland, and J. Schweizer (2015b). “Modeling of crack propagation in weak snowpack layers using the discrete element method”. In: *The Cryosphere* 9(5), pp. 1915–1932. DOI: https://doi.org/10.5194/tc-9-1915-2015.

GDR-MiDi (2004). “On dense granular flows”. In: *The European Physical Journal E* 14(4), pp. 341–365. ISSN: 1292-895X. DOI: https://doi.org/10.1140/epje/i2003-10153-0.

Geng, J. and R. P. Behringer (2005). “Slow drag in two-dimensional granular media”. In: *Physical Review E* 71 (1), p. 011302. DOI: https://doi.org/10.1103/PhysRevE.71.011302.

Gerling, B., H. Löwe, and A. van Herwijnen (2017). “Measuring the Elastic Modulus of Snow”. In: *Geophysical Research Letters* 44(21). 2017GL075110, pp. 11,088–11,096. ISSN: 1944-8007. DOI: https://doi.org/10.1002/2017GL075110.

Gubler, H (1978). “Determination of the Mean Number of Bonds per snow grain And of the Dependence of the Tensile Strength of Snow on Stereological Parameters”. In: *Journal of Glaciology* 20, pp. 329–341. DOI: https://doi.org/10.3189/S0022143000013885.

Gubler, H., M. Hiller, G. Klausegger, and U. Suter (1986). *Messungen an Fliesslawinen.* Tech. rep. 41. SLF.

Haefeli, R. (1939). "Schneemechanik mit Hinweisen auf die Erdbaumechanik". Dissertation Technischen Wissenschaften ETH Zürich, Nr. 997. ETHZ.

Haefeli, R. (1948). "Schnee, Lawinen, Firn und Gletscher". In: *Ingenieurgeologie: Ein Handbuch für Studium und Praxis.* Ed. by L. Bendel. Springer Vienna: Vienna, pp. 663–735. ISBN: 978-3-7091-5845-6. DOI: https://doi.org/10.1007/978-3-7091-5845-6_13.

Haefeli, R. (1951). *Neuere Entwicklungstendenzen und Probleme des Lawinenverbaus im Anbruchgebiet.* Tech. rep. Buchdruckerei Büchler & Co.

Hagen, G. (1852). *Bericht über die zur Bekanntmachung geeigneten Verhandlungen der Königlich Preussischen Akademie der Wissenschaften zu Berlin.* Tech. rep. Königliche Preussische Akademie der Wissenschaften, pp. 35–42.

Hauksson, S., M. Pagliardi, M. Barbolini, and T. Jóhannesson (2007). "Laboratory measurements of impact forces of supercritical granular flow against mast-like obstacles". In: *Cold Regions Science and Technology* 49(1). Selected Papers from the General Assembly of the European Geosciences Union (EGU), Vienna, Austria, 25 April 2005, pp. 54–63. ISSN: 0165-232X. DOI: https://doi.org/10.1016/j.coldregions.2007.01.007.

Hilton, J. E. and A. Tordesillas (2013). "Drag force on a spherical intruder in a granular bed at low Froude number". In: *Physical Review E* 88 (6), p. 062203. DOI: https://doi.org/10.1103/PhysRevE.88.062203.

Hopfinger, E. J. (1983). "Snow Avalanche Motion and Related Phenomena". In: *Annual Review of Fluid Mechanics* 15(1), pp. 47–76. DOI: https://doi.org/10.1146/annurev.fl.15.010183.000403.

Huang, D. and J. H. Lee (2013). "Mechanical properties of snow using indentation tests: size effects". In: *Journal of Glaciology* 59(213), 35—46. DOI: https://doi.org/10.3189/2013JoG12J064.

Hutter, K. (1996). "Avalanche dynamics". In: *Hydrology of Disasters.* Ed. by V. Singh. Kluwer Academic Publications: Dordrecht, pp. 317–392.

Issler, D. (1999). *European avalanche test sites: Overview and analysis in view of coordinated experiments.* Tech. rep. Mitteilungen Nr. 59. WSL/SLF.

Issler, D. (2003). "Experimental Information on the Dynamics of Dry-Snow Avalanches". In: *Dynamic Response of Granular and Porous Materials under Large and Catastrophic Deformations.* Ed. by K. Hutter and N. Kirchner. Springer Berlin Heidelberg: Berlin, Heidelberg, pp. 109–160. ISBN: 978-3-540-36565-5. DOI: https://doi.org/10.1007/978-3-540-36565-5_4.

Itasca Consulting Group, Inc. (2014). *Particle Flow Code in 3D, version 5.0 software documentation.* Itasca Consulting Group Inc. Minneapolis.

Jamieson, J. and C. Johnston (1990). "In-Situ Tensile Tests of Snow-Pack Layers". In: *Journal of Glaciology* 36(122), pp. 102–106. DOI: https://doi.org/10.3189/S002214300000561X.

Jóhannesson, T., P. Gauer, P Issler, and K Lied, eds. (2009). *The design of avalanche protection dams: Recent practical and theoretical developments.* European Commission - Directorate General for Research.

Jop, P., Y. Forterre, and O. Pouliquen (2006). “A constitutive law for dense granular flows”. In: *Nature* 441(7094), pp. 727–730. DOI: https://doi.org/10.1038/nature04801.

Kang, C. and D. Chan (2018). “Numerical simulation of 2D granular flow entrainment using DEM”. In: *Granular Matter* 20(1), p. 13. ISSN: 1434-7636. DOI: https://doi.org/10.1007/s10035-017-0782-x.

Kern, M. (2000). *Inverse grading in granular flow*. EPFL: Lausanne, p. 336.

Kern, M., P. Bartelt, B. Sovilla, and O. Buser (2009). “Measured shear rates in large dry and wet snow avalanches”. In: *Journal of Glaciology* 55(190), 327—338. DOI: https://doi.org/10.3189/002214309788608714.

Kern, M. A., P. A. Bartelt, and B. Sovilla (2010). “Velocity profile inversion in dense avalanche flow”. In: *Annals of Glaciology* 51(54), 27—31. DOI: https://doi.org/10.3189/172756410791386643.

Köhler, A., J.-T. Fischer, R. Scandroglio, M. Bavay, J. McElwaine, and B. Sovilla (2018a). “Cold-to-warm flow regime transition in snow avalanches”. In: *The Cryosphere* 12, pp. 3759–3774. DOI: https://doi.org/10.5194/tc-12-3759-2018.

Köhler, A., J. McElwaine, and B. Sovilla (2018b). “GEODAR Data and the Flow Regimes of Snow Avalanches”. In: *Journal of Geophysical Research: Earth Surface* 0(0). DOI: https://doi.org/10.1002/2017JF004375.

Kumar, S., K. Anki Reddy, S. Takada, and H. Hayakawa (2017). “Scaling law of the drag force in dense granular media”. In: *arXiv e-prints*, arXiv:1712.09057, arXiv:1712.09057.

Kyburz, M. L., B. Sovilla, J. Gaume, and C. Ancey (2020). “Decoupling the role of inertia, friction, and cohesion in dense granular avalanche pressure build-up on obstacles”. In: *Journal of Geophysical Research: Earth Surface* 125(2). e2019JF005192 10.1029/2019JF005192, e2019JF005192. DOI: https://doi.org/10.1029/2019JF005192.

Kyburz, M. L., B. Sovilla, J. Gaume, and C. Ancey (submitted). “The concept of mobilized domain: how it can explain and predict the forces exerted by a cohesive granular avalanche on an obstacle”. In: *Granular Matter*.

Lazar, B. and M. Williams (2008). “Climate change in western ski areas: Potential changes in the timing of wet avalanches and snow quality for the Aspen ski area in the years 2030 and 2100”. In: *Cold Regions Science and Technology* 51(2). International Snow Science Workshop (ISSW) 2006, pp. 219–228. ISSN: 0165-232X. DOI: https://doi.org/10.1016/j.coldregions.2007.03.015.

Li, X., B. Sovilla, C. Jiang, and J. Gaume (2020). “The mechanical origin of snow avalanche dynamics and flow regime transitions”. In: *The Cryosphere* 14(10), pp. 3381–3398. DOI: https://doi.org/10.5194/tc-14-3381-2020.

Luding, S. (2008). “Cohesive frictional powders: Contact models for tension.” In: *Granular Matter* 10(4), pp. 235–246. DOI: https://doi.org/10.1007/s10035-008-0099-x.

Macaulay, M. and P. Rognon (2021). “Viscosity of cohesive granular flows”. In: *Soft Matter* 17 (1), pp. 165–173. DOI: https://doi.org/10.1039/D0SM01456G.

Margreth, S. (2007). “Snow pressure on cableway masts: Analysis of damages and design approach”. In: *Cold Regions Science and Technology* 47(1). A Selection of papers presented at the International Snow Science Workshop, Jackson Hole, Wyoming, September 19-24, 2004, pp. 4–15. ISSN: 0165-232X. DOI: https://doi.org/10.1016/j.coldregions.2006.08.020.

Margreth, S., L. Stoffel, and M. Schaer (2015). *Berücksichtigung der Lawinen- und Schneedruckgefährdung bei Seilbahnen. Ein Leitfaden für die Praxis.* WSL Berichte 28. WSL-Institut für Schnee- und Lawinenforschung SLF; Eidg. Forschungsanstalt für Wald, Schnee und Landschaft WSL.

McClung, D. M. and P. A. Schaerer (1985). "Characteristics of Flowing Snow and Avalanche Impact Pressures". In: *Annals of Glaciology* 6, 9—14. DOI: https://doi.org/10.3189/1985AoG6-1-9-14.

McClung, D. and P. A. Schaerer (2006). *The avalanche handbook.* The Mountaineers Books.

McClung, D. and P. Schaerer (1993). *The Avalanche Handbook.* The Mountaineers: Seattle.

Mears, A. (1992). *Snow-avalanche hazard analysis for land-use planning and Engineering.* Tech. rep. Bulletin 49. Colorado Geological Survey.

Mellor, M. (1968). "Avalanches". In: *Cold Regions Science and Engineering. Part III: Engineering. Section A3: Snow Technology, U.S. Army Material Command.* Cold Regions Research & Engineering Laboratory, Hanover, New Hampshire.

Mellor, M. (1974). *A review of basic snow mechanics.* US Army Cold Regions Research and Engineering Laboratory.

Mellor, M. (1978). "Chapter 23 - Dynamics of Snow Avalanches". In: *Rockslides and Avalanches, 1.* Ed. by B. VOIGHT. Vol. 14. Developments in Geotechnical Engineering. Elsevier, pp. 753–792. DOI: https://doi.org/10.1016/B978-0-444-41507-3.50031-3.

Moriguchi, S., R. I. Borja, A. Yashima, and K. Sawada (2009). "Estimating the impact force generated by granular flow on a rigid obstruction". In: *Acta Geotechnica* 4(1), pp. 57–71. ISSN: 1861-1133. DOI: https://doi.org/10.1007/s11440-009-0084-5.

Mougin, P. (1922). *Les avalanches en Savoie.* Vol. IV. Ministère de l'Agriculture, Direction Générale des Eaux et Forêts, Service des Grandes Forces Hydrauliques: Paris.

Norem, H. (1990). "Estimating snow avalanche impact pressures on towers". In: *Workshop on Avalanche Dynamics.* Ed. by H. Gubler. Vol. Mitteilungen Nr. 48. Swiss Federal Institute for Snow and Avalanches: Davos, pp. 42–56.

Panaitescu, A., X. Clotet, and A. Kudrolli (2017). "Drag law for an intruder in granular sediments". In: *Physical Review E* 95 (3), p. 032901. DOI: https://doi.org/10.1103/PhysRevE.95.032901.

Paulcke, W. (1938). "Verständliche Wissenschaft". In: *Praktische Schnee-und Lawinenkunde.* Springer-Verlag Berlin Heidelberg, pp. 196–197. DOI: https://doi.org/10.1007/978-3-642-99146-2.

Perla, R. (1980). "Avalanche Release, Motion, and Impact". In: *Dynamics of Snow and Ice Masses.* Ed. by S. C. Colbeck. Academic Press, pp. 397–462. ISBN: 978-0-12-179450-7. DOI: https://doi.org/10.1016/B978-0-12-179450-7.50012-7.

Platzer, K., P. Bartelt, and M. Kern (2007). "Measurements of dense snow avalanche basal shear to normal stress ratios (S/N)". In: *Geophysical Research Letters* 34(7), p. L07501. DOI: https://doi.org/10.1029/2006GL028670.

Potyondy, D. and P. Cundall (2004). "A bonded-particle model for rock". In: *International Journal of Rock Mechanics and Mining Sciences* 41(8). Rock Mechanics Results from the

Underground Research Laboratory, Canada, pp. 1329–1364. ISSN: 1365-1609. DOI: https://doi.org/10.1016/j.ijrmms.2004.09.011.

Proske, D., J. Suda, and J. Hübl (2011). “Debris flow impact estimation for breakers”. In: *Georisk: Assessment and Management of Risk for Engineered Systems and Geohazards* 5(2), pp. 143–155. DOI: https://doi.org/10.1080/17499518.2010.516227.

Quervain, R. de (1981). *Avalanche Atlas.* Unesco, Paris.

Roch, A. (1961). *Mesure de la force des avalanches.* Sonderdruck aus Winterbericht 1960/61, Nr. 25. Schnee- und Lawinen Forschung.

Roch, A. (1980). *Neve e Valanghe.* Club Alpino Italiano: Torino.

Rognon, P. G, J.-N Roux, D Wolf, M NaaÃ¯m, and F Chevoir (2006). “Rheophysics of cohesive granular materials”. In: *Europhysics Letters (EPL)* 74(4), pp. 644–650. DOI: https://doi.org/10.1209/epl/i2005-10578-y.

Rognon, P. G., F. Chevoir, H. Bellot, F. Ousset, M. NaaÃ¯m, and P. Coussot (2008a). “Rheology of dense snow flows: Inferences from steady state chute-flow experiments”. In: *Journal of Rheology* 52(3), pp. 729–748. DOI: https://doi.org/10.1122/1.2897609.

Rognon, P. G., J.-N. Roux, M. Naaïm, and F. Chevoir (2008b). “Dense flows of cohesive granular materials”. In: *Journal of Fluid Mechanics* 596, pp. 21–47. DOI: https://doi.org/10.1017/S0022112007009329.

Roy, S., S. Luding, and T. Weinhart (2017). “A general(ized) local rheology for wet granular materials”. In: *New Journal of Physics* 19(4), p. 043014. DOI: https://doi.org/10.1088/1367-2630/aa6141.

Roy, S., A. Singh, S. Luding, and T. Weinhart (2016). “Micro–macro transition and simplified contact models for wet granular materials”. In: *Computational Particle Mechanics* 3(4), pp. 449–462. ISSN: 2196-4386. DOI: https://doi.org/10.1007/s40571-015-0061-8.

Rudolf-Miklau, F., S. Sauermoser, and A. Mears, eds. (2014). *The Technical Avalanche Protection Handbook.* Ernst & Sohn: Berlin. DOI: https://doi.org/10.1002/9783433603840.

Salm, B. (1966). “Contribution to avalanche dynamics”. In: *Scientific Aspects of Snow and Ice Avalanche* 69, 199—214.

Salm, B. (1967). “On nonuniform, steady flow of avalanching snow”. In: *Assemblée générale de Berne.* Vol. Publication No. 79. IAHS Wallingford Oxfordshire U.K.: Berne, pp. 19–29.

Salm, B and H Gubler (1985). “Measurement and Analysis of the Motion of Dense Flow Avalanches”. In: *Annals of Glaciology* 6, 26—34. DOI: https://doi.org/10.3189/1985AoG6-1-26-34.

Salm, B. (1964). “Anlage zur Untersuchung dynamischer Wirkungen von bewegtem Schnee”. In: *Zeitschrift für angewandte Mathematik und Physik ZAMP* 15(4), pp. 357–375. ISSN: 1420-9039. DOI: https://doi.org/10.1007/BF01601287.

Sauermoser, S., M. Granig, K. Kleemayr, and S. Margreth (2012). “Grundlagen und Modelle der Lawinendynamik und Lawinenwirkung”. In: *Handbuch Technischer Lawinenschutz.* Wiley-Blackwell. Chap. 4, pp. 63–101. ISBN: 9783433600856. DOI: https://doi.org/10.1002/9783433600856.ch4.

Scapozza, C. (2004). “Entwicklung eines dichte-und temperaturabhängigen Stoffgesetzes zur Beschreibung des visko-elastischen Verhaltens von Schnee”. PhdThesis. ETH Zürich. DOI: https://doi.org/10.3929/ethz-a-004680249.

Scheiwiller, T. and K. Hutter (1982). *Übersicht über Experimente und theoretische Modelle von Fliess-und Staublawinen*. Tech. rep. Mitteilung Nr. 58. VAW, ETH Zürich, p. 166.

Seguin, A., C. Coulais, F. Martinez, Y. Bertho, and P. Gondret (2016). “Local rheological measurements in the granular flow around an intruder”. In: *Physical Review E* 93 (1), p. 012904. DOI: https://doi.org/10.1103/PhysRevE.93.012904.

Shapiro, L. H., J. Johnson, M. Sturm, and G. Blaisdell (1997). “Snow Mechanics: Review of the State of Knowledge and Applications”. In: *CRREL Report 97-3*, p. 40.

Sokratov, S. (2013). “The Russian contribution to snow science”. In: *Ice* 162, pp. 4–9.

Sovilla, B., M. Kern, and M. Schaer (2010). “Slow drag in wet-snow avalanche flow”. In: *Journal of Glaciology* 56(198), pp. 587–592. DOI: https://doi.org/10.3189/002214310793146287.

Sovilla, B., T. Faug, A. Köhler, D. Baroudi, J.-T. Fischer, and E. Thibert (2016). “Gravitational wet avalanche pressure on pylon-like structures”. In: *Cold Regions Science and Technology* 126(Supplement C), pp. 66–75. ISSN: 0165-232X. DOI: https://doi.org/10.1016/j.coldregions.2016.03.002.

Sovilla, B., S. Margreth, M. Schaer, and C. Ancey (2014). “Taking Into Account Wet Avalanche Load for the Design of Pylon-like Structures”. In: *International Snow Science Workshop, Banff, Canada*, pp. 727–732.

Sovilla, B., M. Schaer, M. Kern, and P. Bartelt (2008a). “Impact pressures and flow regimes in dense snow avalanches observed at the Vallée de la Sionne test site”. In: *Journal of Geophysical Research: Earth Surface* 113(F1). ISSN: 2156–2202. DOI: https://doi.org/10.1029/2006JF000688.

Sovilla, B., M. Schaer, and L. Rammer (2008b). “Measurements and analysis of full-scale avalanche impact pressure at the Vallée de la Sionne test site”. In: *Cold Regions Science and Technology* 51(2). International Snow Science Workshop (ISSW) 2006, pp. 122–137. ISSN: 0165-232X. DOI: https://doi.org/10.1016/j.coldregions.2007.05.006.

Steinkogler, W., J. Gaume, H. Löwe, B. Sovilla, and M. Lehning (2015). “Granulation of snow: From tumbler experiments to discrete element simulations”. In: *Journal of Geophysical Research: Earth Surface* 120(6). 2014JF003294, pp. 1107–1126. ISSN: 2169-9011. DOI: https://doi.org/10.1002/2014JF003294.

Steinkogler, W., B. Sovilla, and M. Lehning (2014). “Influence of snow cover properties on avalanche dynamics”. In: *Cold Regions Science and Technology* 97(Supplement C), pp. 121–131. ISSN: 0165-232X. DOI: https://doi.org/10.1016/j.coldregions.2013.10.002.

Szabo, D. and M. Schneebeli (2007). “Subsecond sintering of ice”. In: *Applied Physics Letters* 90(15), p. 151916. DOI: http://dx.doi.org/10.1063/1.2721391.

Takada, S. and H. Hayakawa (2020). “Drag acting on an intruder in a three-dimensional granular environment”. In: *Granular Matter* 22(1), p. 6. DOI: https://doi.org/10.1007/s10035-019-0973-8.

Thibert, E., D. Baroudi, A. Limam, and P. Berthet-Rambaud (2008). “Avalanche impact pressure on an instrumented structure”. In: *Cold Regions Science and Technology* 54(3). Snow avalanche formation and dynamics, pp. 206–215. ISSN: 0165-232X. DOI: https://doi.org/10.1016/j.coldregions.2008.01.005.

Thibert, E., H. Bellot, X. Ravanat, F. Ousset, G. Pulfer, M. Naaïm, P. Hagenmuller, F. Naaïm-Bouvet, T. Faug, K. Nishimura, Y. Ito, D. Baroudi, A. Prokop, P. Schön, A. Soruco, C. Vincent, A. Limam, and R. Héno (2015). "The full-scale avalanche test-site at Lautaret Pass (French Alps)". In: *Cold Regions Science and Technology* 115, pp. 30–41. ISSN: 0165-232X. DOI: https://doi.org/10.1016/j.coldregions.2015.03.005.

Thibert, E., T. Faug, H. Bellot, and D. Baroudi (2013). "Avalanche impact pressure on a plate-like obstacle". In: *International Snow Science Workshop, Grenoble–Chamonix, France*, pp. 663–667.

Tiberghien, D, D. Laigle, M. Naaim, E. Thibert, and F Ousset (2007). "Experimental investigations of interaction between mudflow and an obstacle". In: *Debris-flow hazards mitigation: mechanics, prediction, and assessment*, pp. 281–292.

Tighe, B. P. and M. Sperl (2007). "Pressure and motion of dry sand: translation of Hagen's paper from 1852". In: *Granular Matter* 9(3/4), pp. 141–144. ISSN: 14345021. DOI: https://doi.org/10.1007/s10035-006-0027-x.

Tomas, J. (2003). "Flow properties of cohesive nanopowders". In: *China Particuology* 1(6), pp. 231–241. ISSN: 1672-2515. DOI: https://doi.org/10.1016/S1672-2515(07)60001-3.

Valero, C. V., K. W. Jones, Y. Bühler, and P. Bartelt (2015). "Release temperature, snow-cover entrainment and the thermal flow regime of snow avalanches". In: *Journal of Glaciology* 61(225), 173–184. DOI: https://doi.org/10.3189/2015JoG14J117.

Voellmy, A. (1955a). "Über die Zerstörungskraft von Lawinen". In: *Schweizerische Bauzeitung* 73, pp. 159–165.

Voellmy, A. (1955b). "Über die Zerstörungskraft von Lawinen. II. Zur Dynamik der Lawinen". In: *Schweizerische Bauzeitung* 73, pp. 212–217.

Voellmy, A. (1955c). "Über die Zerstörungskraft von Lawinen. III. Stau- und Druckwirkungen". In: *Schweizerische Bauzeitung* 73, pp. 246–249.

Voellmy, A. (1955d). "Über die Zerstörungskraft von Lawinen. IV. Zur Lawinen-Wirkung und ihrer Bekämpfung". In: *Schweizerische Bauzeitung* 73, pp. 280–285.

Voellmy, A. (1955e). "Über die Zerstörungskraft von Lawinen (On the destructive forces of avalanches)". In: *Schweizerische Bauzeitung* 73(12/15/17/19), pp. 159–162, 212–217, 246–249, 280–285. DOI: http://doi.org/10.5169/seals-61891.

Wassgren, C. R., J. A. Cordova, R. Zenit, and A. Karion (2003). "Dilute granular flow around an immersed cylinder". In: *Physics of Fluids* 15(11), pp. 3318–3330. DOI: https://doi.org/10.1063/1.1608937.

White, F. M. (1991). *Viscous Fluid Flow*. McGraw-Hill: New York.

Wieghardt, K (1975). "Experiments in granular flow". In: *Annual Review of Fluid Mechanics* 7(1), pp. 89–114. DOI: https://doi.org/10.1146/annurev.fl.07.010175.000513.

Yamanoi, K. and Y. Endo (2002). "Dependence of shear strength of snow cover on density and water content". In: *Seppyo* 64(4), pp. 443–451. DOI: https://doi.org/10.5331/seppyo.64.443.

Zimmermann, E. (1936). "Von Lawinen". In: *Schweizerische Bauzeitung* 107-108(25), pp. 541–543. DOI: http://dx.doi.org/10.5169/seals-48319.

Curriculum Vitae

Michael Lukas Kyburz

May 28, 2021

August 30, 1989
Phone: +41 79 259 99 23
Email: michi.kyburz@bluewin.ch

06.2017 – 06.2021
PhD thesis, Mechanics Doctoral School EPF Lausanne, SLF Davos
Thesis: "Pressure on obstacles induced by granular snow avalanches"

09.2013 – 12.2015
Master of Science in Mechanical Engineering ETH Zürich
Focus: Fluid dynamics
Master thesis: "Study on the influence of tip clearance on a miniature high speed compressor"
Semester thesis: "Test of a 2D CFD code for simulating radial compressors"

09.2010 – 09.2013
Bachelor of Science in Mechanical Engineering ETH Zürich
Focus: Energy, flows and processes
Bachelor thesis: "Design improvement of a low pressure plasma circulating fluidized bed reactor"

08.2005 – 06.2010
Matura Alte Kantonsschule Aarau
Special program for competitive athletes
Focus: Chemistry and biology
Minor: Arts